universität wien

MASTERARBEIT | MASTER'S THESIS

Titel | Title

FLUKA Monte Carlo code as a tool for advanced evaluations of clinical proton plans

verfasst von | submitted by

Naomi Rodriguez Acevedo BSc

angestrebter akademischer Grad | in partial fulfilment of the requirements for the degree of

Master of Science (MSc)

Wien | Vienna, 2024

Studienkennzahl lt. Studienblatt | Degree programme code as it appears on the student record sheet:	UA 066 876
Studienrichtung lt. Studienblatt | Degree programme as it appears on the student record sheet:	Masterstudium Physics
Betreut von | Supervisor:	Hon.-Prof. Dipl.-Phys. Dr. Eberhard Widmann

Acknowledgements

I want to express my gratitude to EBG MedAustron GmbH, especially to the radiation protection group, for giving me the opportunity to do a summer internship and combine it with the writing of this thesis. I would especially like to thank my supervisor Dr. Marta Mumot for her assistance, support, patience, and guidance, as well as for her work on the beam model and nozzle geometry, which are incorporated in this thesis. Additionally, I am thankful to Michael Deutsch for introducing me to FLUKA and always helping me with my questions about the software. Furthermore, I am grateful to all my friends and colleagues at MedAustron for constantly motivating and assisting me, even though many of them were not directly involved in the project.

I would also like to express my gratitude to Dipl.-Phys. Dr. Eberhard Widmann, the director of the Stefan Meyer Institute of the Austrian academy of sciences for taking over the supervision of this project. I appreciate your consistent availability to discuss the project, your constructive feedback as well as your assistance and flexibility throughout the process. Finally, I am grateful to my friends and family for their constant support, motivation, and feedback, and to the University of Vienna for allowing me to undertake this work.

Abstract

Monte Carlo simulations are powerful tools for evaluating the effects of patient irradiation that cannot be assessed using a standard treatment planning system (TPS) typically used at particle therapy centers like MedAustron. Furthermore, the flexibility of general purpose Monte Carlo codes such as FLUKA makes them suitable for research purposes in a clinical setting and for complex treatment plans.

To assess clinical treatment plans using FLUKA, the commissioning of specific input parameters was necessary. This involved the recalculation of three facility-specific mass density to Hounsfield units (HU) calibration curves and the adaptation of the beam model. The treatment plans were created using the Raystation TPS, which is used by MedAustron in their clinical practice. The computed tomography (CT) scans of different phantoms were used, one with materials of known density and another made of tissue equivalent materials, to develop these plans. The plans were designed for a monoenergetic beam with nominal energies of 97.4 MeV and 62.4 MeV respectively. The dose distribution was recalculated using the Monte Carlo FLUKA code, and the ranges at 80% of the maximum dose for each material category in the phantom were compared.

The differences in the range of the TPS and FLUKA recalculations for all three calibration curves are found within resolution limit of TPS. However, there are larger range differences for certain material categories. Therefore, a more detailed calibration of these regions may be of interest in the future. The impact of the beam model on the dose distribution was superficially evaluated, showing to have an effect mostly in the plateau region of the beam. It is also estimated that the absence of the beam model in the input configuration of FLUKA may lead to differences in dose distribution for plans where the beam interacts with multiple materials. In conclusion, the evaluation of specific treatment plans using FLUKA in a clinical setting is feasible, specially when considering all input parameters.

Kurzfassung

Monte Carlo Simulationen erlauben die Bewertung von Effekten, die bei der Plannung von Patientenbestrahlungen mit konventionellen Planungssystemen (eng. treatment planing system, TPS) nicht beurteilt werden können. Außerdem sind generische Monte Carlo Codes wie FLUKA aufgrund ihrer Flexibilität für Forschungszwecke im klinischen Umfeld und für komplexe Behandlungspläne geeignet.

Um klinische Therapiepläne mit FLUKA auswerten zu können, war die Anpassung spezifischer Eingabeparameter erforderlich. Insbesondere mussten die einrichtungsspezifischen Kalibrierkurven, die die Umrechnung der Gewebemassendichten in Hounsfield-Einheiten definieren, angepasst werden. Auch das Strahlmodell musste für diesen Zweck adaptiert werden. Zur Überprüfung des Einflusses der oben genannten Parameter auf die simulierte Dosisverteilung wurden Therapiepläne mit dem von MedAustron in der klinischen Praxis eingesetzten Planungssystem "RayStation" erstellt. Zur Erstellung dieser Pläne wurden zwei verschiedene Phantome verwendet. Eines mit Materialien bekannter Dichte und eines mit gewebeäquivalenten Materialien. Die Pläne wurden für einen monoenergetischen Strahl mit nominalen Energien von 97.4 MeV bzw. 62.4 MeV optimiert. Die berechneten Dosisverteilungen wurden exportiert, mit dem Monte Carlo Code FLUKA neuberechnet und die Reichweiten der beiden Dosiskurven bei 80% der maximalen Dosis für jede Materialkategorie im Phantom verglichen.

Die Abweichungen der Reichweiten der Dosisverteilungen von TPS und FLUKA liegen für alle drei Kalibrierkurven innerhalb der Auflösungsgrenze des TPS. Für bestimmte Materialkategorien sind die Abweichungen allerdings größer. Eine detailliertere Kalibrierung dieser Bereiche könnte daher in der Zukunft sinnvoll sein. Der Einfluss des Strahlmodells auf die Dosisverteilung wurde zunächst grob bewertet und zeigte eine Auswirkung vor allem im Plateaubereich der Bragg-Kurve. Außerdem wird ein Zusammenhang zwischen dem Fehlen des Strahlmodells in der FLUKA-Konfiguration und den Abweichungen in der Dosisverteilung vermutet. Insbesondere für Therapiepläne, bei denen der Strahl mit mehreren Materialien wechselwirkt.

Schlussendlich konnte für den Fall des Teilchentherapiezentrums MedAustron gezeigt werden, dass Therapiepläne mit FLUKA evaluierbar sind, wenn sämtliche Eingabeparameter für die Simulationen miteinbezogen werden.

Contents

List of Tables

List of Figures

1. Introduction

1.1. Motivation

The project idea originated from the necessity to evaluate certain effects of patient irradiations that could not be assessed with a standard treatment planning system (TPS) commonly utilized at particle therapy centers such as MedAustron. For instance, the activation of irradiated metallic implants and the contribution of secondary neutrons deposited outside the target volume [1], are some effects that are not currently accounted for in TPS. This is because commercial treatment planning systems rely on approximations to reduce computation time, which is crucial for routine clinical use. The dose deposited by neutrons or from the activation in standard treatment procedures is small and therefore clinically insignificant. However, it is still important to consider these effects in special cases or whenever possible in order to optimize the treatment according to the ALARA (As Low As Reasonably Achievable) rule and for radiation protection.

Monte Carlo simulations consider the physics of particle interactions at the microscopic level. This is achieved by calculating the interaction of each particle using either theoretical models or experimental cross-section data for electromagnetic and nuclear interactions [2, 3, 4]. Furthermore, they consider tissue inhomogeneities by using specific material properties, such as elemental composition, electron density, mass density, or ionization potential, and model the appropriate position of inhomogeneities along the beam path as well as their scattering effects [2]. Since Monte Carlo dose calculations are considered to be the most accurate method for dose calculation in radiotherapy, several fast Monte Carlo-based dose calculation algorithms have been developed and implemented in many commercial TPSs [5, 2]. However, these types of Monte Carlo-based TPSs are inflexible and have numerous limitations that make them unsuitable for research purposes or for certain patient assessment cases [6].

The latest version of the general-purpose Monte Carlo code, FLUKA, along with the FLAIR interface, offers useful tools for importing and using DICOM (Digital Imaging and Communications in Medicine) data. This makes FLUKA a flexible tool for the evaluation and comparison of dose distributions for complex treatment plans [6, 3, 4]. The focus of this work is on the preparation and configuration of the necessary tools for the comparison and analysis of the planned and calculated dose distributions between the two systems.

1.2. MedAustron

MedAustron is a synchrotron-based particle therapy and research facility located in Wiener Neustad, Lower Austria, approximately 50 kilometers south of the city of Vienna.

It is one of only six such centers in the world, providing protons and light-ions for a range of cancer treatment, clinical research and non-clinical research applications [7, 8]. The origins of MedAustron can be traced back to the AUSTRON project, which was launched in the early 1990s to establish a scientific research center in Central Europe. Initially, the project aimed to create a neutron spallation source, however, after a feasibility study in 1994, the focus shifted to the development of an ion therapy center. The Proton-Ion Medical Machine Study (PIMMS) group was founded with the purpose of developing a specialized synchrotron for medical treatments [9]. In 2007, the ownership of the project was transferred to the region of Lower Austria, which then initiated the establishment process. Construction began in 2012, and after four years, the first patient was successfully treated with protons in December 2016, marking a significant milestone for the project. Since then, the facility has continued to evolve, most notably with the implementation of the gantry, the introduction of carbon ion-based treatments, and the addition of a helium source in the near future. The layout of the facility is illustrated in Figure 1.1.

Figure 1.1.: Overview of the MedAustron facility, used with permission from MedAustron [10].

The accelerator is currently equipped with three ion sources, which generate the particle beams. One of these is a carbon dioxide (CO_2) source, which produces carbon ions. The remaining two are hydrogen gas (H_2) sources, which generate proton beams [11]. The process begins with the heating of carbon dioxide and hydrogen gas to elevated temperatures, generating a plasma. Utilising an electric field, the positive and negative charges within this plasma are then separated. The ions are subsequently transported from the sources to the linear accelerator via a Low Energy Beam Transfer (LEBT) line, where they reach an energy of 8 keV per nucleon. In the linear accelerator (LINAC) the

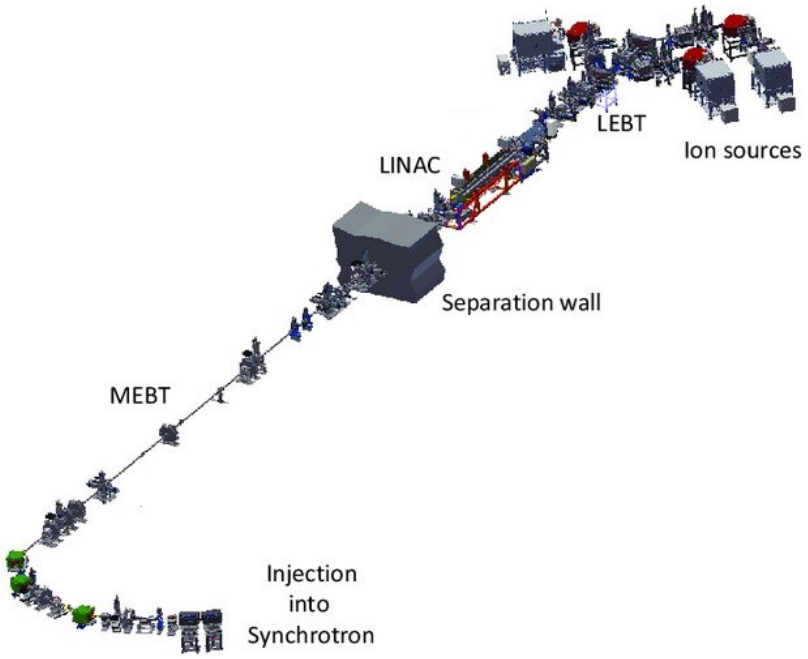

Figure 1.2.: Part of the MedAustron accelerator system, including key parts such as the low energy beam transfer and the medium energy beam transfer, used with permission from MedAustron [10, 13].

particles are accelerated to 7 MeV per nucleon [7]. Upon transfer to the synchrotron via the Medium-Energy Beam Transfer (MEBT) line, the beam is focused onto a carbon stripper foil to remove any residual electrons from the ions, providing a mass-to-charge ratio of $m/q = 1$ for the protons and $m/q = 1/2$ for the carbon ions. Finally, two dipole magnets facilitate the injection of the beam into the synchrotron at the end of the MEBT line. The particles injected into the synchrotron are bunched and accelerated by the RF-system to the desired extraction energy before being transported to different irradiation rooms (IR1-IR4) by a beam delivery system [12]. IR1 is dedicated to research, while IR2-IR4 are used for treatment. Three of the treatment rooms are equipped with fixed beam lines, and the fourth room is equipped with a proton gantry system, which allows for flexible patient treatment. Proton energies for clinical use range from 62.4 MeV to 252.7 MeV per nucleon, and can go up to 800 MeV for non-clinical research purposes [7].

1.3. Particle Therapy

Particle therapy uses ion beams (protons or heavier ions) to treat patients with malignant or non-malignant tumors [14]. It provides an alternative to conventional photon radiation therapy and has several biological advantages due to its physical properties, which result in

precise dose deposition within a defined range, minimizing damage to surrounding healthy tissue. The higher precision also permits the treatment of tumors near radiation-sensitive organs.

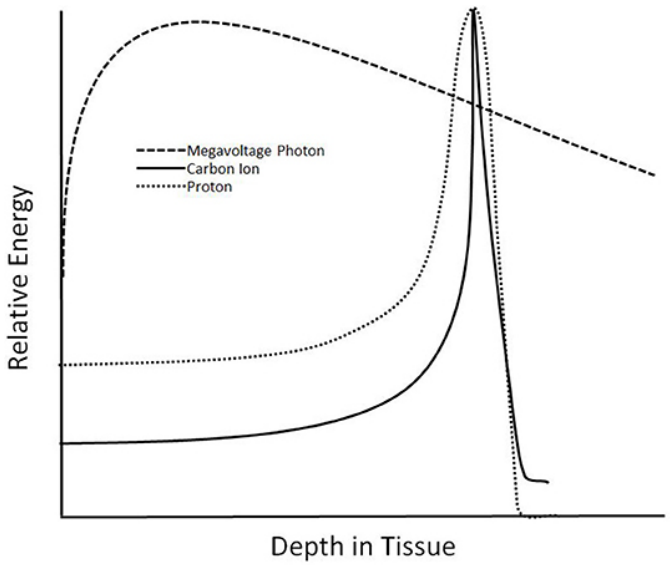

Figure 1.3.: Dose deposition at depth for 6 MV photons, protons, and carbon ions by Timothy D. Malouff et al. [15], used under CC BY 4.0

In Figure 1.3, the dose distribution of proton and carbon ion is compared to that of megavoltage photon. It is observed that photons release most of their energy at the beginning of their trajectory, while protons and carbon ions deposit most of their energy towards the end of their path through matter, with minimal energy being delivered within the so-called plateau region. The Bragg peak refers to the region where maximal energy deposition occurs at the end of an ion's path [16]. The underlying physical principles responsible for the characteristic dose deposition of protons and other light ions are explained in more detail in Chapter 2.4.5.

2. Radiation Physics

This chapter introduces the basic interactions between radiation and matter. Concepts such as cross-section and mean free path are introduced in 2.1. These concepts are essential for understanding the probability of certain interactions between particles and matter and their energy dependence. Next, in chapter 2.2, the various mechanisms of photon interaction, such as the photoelectric effect, elastic scattering, the Compton effect, and pair production are explored. These interactions serve as the foundation for several medical imaging systems and play an important role in proton therapy. Finally, 2.4 focuses on protons, discussing their interactions and energy loss processes.

2.1. Interaction of Radiation with Matter

The interaction of radiation with matter is a stochastic process [17]. The collision probability between a particle and an atom or nucleus with atomic number Z and mass number A is generally given by the microscopic cross-section σ:

$$\sigma = \sigma(Z, A, E) \tag{2.1}$$

The microscopic cross-section depends on the projectile type and energy E and is often seen as the effective area of the collision [18]. The microscopic cross-section is usually given in units of barns $1\,\text{barn} = 1 \times 10^{-24}\,\text{cm}^2$ [17]. A related concept is the macroscopic cross-section Σ, which is indirectly proportional to the average distance between two successive collisions, i.e., the mean free path λ. The relation between the macroscopic cross-section and the mean free path is given by:

$$\Sigma = \frac{1}{\lambda} \tag{2.2}$$

The mean free path λ is related to the microscopic cross-section as following:

$$\lambda = \frac{1}{N\sigma} = \frac{M}{\rho N_A \sigma} \tag{2.3}$$

where N is the atom density, M is the molar mass, ρ is the material density, and $N_A = 6.022\,045 \times 10^{23}\,\text{mol}^{-1}$ is the Avogadro constant [18]. The probability of a specific type of particle interaction depends on the energy. For an inhomogeneous medium or material mixtures, the mean free path becomes:

$$\lambda = \frac{1}{\Sigma_i N_i \sigma_i} = \frac{1}{\rho N_A \sum_i \left(\frac{\omega_i}{M_i}\right) \sigma_i} \tag{2.4}$$

N_i is the atom density of element i, M_i is the molar mass of element i, and ω_i is the relative weight fraction of element i in the mixture [18].

2.2. Interactions of Photons with Matter

There are four fundamental photon interactions, each associated with a specific cross-section. The cross-section for a photon to interact with an atom by the photoelectric effect is represented by $\sigma_{\text{p.e.}}$, the cross-section for interaction by coherent scattering is represented by σ_{Rayleigh}, the cross-section for incoherent scattering is represented by σ_{Compton}, and the cross-section for pair production is represented by κ_{nuc} [17]. The total cross-section gives the overall probability of photon interaction and is given by the sum of the individual cross-sections:

$$\sigma_{\text{tot}} = \sigma_{\text{p.e.}} + \sigma_{\text{Rayleigh}} + \sigma_{\text{Compton}} + \kappa_{\text{nuc}}. \tag{2.5}$$

Figure 2.1 illustrates the total cross-section as a function of photon energy in carbon, showing the contributions of the different processes [19].

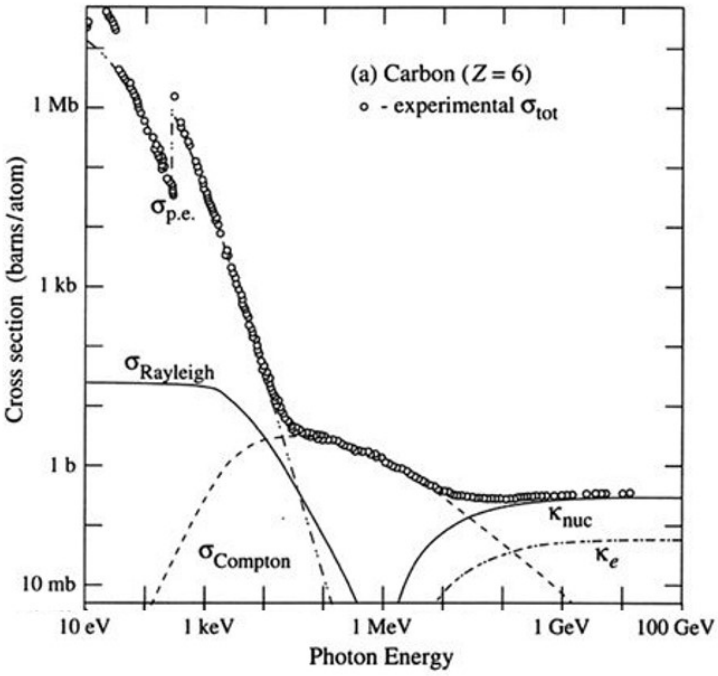

Figure 2.1.: Photon total cross-section as a function of the photon energy in carbon, with the contributions of different processes. $\sigma_{\text{p.e.}}$ corresponds to the atomic photoelectric effect and $\kappa_{\text{nuc}}(\kappa_e)$ corresponds to pair production in the nuclear (electron) field by Christian Fabjan et al. [15], used under CC BY 4.0[20].

In the diagnostic energy range up to 150 keV, only the photoelectric effect, coherent scattering, and incoherent scattering are significant. Pair production become important at much higher energies [17]; nevertheless, all photon interaction processes will be described in detail in the following sections.

2.2.1. Photoelectric Effect

When an incoming photon interacts with an atom, it causes the atom to enter an excited state, ejecting an electron from an atomic shell. This electron is called a photoelectron and carries kinetic energy equal to the difference between the binding energy of the electron to the atom and the energy of the incident photon:

$$E_{\text{kin}} = h\nu - E_{\text{binding}} \tag{2.6}$$

E_{kin} is the kinetic energy of the ejected electron, h is the Planck constant, ν is the photon frequency, and E_{binding} is the binding energy between the electron and the atom [17]. If the photoelectric effect involves an inner-shell electron, the electron ejection is followed by atomic relaxation, i.e. the missing inner-shell electron is replaced by an outer-shell electron, which emits characteristic X-rays or Auger electrons to compensate for the energy difference. As shown in Figure 2.1, the photoelectric effect is the dominant photon process at energies up to the keV region [18]. For diagnostic energies up to 150 keV, the photoelectric effect cross-section $\sigma_{\text{p.e.}}$ is proportional to:

$$\sigma_{\text{p.e.}} \propto \frac{Z^n}{(h\nu)^m} \tag{2.7}$$

where Z is the atomic number of the target material, h is the Planck constant, ν is the photon frequency, n and m are exponents in the range of 3.6-5.3 and 2.5-3.5 respectively, being largest for low atomic numbers [17]. Depending on the energy of the photon, the cross-section scales with the Z^4 or Z^5 [18].

2.2.2. Coherent Scattering

Coherent scattering, also referred to as Rayleigh scattering, is a cooperative phenomenon involving the interaction of all the electrons in the atom [21]. It represents a form of elastic scattering, in which the internal energy of the particles involved in the collision is preserved, with changes occurring only in their relative velocities [19]. This mechanism is relevant at high atomic numbers and energies in the keV range. Therefore, it is not significant for tissue or tissue-equivalent materials [21].

2.2.3. Compton Effect

Incoherent scattering, better known as Compton scattering or the Compton effect, describes a case of scattering in which a photon collides with an electron, resulting in a change in the energy and momentum of the photon [18].

The relationship between the deflection of a photon and the loss of energy in Compton scattering is established by the principles of conservation of momentum and energy between the incident photon and the recoiling electron [17], as described in equation (2.8).

$$\Delta\lambda = \lambda' - \lambda = \frac{h}{m_e c}\left(1 - \cos(\theta)\right) \tag{2.8}$$

where λ and λ' are the wavelengths of the photon before and after the collision, m_e is the mass of the electron, h is the Plank constant, c is the speed of light and θ is the scattering angle. The Compton effect is the dominant process at MeV energies, as depicted in Figure 2.1. In the diagnostic energy range, the energy transfer to the recoil electron is also small. For photons with energies ranging from 50 keV to 100 keV, the maximum energy transfer to the recoil electron is between 8.2 keV and 28.1 keV. This occurs when the photon is backscattered [17]. The Compton effect assumes that the electron is free and at rest. The incoherent scattering cross-sections σ_{Compton} of bound atomic electrons can be approximated by multiplying the Compton effect cross-sections by the number of electrons in the atom [17]. σ_{Compton} scales with the atomic number Z, resulting in a weaker dependence on atomic number than the photoelectric effect and electron-positron production [18].

2.2.4. Pair Production

At high energies, pair production is the dominant effect. The energy at which pair production becomes dominant decreases as the atomic number Z increases, with a threshold energy maintained at 1.022 MeV [18]. In this process, the photon is converted into an electron-positron pair, each with a kinetic energy in accordance to Equation (2.9).

$$h\nu = E_- + E_+ + 2m_0c^2 \tag{2.9}$$

the kinetic energy of the photon is given by $h\nu$, E_+ and E_- are the kinetic energies of the produced electron-positron pair, and $2m_0c^2 = 1.022\,\text{MeV}$ is the combined rest energy of the electron and positron [17]. The pair production cross-section scales approximately with Z^2 [18].

2.3. Interaction of Neutrons with Matter

Neutrons are electrically neutral particles, which are not subject to Coulomb forces. Nevertheless, they can interact with other particles through various processes. Neutrons are stable only within the nucleus of an atom; outside the nucleus, they decay with a mean lifetime of approximately 15 minutes. Similar to protons, neutrons have an atomic mass close to 1 atomic mass unit (amu). Neutrons can be produced by several processes, including alpha particle-induced nuclear reactions, spontaneous fission, neutron-induced fission, photoneutron production, accelerator sources, and nuclear fusion [22].

Neutrons are classified into several categories based on their kinetic energy:

- **Ultracold neutrons**: $E_{\text{kin}} < 2 \times 10^{-7}\,\text{eV}$
- **Very cold neutrons**: $2 \times 10^{-7}\,\text{eV} \leq E_{\text{kin}} \leq 5 \times 10^{-5}\,\text{eV}$
- **Cold neutrons**: $5 \times 10^{-5}\,\text{eV} \leq E_{\text{kin}} \leq 0.025\,\text{eV}$
- **Thermal neutrons**: $E_{\text{kin}} \approx 0.025\,\text{eV}$

- **Epithermal neutrons**: $1\,\mathrm{eV} < E_{\mathrm{kin}} < 1\,\mathrm{keV}$
- **Intermediate neutrons**: $1\,\mathrm{keV} < E_{\mathrm{kin}} < 0.1\,\mathrm{MeV}$
- **Fast neutrons**: $E_{\mathrm{kin}} > 0.1\,\mathrm{MeV}$

There are five main processes by which neutrons interact with the nuclei of a medium: elastic scattering, inelastic scattering, neutron capture, spallation, and fission [23]. The probability of a specific type of interaction between a neutron and a nucleus is energy-dependent and is expressed by the cross-section [24, 23]. The total cross-section σ_{total} is defined as the sum of all individual cross-sections and represents the probability of any interaction occurring, as given by Equation (2.10):

$$\sigma_{\mathrm{total}} = \sum \sigma_i \tag{2.10}$$

The subsequent sections provide a more detailed account of the various types of neutron interactions.

2.3.1. Elastic Scattering

In elastic scattering, the total kinetic energy of the neutron n and the nucleus remains constant throughout the interaction. During this process, the neutron transfers a portion of its kinetic energy to the nucleus. The average energy loss for a neutron with kinetic energy E_{kin} colliding with a nucleus of atomic mass A can be calculated [24] using the following Equation:

$$\Delta E = \frac{2E_0 A}{(A+1)^2}. \tag{2.11}$$

2.3.2. Inelastic Scattering

In inelastic scattering, the neutron n is captured by the nucleus and subsequently re-emitted with a loss of energy and a change in direction. Consequently, the nucleus is left in an excited state, from which it eventually releases radiation [23]. This process is described by Equation:

$$n + {}^{A}_{Z}\mathrm{X} \rightarrow {}^{A+1}_{Z}\mathrm{Y}^{*} \rightarrow {}^{A}_{Z}\mathrm{X}^{*} + n \Rightarrow {}^{A}_{Z}\mathrm{X}^{*} \rightarrow {}^{A}_{Z}\mathrm{X} + \gamma \tag{2.12}$$

where ${}^{A}_{Z}\mathrm{X}$ represents the target nucleus, ${}^{A+1}_{Z}\mathrm{Y}^{*}$ denotes the unstable nucleus resulting from the absorption of the neutron, and ${}^{A}_{Z}\mathrm{X}^{*}$ represents the excited target nucleus [23].

2.3.3. Neutron Capture

Neutron capture is a nuclear reaction in which a nucleus absorbs a neutron, leading to the emission of various particles, such as protons or gamma rays [24]. This process is represented by the Equation:

$$n + {}^{A}_{Z}\mathrm{X} \rightarrow {}^{A}_{Z+1}\mathrm{X} + x \tag{2.13}$$

In this equation, ${}^{A}_{Z}\mathrm{X}$ represents the nucleus of an atom, where A is the mass number and Z is the atomic number. Neutrons are denoted by n, and x represents the various particles emitted during the reaction, such as protons or gamma rays. In biological tissues, two neutron capture reactions are particularly significant: ${}^{14}\mathrm{N}(n,p){}^{14}\mathrm{C}$ and ${}^{1}\mathrm{H}(n,\gamma){}^{2}\mathrm{H}$ [23].

2.3.4. Spallation

Spallation is a nuclear process where a fast neutron n interacts with a nucleus and transfers sufficient energy to cause the nucleus to break down into numerous residual components, such as alpha particles α and heavier nuclei. This process occurs at high neutron energies, where the neutron-nucleus interaction results in the ejection of several nucleons and the formation of lighter nuclei [23].

2.4. Interaction of Protons with Matter

This section discusses the ways in which protons interact with matter, resulting in energy loss. Interactions occur with either atomic electrons or the nucleus. Types of interactions include inelastic interactions with atomic electrons, elastic interactions with atomic nucleons, nuclear interactions with the nucleus, and Bremsstrahlung. However, this work will not discuss the last type of interaction as it is negligible for therapeutic energies.

2.4.1. Stopping Power

Protons travelling through a medium interact with atomic electrons via electromagnetic forces. This interaction leads to the excitation and ionization of atoms in the medium, and subsequently causes the proton to lose some energy with each interaction until it comes to rest [3]. The energy loss rate of protons is given by the mass stopping power (2.14), which describes the relationship between the average energy E dissipated by ionising radiation as it travels a distance x through a medium.

$$\frac{S}{\rho} = -\frac{\mathrm{d}E}{\rho\,\mathrm{d}x} \tag{2.14}$$

where ρ is the mass density of the target material [16, 3]. The mass stopping power is defined for a beam rather than for individual particles. For protons and heavier hadrons with energies in the radiotherapy range, which is about 70 MeV up to around 250 MeV for protons, this process accounts for most of their energy loss.

The energy losses of charged particles due to inelastic collisions with atomic electrons can be described by several theories with different levels of complexity and accuracy [16]. The most accurate is the Bethe-Bloch formula, given by Equation (2.15). It was first described by Hans Bethe [25] and later developed to include relativistic, shell and density corrections [3].

$$-\frac{\mathrm{d}E}{\mathrm{d}x} = 4\pi N_{\mathrm{A}} r_e^2 m_e c^2 \frac{Z z^2}{A\beta^2}\left[\ln\left(\frac{2m_e c^2\beta^2\gamma^2}{I}\right) - \beta^2 - \frac{\delta}{2} - \frac{C}{Z}\right] \tag{2.15}$$

where $N_A = 6.022 \times 10^{23}\,\mathrm{mol}^{-1}$ is the Avogadro constant, $r_e = 2.818 \times 10^{-15}\,\mathrm{m}$ is the classical electron radius, z is the charge of the particle, Z is the atomic number, A is the atomic mass of the material, $\beta = \frac{v}{c}$ is the velocity of the particle relative to the speed of light, γ is the Lorentz factor, m_e is the rest mass of the electron, c is the speed of light in vacuum and I is the mean excitation energy of the material. C is the shell correction, which is only important if the velocity of the particle is comparable to the velocity of the atomic electrons [16]. According to Equation (2.15), the energy loss is directly proportional to the inverse square of the velocity of the projectile and the square of its charge. The energy loss does not depend on the mass of the projectile. On the other hand, it is directly proportional to the electron density in the absorber ($\frac{N_A \rho Z}{A}$). This is due to the fundamental Coulomb interactions between the projectile particles and the atomic electrons, which are the main contributors to energy dissipation. The linear stopping power also depends on the mass density of the absorbed material. In addition, the stopping power depends on the ionization potential I of the absorber, which is directly correlated to its atomic number Z. Consequently, the energy loss of protons in the human body is mainly determined by the velocity of the ion as well as by the material density, which can vary by about three orders of magnitude, ranging from air-filled cavities to dense skeletal structures [16].

2.4.2. Multiple Coulomb Scattering

Due to the repulsive force between positive charges, protons undergo elastic scattering when they approach an atomic nucleus. The large mass of the protons leads to small-angle scattering, but even a small change in the trajectory of the proton can be significant, although the proton loses a negligible amount of energy in this type of scattering [16]. In proton therapy, the thickness of the irradiated volume leads in multiple scattering events, which is known as Multiple Coulomb Scattering (MCS). MCS accounts for the combined effect of all scattering events and is an important factor to be considered when calculating dose distributions in patients or phantoms with treatment planning systems for clinical proton therapy [26, 27, 28, 16], where the sum of all collisions produces a later spread of the beam and an angular divergence [3].

Moliere's theory [29] describes the angular deflection of particles after they have travelled a certain distance. Due to the complexity of the full theory, several simplifications have been proposed in the literature. One method, proposed by Gottschalk [30], considers the simplest case, which consists of a target of a single element so thin that the proton loses negligible energy. Another approximation takes the form of the MCS as a Gaussian distribution, as described by the Equation (2.16):

$$P(\theta) \approx \frac{2\theta}{\langle\theta^2\rangle} \exp\left(\frac{-\theta\zeta^2}{\langle\theta^2\rangle}\right) \mathrm{d}\theta \tag{2.16}$$

where $\left(\langle\theta^2\rangle\right)$ is the mean square scattering angle or the width parameter of the Gaussian distribution [16]. For small angles, the angular distribution of the beam can be approximated by a Gaussian distribution [3] as defined by [31] in Equation (2.17):

$$P(\theta) = 14.1\,\mathrm{MeV}\frac{Z}{\beta pc}\sqrt{\frac{x}{L_{\mathrm{rad}}}}\left(1+\frac{1}{9}\log_{10}\frac{x}{L_{\mathrm{rad}}}\right) \tag{2.17}$$

where p is the momentum of the projectile, Z is the charge of the projectile and $\beta = \frac{v}{c}$ is the ratio of velocity to the speed of light, x is the depth of penetration in the medium being traversed and L_{rad} is the length of the radiation [3]. Equation (2.17) shows that the MCS increases significantly as the energy of the particle decreases. Additionally, targets made of heavier elements result in larger deflection angles compared to those made of lighter elements [3, 32].

2.4.3. Nuclear Interactions

Non-elastic nuclear reactions occur when a proton interacts with an atomic nucleus, inducing irreversible changes such as neutron ejection [16]. While the probability of such reactions is smaller than the other proton interactions, their significance increases with the energy and mass of the primary particle, as well as the density of the medium [3]. To penetrate an atomic nucleus, a proton must possess sufficient kinetic energy to overcome the Coulomb barrier of the target nucleus. The minimum energy threshold for non-elastic cross-section in proton-induced nuclear reactions is approximately 8 MeV in biologically relevant elements [16].

Nuclear interactions lead to the attenuation of primary particle fluence, the production of fragments, and the emergence of secondary particles. These interactions not only modify the width and height of the Bragg curve but also generate its tail [3]. Secondary particles resulting from nuclear reactions are particularly significant in proton therapy. They contribute to the total absorbed dose, potentially increases the beam's Relative Biological Effectiveness (RBE), and can produce secondary neutrons, leading to dose deposition outside the target volume [33]. In context of clinical proton therapy, relevant nuclear reactions generate energetic protons, neutrons, deuterons, tritons, ^{3}He, ^{4}He, and other small ions. While secondary protons contribute to approximately 10% of the absorbed dose in a high energy proton beam, deuterons and heavier ions contribute only 1% [16, 34]. Secondary particles generated from target fragments typically possess low energy and range, leading to the deposition of their energy in close proximity to their point of origin [3, 16]. Secondary neutrons produced by nuclear reactions in high energy proton beams are a major concern. Due to their considerable biological effectiveness, even small contributions to the absorbed dose can lead to significant side effects [35].

2.4.4. Proton Range

As discussed in previous sections, charged particles such as protons lose energy through ionization and excitation of atomic electrons as they pass through matter. In addition, protons can experience subtle changes in their trajectories due to elastic collisions with atomic nuclei. Despite this, most protons travel in an almost straight line because their mass is 1832 times greater than the mass of an electron [16]. The range of a proton is defined as the depth within a material that the proton can penetrate before coming to

rest. However, due to scattering, not all protons of the same energy have the same range. Therefore, the range must be defined for a beam rather than for a single particle [36]. In the context of proton therapy, the range of the proton beam is typically defined as the depth at which the central axis depth dose has decreased to 80% of the maximum dose [37, 36]. However, this value may vary between different sources in the literature. The range of a proton beam in a water phantom with four different nominal energies is shown in Figure 2.2

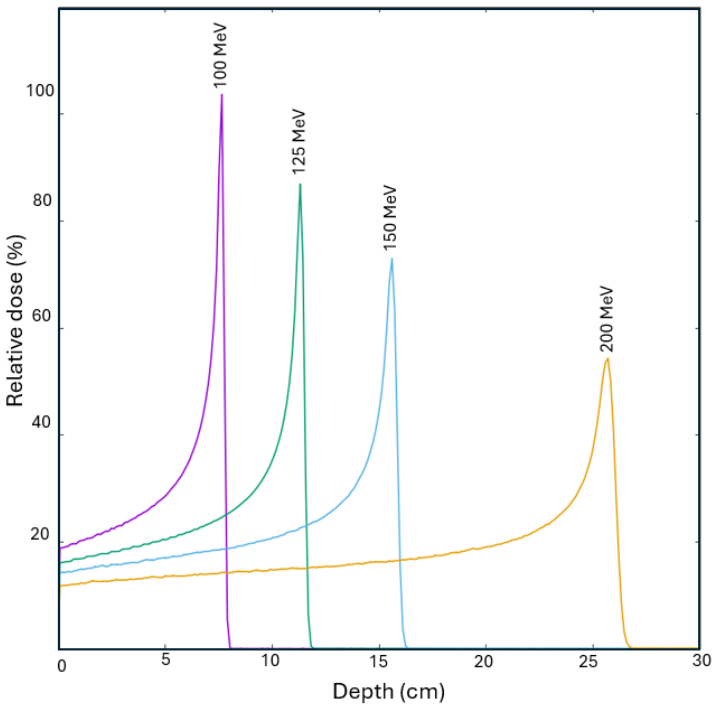

Figure 2.2.: Bragg peak for four proton beams with energies between 100-200 MeV

Assuming continuous energy loss and neglecting lateral dispersion, the range of a proton beam can be calculated using the Continuous Slowing Down Approximation (CSDA) defined by Equation (2.18).

$$R(E) = \int_0^R \left(\frac{\mathrm{d}E}{\mathrm{d}x}\right)^{-1} \mathrm{d}E \tag{2.18}$$

which integrates the inverse stopping power from 0 to the maximum energy [23, 3, 16]. The range of a proton beam depends on the kinetic energy and the mass of the particles as well as on the composition of the absorbing material [23, 16].

2.4.5. The Bragg Peak

The energy transferred from the protons to the atomic electrons in a material is described by the Bethe-Bloch formula, as discussed in Chapter 2.4.1. The energy loss per unit distance travelled through the medium is graphically represented by the central axis depth dose distribution, also known as the Bragg curve [38, 3]. The Bragg curve features different regions resulting from the specific types of interactions described in the chapters 2.4.1, 2.4.2 and 2.4.3. These regions are presented in Figure 2.3.

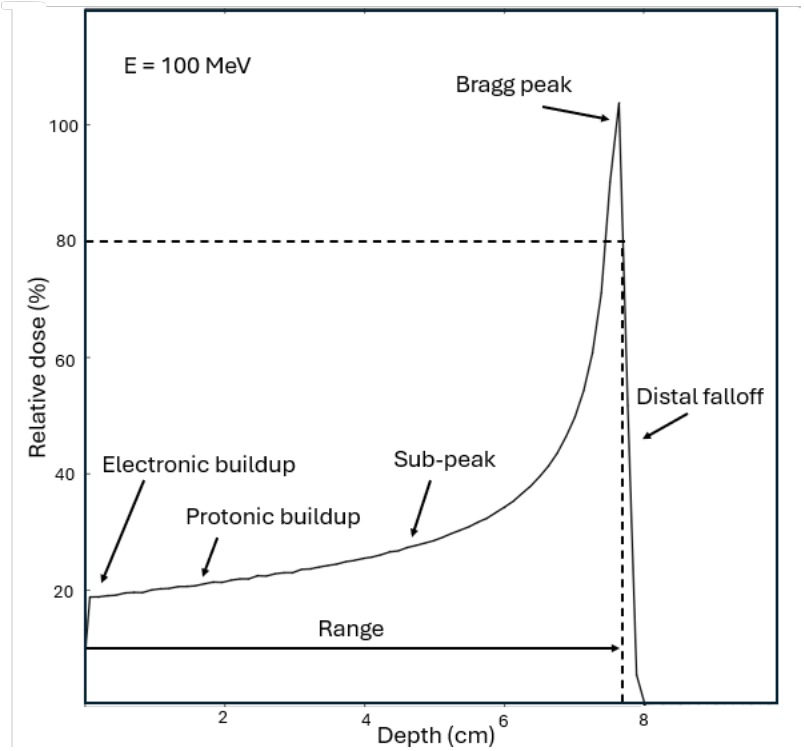

Figure 2.3.: Relative dose of a 100 MeV proton beam as a function of depth in water. The various regions and characteristics are labeled.

- The region of electronic buildup corresponds to the incident area of the proton beam, resulting from the accumulation of secondary electrons [16].
- The protonic buildup region is where the Coulomb interactions increase with depth due to the accumulation of secondary protons from proton-induced non-elastic nuclear interactions [16].
- The sub-peak region extends from the surface of the absorber to a depth just before the peak. This region is caused by the stopping power's dependence on the inverse of the proton velocity, the removal of some protons, and the release of secondary particles due to nuclear interactions [16].

- The Bragg peak is the region of maximum energy loss. The underlying physical processes include proton stopping power, dispersion of energy deposition by individual particles, and nuclear reactions [16]. Nuclear reactions do not affect the position of the Bragg peak, but they do alter some of its characteristics, such as the height and width of the peak, and are responsible for the tail [3].

When discussing proton beam therapy, it is important to distinguish between two related concepts: the Pristine and Spread Out Bragg Peak (SOBP). These concepts are illustrated in Figure 2.4. The term pristine Bragg peak refers to the unmodified depth dose distribution that arises from a monoenergetic or nearly monoenergetic proton beam. In simple terms, it describes the original and unaltered energy deposition pattern of a single proton beam, displaying a well-defined and distinct peak in energy release [16].

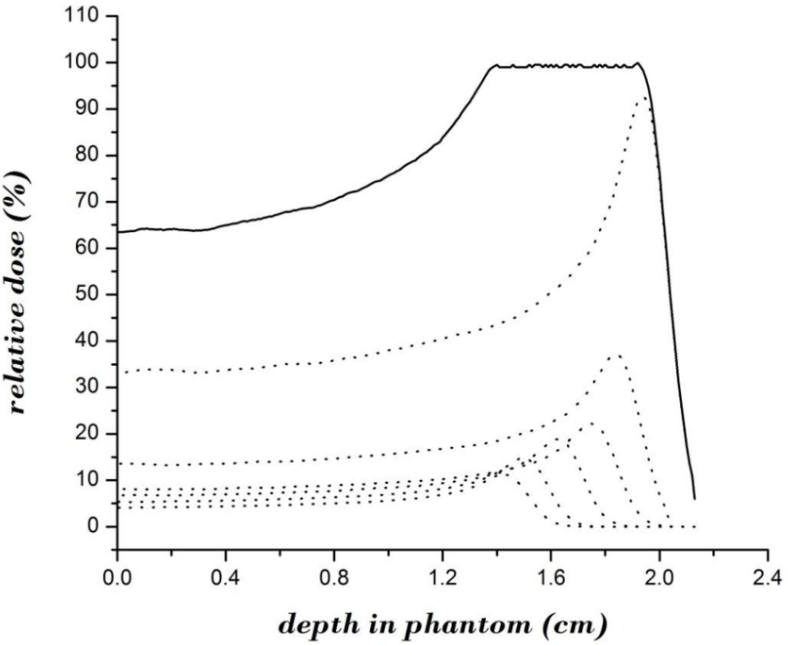

Figure 2.4.: "A typical created SOBP with subplot weighted Bragg peaks", by S F Masoudi et al. [39], used under CC BY 3.0

The SOBP is a modified depth dose distribution created by combining multiple quasi-monoenergetic proton beams. This method produces a wider and more evenly distributed energy deposition profile. The SOBP is mainly used to ensure that the entire tumor volume receives uniform and consistent radiation, which is essential for an effective treatment. Implementing the SOBP technique involves adjusting the energies of the individual proton beams so that their Bragg peaks overlap, collectively covering the entire tumor volume and providing a homogeneous dose distribution throughout the target area [16].

3. Radiation Therapy

Radiation therapy is a standard cancer treatment that uses radiation to target and eliminate cancerous cells. In this chapter, the essential concepts related to radiation therapy, including dosimetry, absorbed dose, equivalent dose, and effective dose are covered. The concept of radiobiology and and the physical properties of radiation, such as Linear Energy Transfer (LET) and Relative Biological Effectiveness (RBE) will be also discussed.

3.1. Dosimetry

Radiation dosimetry is the process of measuring, calculating, and evaluating the absorbed dose of ionizing radiation. This is a crucial aspect of radiotherapy, where the aim is to improve the effectiveness of cancer therapy while minimizing the risk of severe adverse effects among patients [40]. Moreover, it is of significant value in other medical fields, such as diagnostic radiology [41] and nuclear medicine, where the principle of limiting exposure "as low as reasonably achievable" (ALARA) is of utmost importance [42].

The International Commission on Radiological Protection (ICRP) has introduced several dosimetric quantities and units to describe radiation beams [43, 44, 23]. The most commonly used dosimetric quantities and their units are defined in the following sections.

3.1.1. Absorbed Dose

The absorbed dose is a measure of the energy deposited per unit of mass, denoted by the unit Gray (Gy) with the dimension of Joule per kg. As defined by Equation (3.1), it represents the average energy ΔE deposited by ionizing radiation within a volume V of mass Δm [45].

$$D = \frac{\Delta E}{\Delta m} \tag{3.1}$$

The absorbed dose is the fundamental physical dosimetric quantity, but it cannot be directly used for radiation protection since various types of ionizing radiation have different effects on damaging human tissue [45]. Therefore, the concept of equivalent dose was introduced to account for these differences and provide a more accurate measure of radiation exposure for radiation protection purposes.

3.1.2. Equivalent Dose

The concept of equivalent dose H_{T} takes into account the biological effects of a specific type of radiation when compared to the same absorbed dose, providing a clearer indication

of the potential radiation risk. It is necessary to consider this factor because the damage caused by the same dose of radiation to an organ from neutrons or α radiation is more severe than that caused by γ radiation or electrons [45]. The equivalent dose is given as the product of the absorbed dose D_{T} and the radiation-dependent weighting factor w_{R}.

$$H_{\mathrm{T}} = w_{\mathrm{R}} D_{\mathrm{T}} \tag{3.2}$$

Since the weighting factor w_{R} is dimensionless, the equivalent dose H_{T} retains its unit of joule per kilogram. However, to differentiate between absorbed dose and equivalent dose, the unit of equivalent dose is referred to as Sievert (Sv) [45]. The tissue weighting factors w_{R} are listed in Table 3.1.

Radiation type	**Weighting factor** $w_{\mathbf{R}}$
Photons	1
Electrons and muons	1
Protons and charged pions	2
Alpha particles and heavy ions	20
Neutrons	5-20

Table 3.1.: Radiation weighting factors as defined by the International Commission on Radiological Protection (ICRP) in the ICRP Publication 103 (ICRP 2007) [46]

.

3.1.3. Effective Dose

The concept of effective dose E, introduced by the ICRP in 1977 [43], considers the sensitivity of organs and tissues to radiation through the use of tissue-dependent weighting factors. These tissue weighting factors w_{T} represent the relative contribution of an organ or tissue to the total damage due to the effects resulting from a uniform irradiation of the whole body. At low doses, the individual organ or tissue damage is additive, and the total damage to the whole body is the sum of the individual damage [45], as given by Equation (3.3):

$$E = \sum_{\mathrm{T}} w_{\mathrm{T}} * H_{\mathrm{T}} \tag{3.3}$$

where H_{T} represents the equivalent dose of a particular type of radiation. Equation (3.3) can be expanded to consider multiple types of radiation. The tissue weighting factors w_{T} are given in Table 3.2.

Tissue	**Tissue weighting factor** $w_{\mathbf{T}}$	$\sum w_{\mathbf{T}}$
Bone-marrow (red), colon, lung, stomach, breast, remaining tissues.	0.12	0.72
Gonads	0.08	0.08
Bladder, Oesophagus, Liver, Thyroid	0.04	0.16
Bone surface, Brain, Salivary glands, Skin	0.01	0.04
Total		1.00

Table 3.2.: Tissue weighting factors according to ICRP 103 (ICRP 2007) [46].

3.1.4. Dose-to-Water

In radiotherapy, doses are typically expressed as water-equivalent dose, also known as dose-to-water D_{w}, for historical reasons [47, 3] and because the human body is mostly composed of water. Commercial treatment planning systems typically model the structures of the human body as water voxels with varying mass density, electron density or stopping power, while the real tissue composition varies significantly. Monte Carlo codes, such as FLUKA, calculate the dose in the medium D_{m}, taking into account material properties such as composition, mass density and ionization potential, which allows for more accurate reflection of particle interactions. However, most of the clinical experience is based on dose-to-water calculations, and commissioning, quality assurance and absolute dose measurements in radiotherapy centers are done in water [48, 47, 3]. Consequently, a conversion of the dose-to-medium into dose-to-water is necessary for a direct comparison of results from Monte Carlo simulations to the treatment planning system. Several methods have been previously employed to integrate the calculation of dose-in-water into FLUKA, as detailed in [48, 49], for which a specialized routine was implemented to directly multiply the fluence Φ_{m} of charged particles in a given medium by the Linear Energy Transfer (LET) of the particles in water [48]. Recent developments of FLUKA in the field of particle therapy have introduced a more user-friendly method for calculating the dose-to-water via the use of a USRBIN score card, which has already been pre-defined. This method is called on-the-fly conversion from D_{m} to D_{w}, and considers all the elements of the mixed-radiation field generated by the primary beam, as well as the secondary particles and fragments that undergo nuclear reactions in a patient voxel geometry [50, 3]. The on-the-fly conversion from D_{m} to D_{w} is given by Equation (3.4)

$$D_{\mathrm{w}} = \sum_{\mathrm{i}} \int \Phi_{\mathrm{m,\,i}}(E) \frac{S_{\mathrm{w,i}}(E)}{\rho} \,\mathrm{d}E \tag{3.4}$$

where the dose-to-medium is converted into dose-to-water by weighting the track-length with the stopping power in water $S_{\mathrm{w,i}}$ at each step, regardless of the material present at the step location.

3.1.5. Water Equivalent Thickness

As already discussed, water is a material frequently used in radiotherapy to evaluate the distribution and range of radiation doses due to its similarities with human tissues [51]. Water shows characteristics such as energy loss, multiple Coulomb scattering, and nuclear interactions, which are comparable to those of human tissues. The Water Equivalent Thickness (WET), denoted by t_w, is a parameter employed in the characterization of the penetration range for clinical proton beams. It enables the analysis and comparison of range losses in various beamline components and in the patient [16]. A schematic representation of WET is presented in Figure 3.1

Figure 3.1.: Schematic illustration of the concept of WET [52].

The general equation for the definition of the Water Equivalent Thickness of a material is given in Equation (3.5):

$$t_w = t_m \frac{\rho_m S_m}{\rho_w S_w} \tag{3.5}$$

where the mass densities of water and the given material are represented by ρ_w and ρ_m, and S_w, S_m denote the mean proton mass stopping power of water and the material, respectively. An approximate method for predicting the WET using the ratio of continuous slowing down approximation (CSDA) ranges in water and the material of interest [52] was proposed by the International Atomic Energy Agency (IAEA) [51] and is defined as follows:

$$t_w = t_m \frac{\rho_m}{\rho_w} c_m \tag{3.6}$$

As already mentioned, the Water Equivalent Thickness of a material is denoted as t_w, while its physical thickness is represented by t_m. The mass densities of both water and the given material are represented by ρ_m and ρ_w. Finally, c_m is a depth scaling factor defined by the ratio of the Continuous Slowing Down Approximation (CSDA) in water to the target material, as given in Equation (3.7).

$$c_m = \frac{\rho_w R_w}{\rho_m R_m} \tag{3.7}$$

This approach is only valid for targets thick enough to stop the beam completely, also known as stopping-length targets. In clinical applications of proton therapy, it is possible to determine the (WET) values by analyzing the range shift resulting from introducing a test object. This technique involves performing a pair of measurements under identical conditions, with the only difference being the introduction of the test material. The resulting range shift in a water phantom corresponds to the WET value [52, 16].

3.2. Radiobiology

The field of radiobiology studies the impact of ionizing radiation on living organisms and biological tissues. It is an interdisciplinary field that combines radiation physics and biology [23]. The effect of ionizing radiation on cells and genetic material (DNA) is based on the physical principles described in Chapter 2. Cells and genetic material can be damaged by ionizing radiation. If the damage is not repaired, it can lead to cell death or changes in the DNA called mutations. There are two ways in which this harm can occur: direct and indirect action. Direct action occurs when the radiation interacts directly with a critical target within the cell, leading to a chain of physical and chemical events resulting in biological damage. Indirect action, on the other hand, happens when radiation interacts with other molecules and atoms inside the cell, producing Hydroxyl radicals [53, 23]. These free radicals can then diffuse and damage the key targets within the cell by breaking chemical bonds and causing chemical changes [23]. The kind of action that specific types of radiation take on a cell is closely related to the LET of the particle.

3.2.1. Linear Energy Transfer

The Linear Energy Transfer (LET) is a parameter defined by the International Commission on Radiation Units and Measurements (ICRU), often used in medical physics and radiobiology to quantify the amount of energy deposited per unit distance traveled by a charged particle in a particular medium. It determines the average rate at which energy $\mathrm{d}E_{\mathrm{L}}$ is deposited locally along the path $\mathrm{d}x$ of a charged particle of a given energy, and it sets a limit on the distance from the track beyond which energy deposition will not be included or the maximum value of discrete energy loss by the particle beyond which losses will no longer be considered as local [21]. The Linear Energy Transfer is defined in Equation (3.8):

$$\mathrm{LET} = \frac{\mathrm{d}E_L}{\mathrm{d}x}. \tag{3.8}$$

Although LET is closely related to linear stopping power, it focuses on the amount of energy deposited due to electronic interactions without considering the energy loss caused by nuclear interactions. The delimitation of energy deposition that is considered for LET is established by excluding the energy deposition of high energetic secondary electrons, also known as δ-rays [54]. In the field of radiation biology, LET has an important role in understanding the biological effect of radiation, as it determines the rate at which energy

is transferred to the medium in a localized area. This characteristic is significant because the energy must be locally delivered to a specific cell in order to cause damage [21].

Particles are classified into two groups based on their Linear Energy Transfer: high LET radiation causes more ionization events by depositing a larger amount of energy per unit length along its path. As a result, this leads to a higher concentration of energy deposition, which can cause more severe damage to biological structures near the particle track, such as double-strand breaks and base damage to the DNA molecule [21]. When high LET particles interact with biological material, the dominant process of cell damage is direct action [23]. In contrast, low LET radiation tend to generate uniform and widespread ionization throughout the tissue, mainly resulting in single-strand breaks [21, 55, 56]. The majority of the biological damage caused by low LET particles is due to indirect action [23]. Electrons, X-rays, and γ-rays are typically associated with low LET, whereas high LET is commonly associated with protons and α-particles. The LET associated with X-rays, γ-rays, and neutrons arises from the secondary charged particles that are produced when the primary particles interact with the surrounding medium or tissue [21].

3.2.2. Relative Biological Effectiveness

Relative biological effectiveness (RBE) is defined as the ratio of the absorbed dose of a specific type of radiation to a reference absorbed dose that produces an equivalent biological effect under uniform conditions [34], as given by Equation (3.9):

$$\mathrm{RBE} = \frac{D_{\mathrm{R}}}{D_{\mathrm{x}}} \tag{3.9}$$

The absorbed dose of the particular type of radiation and of the reference radiation are denoted by D_{x} and D_{R}, respectively. X-rays with an energy of 250 keV or cobalt-60 gamma rays are frequently utilized as the reference radiation. In clinical settings, proton therapy employs a constant RBE value ranging between 1.1 and 1.2 [56], as recommended by the ICRU [44]. This value is used to calculate the clinically prescribed dose, which is referred to as the biological dose D_{Bio} or isoeffective dose, as given by:

$$D_{\mathrm{Bio}} = \mathrm{RBE} \cdot D_{\mathrm{Physical}} \tag{3.10}$$

It is important to note that even when a constant RBE value is typically employed, the RBE depends on a variety of factors. These factors include the type and quality of radiation, which are measured by Linear Energy Transfer (LET), as different types of radiation transfer energy differently. Additionally, the RBE can be influenced by the total dose, dose per fraction, presence or absence of oxygen, and the specific tissue or cell in which the radiation dose is deposited [21, 34].

4. Medical Imaging and Treatment Planning

4.1. Medical Imaging

Improvements in imaging techniques and instrumentation have revolutionized early diagnosis and treatment of various medical conditions [57]. Different techniques can be employed based on the specific information needed, and the selection of imaging technique and instrumentation should be carefully evaluated for their impact on diagnosis. The most commonly used modalities are computed tomography (CT), positron emission tomography (PET), magnetic resonance imaging (MRI) and ultrasound. In radiotherapy, CT is the gold standard because of its ability to provide tissue density information [57, 48].

4.1.1. Computed Tomography

Computed tomography (CT) is a medical imaging technique used to obtain detailed internal 3D-images of the body. CT scans have a wide range of applications, including the detection and diagnosis of various medical conditions, such as tumors, and the planning of radiotherapy treatments [17]. The basic principle behind CT image acquisition involves measuring the spatially dependent X-ray attenuation coefficients μ, which result from the interaction of X-ray beams with a patient [57]. A detector array consisting of multiple solid-state detectors is positioned opposite the X-ray tube, both of which are mounted inside the gantry. The X-ray tube rotates around the patient, continuously collecting data from multiple angles [17]. The acquired data is then used to reconstruct a CT matrix using a computer reconstruction technique, resulting in a cross-sectional image typically consisting of 512×512 or 1024×1024 pixels. CT scanners operate in the range of 70 kV to 140 kV and a tube current between 70 mA up to 320 mA, with the exact value being tailored to the size of the patient [57]. The values assigned to each pixel in a CT image are associated with the linear attenuation coefficient μ of the corresponding tissue, which depends on the density and composition of the material in addition to the photon energy [17], according to the Beer-Lambert law (4.1):

$$I(x) = I_0 e^{-\mu x} \tag{4.1}$$

where $I(x)$ is the intensity of the attenuated beam, I_0 is the intensity of the original beam, and x is the thickness of the material. Since most X-ray sources and tubes produce polyenergetic beams, the Beer-Lambert law should be integrated over all photon energies in the X-ray spectrum. Most CT reconstruction algorithms, however, use an alternative approach in which the average photon energy of the spectrum is used instead [17]. A

detailed description of reconstruction algorithms is beyond the scope of this thesis. The characteristic third dimension of CT images results from the movement of the patient's table in a horizontal direction as the images are acquired [57]. The position of the patient on the table is an important factor in the treatment planning process and is recorded along with the scan data [17].

The reconstructed CT image is composed of multiple slices, each representing a specific plane in the body of the patient and displaying the anatomy at a particular level. The thickness of the slice is selected to reduce scatter radiation and overlapping by using collimators. Typically, it ranges between 1 mm to 5 mm and is determined by the operator based on clinical examination requirements [58]. Figure 4.1 illustrates this concept showing a CT image of a head at different slices of the image.

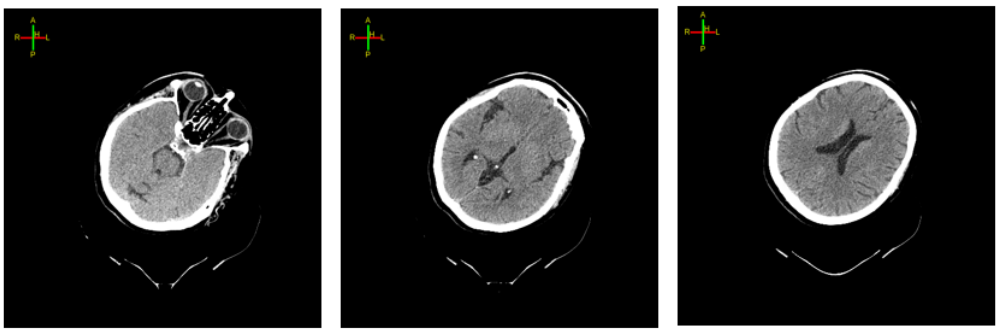

Figure 4.1.: CT image of head at different slices.

4.1.2. Hounsfield Units

For the purpose of comparison and interpretation of CT images acquired by the same or by different scanners, it was necessary to have a standardized scale of measurement. Godfrey Hounsfield introduced the Hounsfield units (HU), also known as CT numbers, as a relative quantitative measure of radiodensity. The Hounsfield scale relates the average attenuation coefficient of X-rays within tissue relative to water. A Hounsfield unit is defined by Equation (4.2), as:

$$\mathrm{HU}_{\mathrm{material}} = \frac{\mu_{\mathrm{material}} - \mu_{\mathrm{water}}}{\mu_{\mathrm{water}}} \times 1000 \tag{4.2}$$

where μ_{water} and μ_{material} are the linear attenuation coefficients of the water at room temperature and the material, respectively. Water and air have assigned values of $\mathrm{HU}_{\mathrm{water}} = 0$ and $\mathrm{HU}_{\mathrm{air}} = -1000$ [17]. In a CT image, materials with a lower attenuation coefficient than water are represented by negative numbers and appear as dark shades of gray, with air appearing as black. Whereas, materials with a higher attenuation coefficient than water are represented by positive numbers and appear as lighter shades of gray up to white in the CT image [58].

4.1.3. DICOM Standard

CT scans, among many other medical imaging procedures that require image reconstruction, are based on digital storage rather than traditional photographic plates. These developments in medical imaging, along with the wide range of specialized equipment offered by multiple manufacturers implementing different approaches, have created the need for a standard that enables and simplifies the exchange of medical data [59]. The Digital Imaging and Communication in Medicine (DICOM) standard serves as a crucial format for medical images, facilitating the storage, exchange, and management of medical images and associated information [60]. DICOM standardizes medical information and technical specifications into modules. These modules consist of lists of attributes that encode specific details within common categories, such as patient-specific information, device details, type of examination, and the relationships between these types of information [17]. In addition, DICOM enables communication between medical imaging devices, diagnostic systems, and therapy systems. This is particularly important in radiotherapy, where treatment planning can be based on the CT images of the patient. This is made possible by the compatibility of image formats supported by DICOM [61]

4.2. Treatment Planning

Treatment planning is the process used to program a radiation therapy machine to deliver a precise radiation dose to a patient, or more specifically, to a defined area of the patient undergoing treatment. The treatment planning workflow consists of a series of steps that require detailed knowledge of the patient's anatomy and system specifications. This knowledge is used to determine the optimal system configuration for delivering an appropriate dose to the target structures while minimizing damage to healthy tissue [62]. A flowchart describing the treatment planning workflow is shown in Figure 4.2.

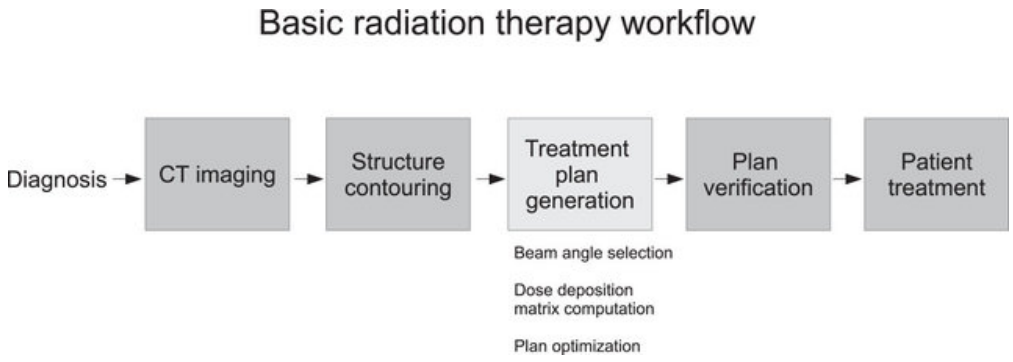

Figure 4.2.: Radiation therapy workflow by David Craft et al. [63], used under CC BY 4.0

As mentioned in Chapter 4.1.1, the radiotherapy treatment planning process is based on the patient's CT images. Using the DICOM standard, these images can be imported directly into a treatment planning system where the various regions of interest (ROI),

organs at risk (OAR), and target volumes (RV) must be delineated before the beam configuration and dose distribution can be defined and optimized [45]. This involves calculating the most effective beam angles, intensities, and shapes to achieve the best possible therapeutic outcome. The entire process is iterative and often requires a number of adjustments and evaluations in order to refine the plan. From the CT data, a user-defined mass density to HU calibration curve defined in the treatment planning system is used to interpret the material information used in the dose distribution calculations [64]. There are currently a number of commercial planning systems available on the market. These systems typically differ in the radiation dose calculation algorithms used and the way they are implemented [65]. Within the framework of this thesis, the treatment planning system RayStation [66] is used.

4.2.1. Calibration Curve

In order to be used as a base for the dose distribution calculations by the treatment planning system, the Hounsfield units (HU) in each volume element (voxel) of a CT image need to be converted to mass density ρ, a process defined by the mass density ρ to HU calibration curve, also known as the HU calibration curve. This correlation between tissue mass density ρ and Hounsfield units is crucial in computed tomography, since it allows the conversion of tissue composition into numerical values for representing anatomical structures and pathological findings in medical imaging. As mentioned in Chapter 4.1.2, the CT number depends not only on the attenuation properties of the medium, but also on several other factors such as scanner type, tube voltage, field of view (FOI), and reconstruction algorithm [67]. As a result, the CT number of a given tissue is not constant but rather scanner- and study-dependent [68].

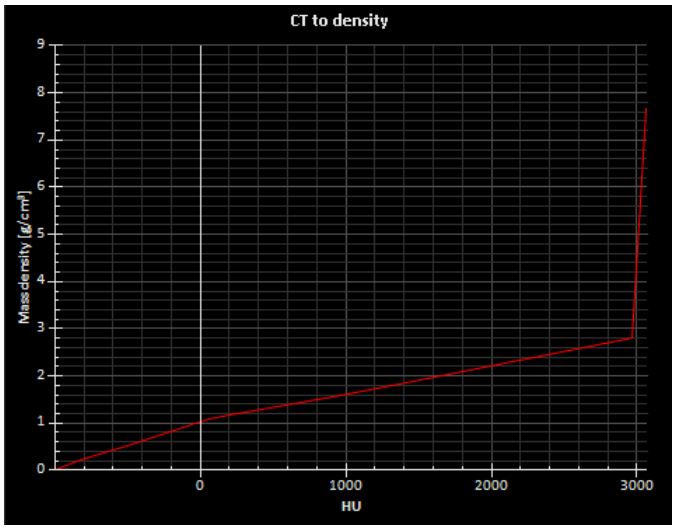

Figure 4.3.: Mass density to HU calibration curve for the MA/Adult Head protocol.

The process of generating such a calibration curve involves the scanning of a phantom

with inserts of tissue-equivalent materials of known composition, and relating the density of those materials to the obtained CT number. The results are typically presented as a graph of the mass density ρ as a function of the Hounsfield unit (HU), as illustrated in Figure 4.3.

The relative stopping power values necessary for treatment planning and dose calculation are frequently calculated on a voxel-by-voxel basis, using stoichiometric calibration. The composition and density of standard adult tissues are typically employed as a reference point. Nevertheless, it is commonly assumed that the compositional inserts of the calibration phantoms are representative of tissues of all ages and sexes. This assumption overlooks the fact that female, male, and pediatric tissues differ in density and composition. Some centers employ a smaller electron density phantom to calibrate the CT to small patients [69]. Additionally, the adjustment of parameters utilized in CT scanning protocols is employed to account for these differences.

4.2.2. Structure Definition and Contouring

Structure definition and contouring represent a fundamental aspect of the treatment planning process, as they serve as the basis for the prescription, documentation, and implementation of the treatment plan [45]. The contouring of structures and volumes is conducted by a medical physicist, radiation technologist or radiation oncologist directly over the CT images in the treatment planning software. The ICRU Reports No. 50 [70] and 62 [71] defined multiple volumes for treatment planning, which serve as a basis for comparison between treatment outcomes. These structures include the gross tumor volume (GTV), the clinical target volume (CTV), and the planning target volume (PTV). In addition, organs at risk (OAR) must be carefully considered and delineated for treatment planning [45]. A brief description of these structures and concepts is provided in the following sections and illustrated in Figure 4.4

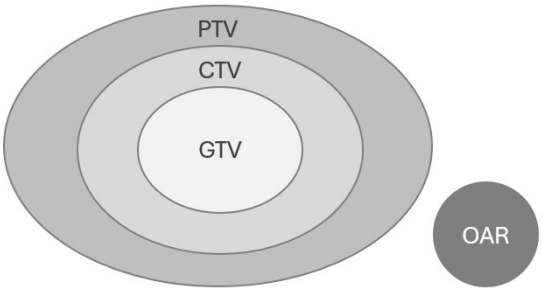

Figure 4.4.: Irradiation volumes of interest, as defined in ICRU Report No. 50.

- **Gross Tumor Volume (GTV):** The gross tumor volume is defined as the extent and location of the tumor [45, 70, 71].

- **Clinical Target Volume (CTV):** The clinical target volume includes the area immediately surrounding the GTV, which may contain disease contamination. It is usually described as a margin around the GTV, the extent of which is determined by a radiation oncologist [45, 70, 71].

- **Planning Target Volume (PTV):** The planning target volume takes into account the net effect of all possible geometric variations to ensure that the prescribed dose is actually absorbed in the clinical target volume; it includes the clinical target volume and a margin for uncertainty, machine tolerances, and in treatment variations [45, 70, 71].

- **Organs At Risk (OAR):** Organs at risk are those whose sensitivity to radiation is such that the dose received from a treatment plan may be significant compared to their tolerance. This may require a change in beam delivery or dose [45, 70, 71].

- **External Region Of Interest (External ROI):** The external region of interest is defined as the delimitation of the patient. All other relevant structures such as target ROIs and OARs must be covered by the external ROI [45, 70, 71].

- **Regions Of Interest (ROI):** The regions of interest include all structures relevant to radiotherapy, such as body contours, PTVs, GTVs, and OARs [45, 70, 71].

4.2.3. Dose Planning

The process of dose planning, calculation and optimization can begin once the target volume and regions of interest have been delineated. Based on the patient geometry and defined structures, the beam entrance fields can be defined according to several principles: the dose should be delivered homogeneously to the tumor volume using either a single-field direction or a multi-field direction approach (as depicted by Figure 4.5) for which is important to consider and minimize the effects on low-dose regions and to spare normal tissue. In addition, the shortest possible beam path should be used, avoiding highly heterogeneous areas that may distort the shape of the Bragg peak.

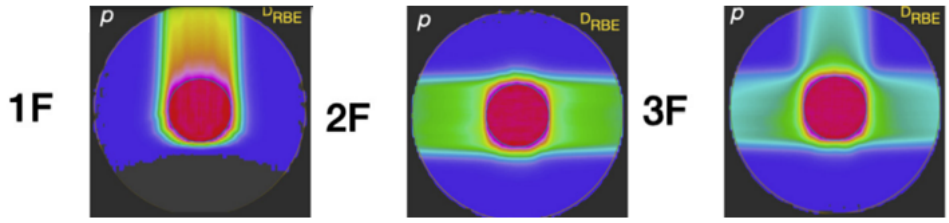

Figure 4.5.: D_{RBE} for intensity modulated particle therapy for a proton beam using single and multi-field by Stewart Mein et al. [72], modified and used under CC BY 4.0

The purpose of dose calculation and optimization is to ensure that the necessary dose is delivered to achieve the therapeutic effect while also considering the constraints of the surrounding normal tissues. This is carried out by the treatment planning system, which assigns energy, number of particles, and transverse position to each monoenergetic beam. The medical treatment planner needs to determine specific targets and constraints for optimization, which will be used as a base for the treatment planning system to optimize the dose distribution. This provides the best field shapes, beamlet weights, particle fluence, etc. based on the dose planning method [3]. Dose planning methods such as pencil beam and Monte Carlo based TPS are described in Chapter 5.

5. Materials and Methods

The goal of this thesis was the commissioning of certain input parameters to enable the recalculation of MedAustron treatment plans using the Monte Carlo code FLUKA. Specifically, I focused on adapting and validating input CT calibration curves, and assessing their impact on the simulated dose distributions.

The materials and methods used in this thesis are detailed in this chapter. The first section explains the fundamentals of the Monte Carlo method 5.1 and provides a description of the relevant softwares: FLUKA 5.1.1 and the treatment planning system RayStation 5.1.2. It emphasizes the mathematical and physical models used as the basis for their dose calculations as well as their approach to handling DICOM data. Then, the workflow for calibration curve adjustment and verification as well as the implemented methods are presented in Section 5.2, 5.2.1 and 5.2.2. The process of dose recalculation with FLUKA is described in Section 5.2.3, Finally, a short description of a simulation using the beam model is given in Section 5.4.

5.1. Monte Carlo Method

Monte Carlo (MC) methods are computational techniques that use random numbers to solve mathematical problems, including numerical integration and stochastic optimization. They are also widely used to simulate physical, chemical, and biological systems. The underlying principle of the Monte Carlo method is the Law of Large Numbers, which states that the expected value $E(X)$ of a random variable X with a probability density function $f(x)$ is approximately given by the average value $\bar{x}$ if the experiment were to be repeated infinitely often [73]. The expected value $E(X)$ of X is calculated by Equation (5.1):

$$E(X) = \int x f(x) \mathrm{d}x \tag{5.1}$$

where the integral is done over all possible values of X. In the case of discrete random variables, the integral is replaced by a summation [73], resulting in:

$$E(\varphi(X)) = \lim_{\mathrm{inf} \to \infty} \frac{1}{n} \sum_{i=1}^{n} \varphi(X_i) \tag{5.2}$$

On the other hand, the average value $\bar{x}$ of the results of n is given by:

$$\bar{x} = \frac{1}{n} \sum_{i=1}^{n} \varphi(X_i) \tag{5.3}$$

Hence, according to the Law of Large Numbers [74], for an infinite number of results ($n \to \infty$), the mean approaches the expected value, as shown in Equation (5.4).

$$\lim_{n\to\infty} \Rightarrow \bar{x} = E(\varphi(X)) \tag{5.4}$$

The statistical uncertainty of the expected value is calculated using the Central Limit Theorem, which is given by Equation (5.5) [73, 3].

$$\lim_{n\to\infty} P(\bar{x}) = \frac{1}{\sqrt{2\pi\sigma(x)^2/n}} e^{-\frac{(\bar{x}-E(x))^2}{2\sigma(x)^2/n}} \tag{5.5}$$

which states that as n approaches infinity, the mean of n identically distributed independent random variables converges to a normal distribution with mean $\bar{x}$ and variance $\sigma(x)^2/n$.

A physical problem must first be formulated mathematically, typically as an equation or system of equations, to be solved using the Monte Carlo method [75]. In medical physics, Monte Carlo simulations have become an essential tool, especially in the context of particle therapy, where they are used to commission clinical facilities, design beamlines, delivery systems, and determine radiation protection parameters. In addition, MC codes can be used as a tool to validate, improve and commission analytical treatment planning systems [4]. The schema for solving physical problems using Monte Carlo simulations is as follows [75]:

1. The problem is formulated mathematically by developing a fitting model that describes of the phenomenon.
2. A statistical interpretation of the problem is formulated, expressing the quantity of interest as a parameter of a distribution.
3. A sampling algorithm is developed.
4. Estimators for the value and its statistical and statistical uncertainty derived. These can be the sample average and variance, for example.
5. The algorithm is optimized to achieve the desired level of statistical uncertainty for the available computational time.
6. A statistically significant sample is created.
7. The sample is used to generate the parameter and its uncertainty.

The radiation transport mechanism is a random process, which makes it an excellent application for Monte Carlo calculations. Applying this scheme to the case of calculating the dose distribution from a radiation source, the initial parameters of a particle would be sampled from the distribution characterizing the source. Then, a particle trajectory would be generated by simulating the actual process in order to calculate the dose delivered by that particle. By generating a sufficiently large number of trajectories, the desired level of statistical uncertainty in the calculated dose distribution would be achieved [75].

5.1.1. FLUKA

With roots dating back to the 1970s, FLUKA [76] is a general purpose Monte Carlo code developed jointly by the European Organization for Nuclear Research (CERN) and the Italian Institute for Nuclear Physics. The code is capable of describing the particle transport and interaction with matter of about 60 different particle species and heavy ions in the energy range from 1 keV to 20 PeV. All particles are tracked with high accuracy within complex geometries created by the combinatorial geometry package [3]. FLUKA implements modern physical models that follow a microscopic approach, which ensures the consistency of all reactions and compliance with conservation laws. The versatility of FLUKA covers a wide range of applications, including acceleration physics, detector design, calorimetry, activation, dosimetry, radiation protection, cosmic rays, neutrino physics and radiotherapy [77]. In the field of radiotherapy, FLUKA has been tested with depth dose distributions and beam lateral profiles from research and clinical particle beam therapy accelerators for protons, carbon and several other light ions [6]. A description of the physical models relevant for particle transport calculations of dose distributions in the therapeutic setting is given by Kozlowska [3] and in more detail by Battistoni [4] as described below:

- **Electronic Stopping Power:** when calculating electronic stopping powers, FLUKA starts from the Bethe-Bloch formalism discussed in Chapter 2.4.1, incorporating corrections and avoiding approximations by retaining all terms in the equation to achieve higher precision. The Bethe-Bloch formula, including the modifications proposed by the International Commission on Radiation Units and Measurements (ICRU) [78] and by Ziegler [79] for the low energy range, as used in FLUKA, is given by:

$$\left(\frac{dE}{dx}\right)_0 = \frac{2\pi n_e r_e^2 m_e c^2 z^2 z_{\text{eff}}^2}{\beta^2}\left[\ln\left(\frac{2m_e c^2\beta^2 T_{\max}}{I^2(1-\beta^2)}\right) - 2\beta^2 + 2zL_1(\beta) + 2z^2 L_2(\beta) + K_M(z,\beta) - 2\frac{C(\beta)}{Z} - \delta(\beta)\right] \tag{5.6}$$

  β is the projectile velocity relative to the speed of light, $n_e = \frac{\rho N_{\text{Av}} Z}{A}$ is the electron density of the target material, $I = 75\,\text{eV}$ is the mean excitation energy as proposed by the ICRU [78], M is the projectile mass, and $T_{\max}$ is the maximum energy transfer to a stationary electron. The density correction δ depends on the polarization of the medium and is calculated as proposed by Sternheimer [80]. The shell correction C takes into account the effect of atomic bonds, which is especially important at low energies. C is calculated from the proton stopping power values given by [78]. z_{eff} describes the effective charge due to the partial neutralization of the projectile charge by the charge of the atomic electrons. For protons $z_{\text{eff}} = z$. The correction factor K_m only becomes relevant for medium-heavy projectiles, so it will not be discussed further. Finally, L_1 and L_2 account for the Barkas [81] and Bloch [82] corrections, respectively, as described in [78].

- **Secondary Electrons and Energy Loss Fluctuations:** To account for the fluctuations associated with charged particle energy loss, FLUKA uses an approach [83] that relies on the properties of the cumulants of distributions. The approach can account for an arbitrary threshold for the explicit production of secondary electrons (δ-rays), for arbitrary step-lengths, and for the contribution of distant collisions to the energy loss fluctuations, while ensuring exact compliance with the average restricted stopping power.

- **Multiple Coulomb Scattering:** FLUKA incorporates an extended model [84] for charged particle transport using the Moliere theory [29] to account for multiple Coulomb scattering, as described in Chapter 2.4.2.

- **Nuclear Interaction Models:** FLUKA's nuclear interaction model, known as PEANUT [85], simulates the nuclear environment for interactions involving hadrons, photons, muons and neutrinos from several MeV. At energies relevant for therapy, PEANUT represents the interactions during the stages of a generalized intranuclear cascade (GINC), followed by particle emission based on excitons in a pre-equilibrium phase and an equilibrium phase.

To integrate FLUKA into medical applications, a graphical user interface (GUI), known as Flair, provides the ability to import, manipulate, and view DICOM files [86]. FLUKA's combinatorial geometry package allows users to convert DICOM files into voxel geometry, giving the possibility to edit the geometry or assign materials from built-in libraries, including those from the ICRUs and ICRPs [4]. Further developments of Flair have incorporated several other features that aim to facilitate the use of FLUKA in the clinical workflow. These features, often collectively referred to as "The Particle Therapy Tool" [3], can process dedicated DICOM radiation therapy data as described in the DICOM Radiation Therapy (RT) standard, including the Radiation Therapy Structure module (RTSTRUCT), the Radiation Therapy Dose module (RTDOSE), and the Radiation Therapy Plan module (RTPLAN) [87, 4, 6]. The contents and functions of these modules are described below:

- The Radiation Therapy Structure Module (RTSTRUCT) contains the information necessary to transfer patient structures and related data defined on CT scanners, virtual simulation workstations, and treatment planning systems [60]. It contains both regions of interest and points of interest such as dose reference points. During simulation, the ROIs can be used to calculate Dose Volume Histograms (DVH) or to perform special scoring on an organ-specific basis [4].

- The RT Dose Module (RTDOSE) is designed to store and transfer dose data generated by treatment planning systems (TPS), whether for single or multiple beams [60]. This data, stored as RTDOSE files, can be converted into a FLUKA USRBIN, which is a 3D scoring grid used within FLUKA simulations. Once the RTDOSE data is converted to a FLUKA USRBIN, it can be utilized for plotting and comparing dose distributions [4].

- The Radiation Therapy Plan (RTPLAN) module contains the information on the treatment plans generated by the treatment planning system such as geometric and dosimetric data specifying the course of an external beam, including beam angles, collimator apertures, beam modifiers, and source specifications. It typically references the RT Structure module to define a coordinate system and a set of patient structures [60]. FLUKA is capable of processing the RTPLAN module into a set of input cards that define the beam spots according to the plan. Each beam spot is characterized by a set of parameters and grouped into a beam sequence where they are enumerated by control points. The control point checklist contains several pieces of information, such as particle energy, scan spot position and number of monitor units. In addition, the particle type, the isocenter position according to the DICOM file and the angles of the gantry, the patient and the table are defined for each beam sequence [4].

5.1.2. RayStation

The RayStation treatment planning system (TPS) is a software platform developed, sold and maintained by the Swedish company RaySearch Laboratories AB. It is specifically designed for radiotherapy treatment planning and is capable of supporting multiple therapy modalities such as carbon, helium and proton therapy [64]. In the context of proton therapy, it facilitates the planning and optimization of proton beam plans by allowing the import of patient-specific DICOM files, the definition of Target Volumes and Organs At Risk (which are described in Chapter 4.2.2) and provides a delivery plan based on clinical and machine specifications, taking into account the patient's anatomy, the beam model and the delivery system [88, 64]. Several algorithms have been developed to meet the requirements of different delivery systems, such as Pencil Beam Scanning (PBS), Single Scattering (SS), etc. Relevant for this work is the PBS technique, which achieves a three-dimensional dose distribution by scanning over one layer of the target surface and delivering mono-energetic proton beams with a certain weight. After finishing with that plane, the energy is changed to cover the next area, repeating the process until the entire volume has been irradiated with the prescribed dose. RayStation implements the following physical models and assumptions as a basis for the dose calculations in the context of the Pencil Beam Scanning and Monte Carlo algorithms. These assumptions are taken from [88].

- **Electronic Stopping Power:** The stopping power model is based on the Bethe-Bloch formula omitting the shell C and density ρ correction terms discussed in sections 2.4.1 and 5.1.1.

- **Energy Loss Fluctuations:** The energy loss fluctuations are calculated using the Bohr expression, which assumes a Gaussian distribution of energy loss after passing through a plate of thickness Δz.

- **Multiple Coulomb Scattering:** The lateral spread of the beam caused by multiple Coulomb scattering is treated in the framework of Fermi-Eyges theory. It can only

handle Gaussian distributions and also neglects lateral inhomogeneities.

- **Nuclear Interaction Models:** The Pencil Beam Scanning algorithm represents nuclear interactions by a second lateral Gaussian distribution, which is described by the width σ^{NS} and relative weights ω^{NS} of the nuclear scattering Gaussian. These parameters are given as a function of the initial energy and the depth in water z_{w}. This method is implemented because of the lack of solutions for calculating nuclear scattering effects. However, it underestimates the lateral spread of the nuclear scattering, which can lead to an overestimation of the dose level, especially at lower depths and in small to medium fields.

5.2. Parameter Adaptation and Verification

The following sections provide a detailed explanation of the processes involved in adjusting the mass density ρ to Hounsfield unit calibration curves, as well as validating them using CT scans from two phantoms. The steps of this process follow the workflow:

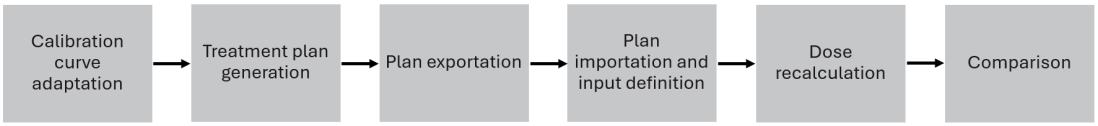

Figure 5.1.: Workflow for adapting the calibration curve to a FLUKA-compatible file.

These steps were repeated for each one of the three calibration curves analyzed in this thesis MA/Adult Head, MA/Pediatric Head and MA/Pediatric Abdomen. The results of the comparisons are presented in Chapter 6.2.

5.2.1. Calibration Curve

As mentioned in Chapter 4.1.1, the mapping between mass density ρ and Hounsfield units (HU) represents a fundamental aspect of computed tomography (CT). It establishes a direct relation that enables the conversion of tissue composition into numerical values. This conversion facilitates the accurate representation of anatomical structures and pathological findings in medical imaging, which serve as the basis for radiation therapy plans and dose calculations. The CT number depends on the attenuation properties of a medium, as well as on a variety of other factors, including the beam energy, the tube voltage, the field of view (FOV), the scattering conditions, and manufacturer-specific CT reconstruction algorithms [89]. As a result, the CT number of a given tissue is not constant but rather scanner- and study-dependent [68].

At MedAustron, the dependence of CT numbers on CT parameters used for image acquisition is accounted for by defining several scanning protocols that result in six different calibration curves for the CT scanner. The available protocols include those for the adult head, adult head and neck, adult abdomen, pediatric head, pediatric abdomen,

and pediatric infant body. The scope of this thesis is limited to the adaptation of the following curves: MA/Adult Head, MA/Pediatric Head and MA/Pediatric Abdomen. These calibration curves are provided in Table 5.1:

		Adult Head	***Pediatric Abdomen***	***Pediatric Head***
Material	**Density ρ (g/cm^3)**	**CT Number (HU)**	**CT Number (HU)**	**CT Number (HU)**
Air	0.001214	-995.64	-979.76	-996.08
Lung IN	0.195	-820.69	-808.61	-821.17
Lung EX	0.51	-502.75	-499.69	-503.04
Adipose	0.96	-63.52	-65.24	-62.71
Breast	0.991	-37.25	-42.17	-36.68
Water	1	4.43	-4.64	4.01
Liver	1.072	48.62	38.22	49.89
Muscle	1.062	51.31	41.79	51.29
Bone200	1.161	204.33	220.17	204.48
Bone800	1.53	910.73	870.65	910.94
Bone1250	1.82	1364.34	1286.55	1365.51
Al	2.8	2972	2972	2972
CT MAX	7.6519		3070	3070
CT MAX	11.163	3070		

Table 5.1.: MedAustron mass density ρ to Hounsfield unit calibration curves for adult head, pediatric head, and pediatric abdomen. The density of the various materials is mapped to a specific CT number for each of the calibration curves.

Table 5.1 lists the mass density ρ of the phantom materials and their corresponding CT numbers at specified settings. Two distinct maximum CT values are presented in the table to address the potential use of implant materials in specific regions of the body. The specific parameters utilized to construct each calibration curve can be found in Appendix A.1.

In the FLUKA code, the conversion of CT numbers into mass density ρ and elemental composition is conducted as the first preparatory step, in which the patient CT data is initially processed and transformed into voxel geometry by dividing the CT scans into a number of HU intervals corresponding to a set of material and compound tables defined in FLUKA [90]. The elemental composition and nominal mean density (i.e. the density corresponding to the HU value at the center of the interval considered) of these materials are taken from the work of Schneider [91], in which 71 human tissues in the HU range between -1000 and 1600 were investigated [90]. Table 5.2 displays the structure and information contained in the FLUKA material tables, using as an example the material defined for CT numbers between 400 HU and 499 HU .

Material properties				
Name:	HU >500			
Density:	1.282808			
Composition:	Mass			
Z	**Atom**	**Element**	**Name**	**Frac**
1		H	Hydrogen	0.076
6		C	Carbon	0.361
7		N	Nitrogen	0.03
8		O	Oxygen	0.38
11		Na	Sodium	0.001
15		P	Phosphorus	0.047
16		S	Sulfur	0.002
17		Cl	Chlorine	0.001
12		Mg	Magnesium	0.001
20		Ca	Calcium	0.101

Table 5.2.: Example of material tables used in the FLUKA code. These tables contain the name and density of the material, as well as its elemental composition. For HU materials, the density corresponds to the nominal density at the center of the range, which is between 400 and 499 HU.

The mass density ρ to HU calibration curves can be added to the configuration of the simulations by means of a configurable material file, which allows the implementation of density correction factors C_ρ to account for possible differences. Since FLUKA has a wider range of materials compared to the ones used for the MedAustron calibration curves (see Table 5.1), it was necessary to interpolate the densities to cover the missing HU ranges. To achieve this, the approach used by Schneider [91] was implemented, where the materials of the calibration curve are categorized as air, lung soft tissue, skeletal tissue, and CT maximum. Within each category, a linear regression was performed, and the resulting equations were utilized to calculate the density ρ of the remaining regions.

Then, the density correction factors C_ρ for the upper and lower limit of each range were determined based on the ratio between the nominal mean densities in the FLUKA material library ρ_{FLUKA_i} and the corresponding densities from the interpolate calibration curve for the same regions ρ_{MA_i}, as described in the following equation 5.7:

$$C_\rho = \frac{\rho_{\mathrm{MA}_i}}{\rho_{\mathrm{FLUKA}_i}} \tag{5.7}$$

The process was repeated for the selected calibration curves, and a material file was prepared for each curve to be imported into FLUKA. An example of the material files, which contains the correction factors, material names, and upper and lower limits for each range, can be found in the Appendix A.2.

5.2.2. Calibration Curve Verification

A CT of a phantom containing six different insert materials with known stopping powers and densities (water, acrylic, Teflon, Lexan, polyethylene, and nylon) was initially used to verify the recalculation of the calibration curves in the material file. The CT scan was conducted using a Phillips CT scanner and then imported into the RayStation treatment planning system by the MedAustron team for quality assurance measurements. Figure 5.2 depicts the phantom with its various regions of interest.

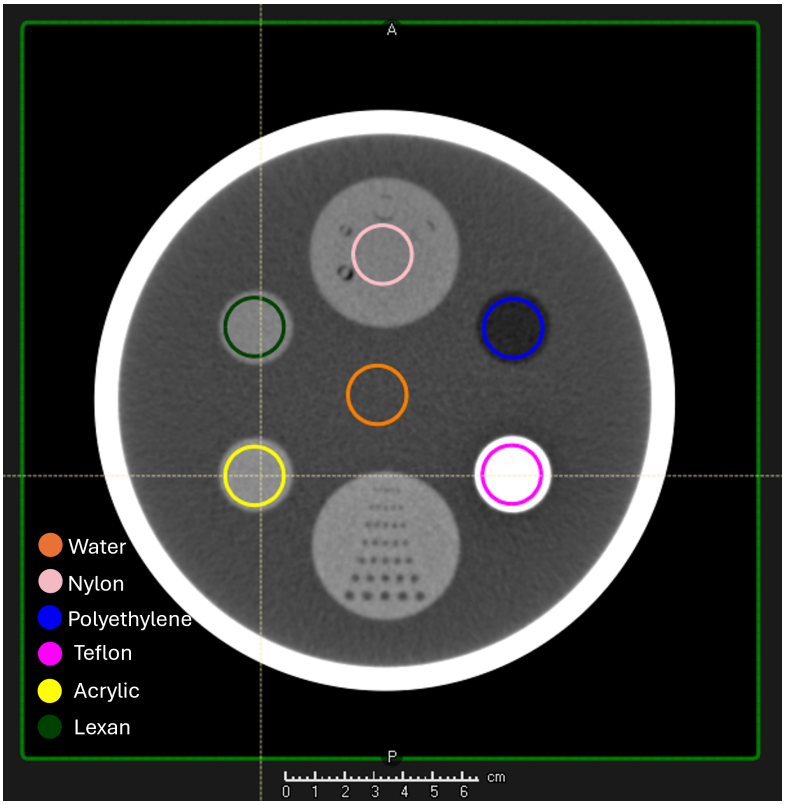

Figure 5.2.: A CT scan of a phantom comprising six materials of known density(water, acrylic, Teflon, Lexan, polyethylene, and nylon). The green rectangle delineating the outer boundary represents the external ROI .

The treatment plans for each material were created using the RayStation treatment planning system with the Pencil Beam Scanner technique (described in Section 5.1.2) only for the MA/Adult Head calibration curve. A plan isocenter was specified at the center of each material. Since the CT scan of the phantom only consisted of four 3 mm-thick slices, it was insufficient to entirely stop the beam for any of the available energies, which range from 62.4 MeV to 252.7 MeV. Therefore, a region of interest (ROI) overwritten with water was defined behind the patient using the patient modeling window of the TPS. Figure 5.3 shows the phantom including the aforementioned water structure.

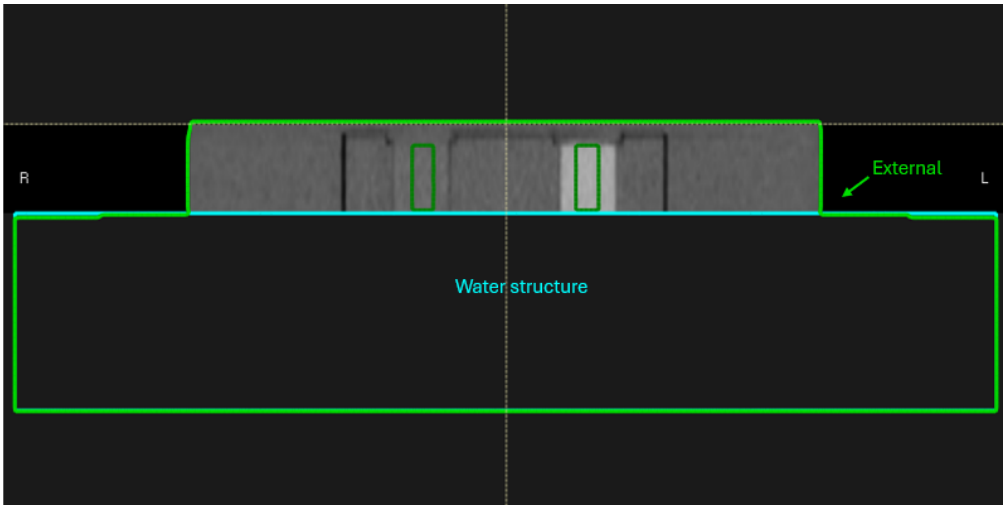

Figure 5.3.: Lateral view of the phantom with the overwritten water structure delineated by the external ROI . The polyethylene and Lexan sample contours are indicated by the two green rectangles in the phantom.

In RayStation, the dose calculation region is limited to the intersection of the dose grid and the region consisting of dose calculation ROIs. In this case, the dose calculation ROIs are limited to the external ROI and no dose is calculated outside the dose calculation region. ROI algebra was used to include the water structure in the dose calculation region by adding the original external contour, defined as the phantom outline, to the water structure using the predefined ROI algebra tool. The dose grid resolution has a minimum value of 1 mm, which was used for all final dose computations. The plans were optimized for the delivery of a 2 Gy physical dose to the selected target. This resulted in the delivery of a set of beams with varying energies and weighting factors, which covered the entire volume. As the objective was not to uniformly irradiate the target volume in accordance with standard clinical practice, but rather to compare the dose distribution of TPS and FLUKA, a single spot of 97.4 MeV was selected and all other spots were manually deleted. Additionally, a number of particles equal to 3000×10^6 were introduced to compensate for the dose. The final dose computations were performed with the RayStation Monte Carlo algorithm, with an average statistical uncertainty of less than 0.5% for voxels with a dose higher than 50% of the maximum dose. The optimization was performed only for the initial plan, i.e., the nylon sample. All further plans were derived from this primary plan by recalculating the final dose after moving the isocenter to the target of the subsequent material with the objective of maintaining a constant plan configuration. All plans were saved and exported as DICOM files.

5.2.3. Dose Recalculation

To set up the simulations, a default Flair voxel input file was created. This file includes optimized physics settings and input cards tailored to medical applications. Specifically

for particle therapy, the "HADROTHErapy" default is optimized with the following specifications [48, 92] to achieve results comparable to those of commercial TPS:

- The electromagnetic module is used for the transport of electrons, positrons, and photons.
- Inelastic form factor corrections for Compton scattering and Compton profiles are enabled. ´
- Low-energy neutron transport down to thermal energies is included.
- Fully analogue absorption for low-energy neutrons is implemented.
- The particle transport threshold is set at 100 keV, except for neutrons (1×10^{-5} eV) and (anti-)neutrinos (0, but they are discarded by default anyway).
- Multiple scattering threshold is set at the minimum allowed energy for both primary and secondary charged particles.
- Delta ray production is turned on with a threshold of 100 keV.
- Restricted ionization fluctuations are activated for both hadrons/muons and EM particles.
- The tabulation ratio for hadron/muon dp/dx is set at 1.03, and the fraction of kinetic energy to be lost in a step is set at 0.02.

Following the preparation of the basic input file, the DICOM files were imported into FLUKA using the Particle Therapy Tool as described in Section 5.1.1. This tool can automatically convert CT slices into FLUKA's combinatorial geometry by generating a voxel file. The file combines the CT data with a predefined material file based on the MA/Adult Head calibration curve to accurately represent different tissues and materials. It achieves this by dividing the CT into voxels and grouping these voxels together into "organs" or groups of voxels made of the same tissue. The water structure was manually specified according to the standard FLUKA procedure, which consists of the definition of three primary input cards: the BODY card, which defines the dimensions, shape and spatial position of the geometry elements; the REGION card, which defines the spatial boundaries by combining these geometry elements through mathematical operations; and the ASSIGNMA card, which assigns the corresponding material properties to the defined regions. The obtained FLUKA combinatorial geometry is shown in Figure 5.4

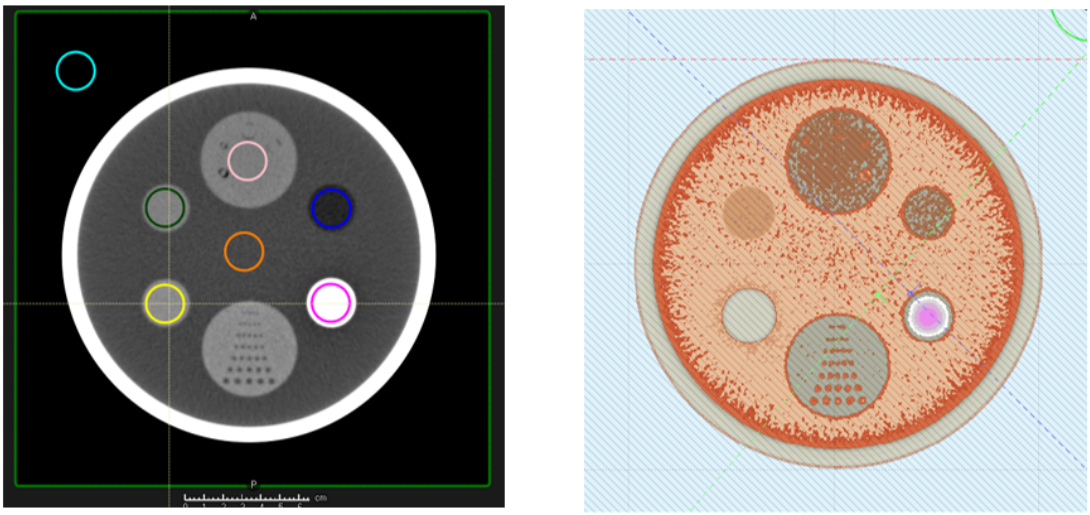

Figure 5.4.: Comparison of CT images of phantom and the phantom converted to FLUKA combinatorial geometry. The FLUKA combinatorial geometry of the phantom includes a dose distribution in the nylon input.

To collect the dose within the phantom, a USRBIN card was also created by extracting the necessary information from the RTDOSE module within the TPS DICOM data. FLUKA's USRBIN card creates a grid over the simulation area and measures the energy deposited into each grid element. In addition, the dose distribution obtained from TPS was converted into a FLUKA USRBIN to facilitate direct comparison. It is important to note that FLUKA allows the evaluation of dose as dose-to-medium and dose-to-water. The second option was chosen to enable direct comparison of the results. The Particle Therapy Tool also processes the information contained in the RTPLAN module to extract source and beam parameters, including position and directional data, from the DICOM files and automatically creates the corresponding input cards. FLUKA allows the beam model definition to be included in the RTPLAN panel, but this was not implemented at this stage of the work. After adding the source and beam data to the FLUKA input, manual adjustments were made to correct the energy.

Nominal energy (MeV)	R_{80} **Energy (MeV)**
62.40	58.98
72.40	69.29
81.30	78.37
97.40	94.71
111.50	109.06
124.70	122.26

Table 5.3.: Nominal and corresponding R_{80} energies established at the commissioning of the facility for the lower energy range.

In Table 5.3, the nominal energy for the spot beam is the energy that the beam has before passing through the nozzle and the air in the room. The R_{80} energy defined in TPS corresponds to the energy of the pre-calculated monoenergetic pristine Bragg peak, which gives the same range as the depth dose curve generated from the corresponding energy histogram. This is the energy used as an input parameter in the FLUKA simulations, meaning that while an energy of 97.40 MeV was selected in TPS, FLUKA was configured with an energy of 94.71 MeV. The simulations were performed with 100,000 primaries over 5 cycles, and repeated for different materials in the phantom. The results were normalized by multiplying the dose with the number of particles specified in the TPS, which is 3000×10^6, as mentioned above in Section 5.2.2, and plotted along the z-axis to obtain the depth dose distribution. To analyze the effect of implementing the calibration curve on the results, each simulation was run again using the example material file provided by the FLUKA developers, which is based on the materials analyzed by Schneider [91], as discussed in section 5.2.1. All other parameters were remaining the same as for the simulations using the material file based on the MA/Adult Head calibration curve. To extract the range of the proton beam for each of the materials, a simple Python script was written and the output was compared to the range extracted from the graph. The results of these simulations and their ranges in water can be found in the Chapter 6.1.

5.3. Dose Distribution Comparison

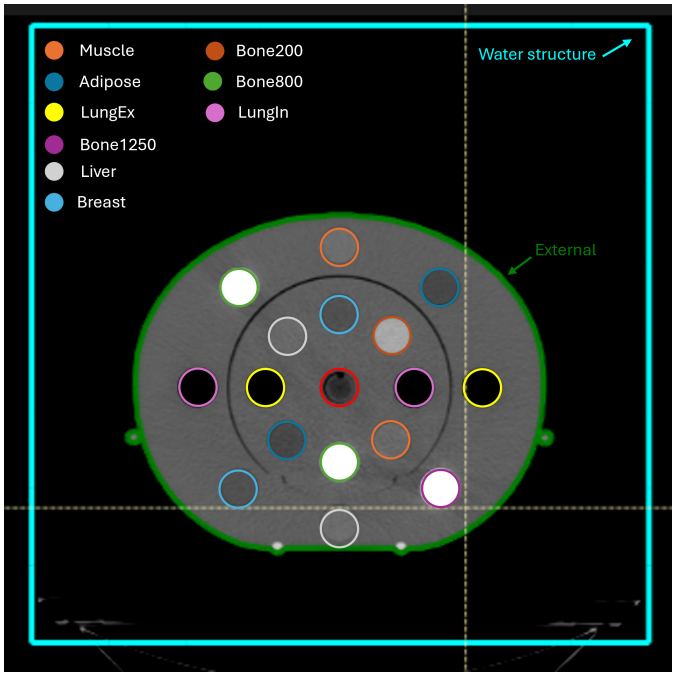

Figure 5.5.: CT scan of a phantom, highlighting the different tissue-equivalent materials. Also shown in this image is the fictive water structure defined in TPS (outlined in blue) and the outer contour (outlined in green).

The dose distribution verification plans for all three calibration curves were made using a different phantom than the one described in Section 5.2.2. The phantom contains inserts composed of different tissue-equivalent materials, that closely resemble the density and elemental composition of human tissue. These materials are commonly used for dosimetric and quality assurance (QA) measurements and were used to create the calibration curves. The inserts include tissue-equivalent materials for muscle, adipose tissue, lung tissues for inhalation and exhalation, breast tissue, liver, and bones with varying densities (Bone200, Bone800, and Bone1250), as shown in Figure 5.5. The CT of the phantom consists of 16 slices, each 3 mm thick, which makes it more suitable for completely stopping the particle beam. However, to account for the low density of the lung inhalation and exhalation inserts, a water structure was also added directly behind the phantom in the RayStation patient modeling panel. To include the water structure in the dose calculation region, the water structure was merged with the external region of interest (ROI) using ROI algebra, which caused parts of the external ROI to extend beyond the top of the image stack where no material override was defined, but still within the external grid, preventing dose calculation. To solve this issue, the top slice of the phantom had to be removed from the external ROI to allow for dose calculation. This problem and its solution are illustrated

in Figure 5.6 and Figure 5.7.

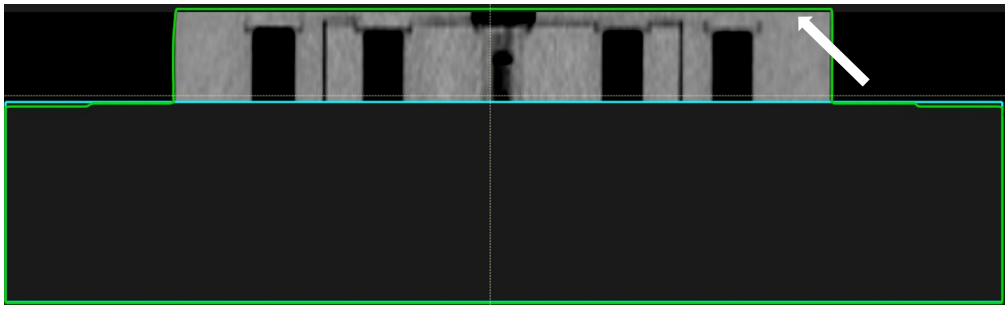

Figure 5.6.: Side view of the phantom including the water structure (defined by the blue outline) and the extended external ROI (defined by the green outline). Note that the external ROI extends beyond the image stack in the upper part of the image, as indicated by the white arrow.

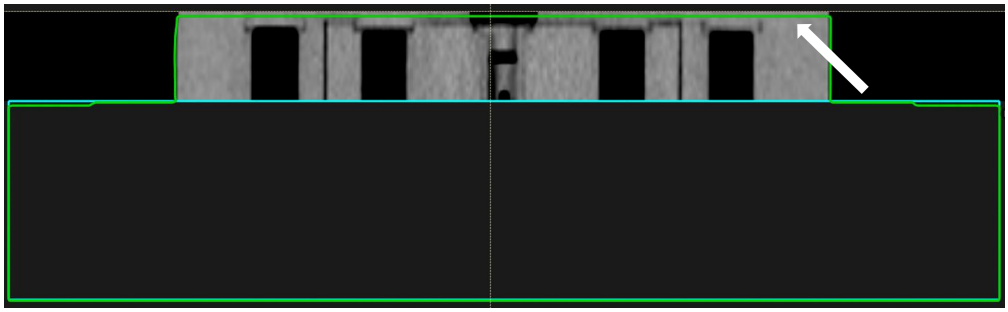

Figure 5.7.: Lateral view of the phantom including the water structure and the extended external ROI after deleting the first slice of the external contour. Note that the extended external ROI fits within the image stack as indicated by the white arrow.

The plans were developed following the general procedure described in section 5.2.2 with some modifications. Initially, the desired calibration curve was selected. After modeling the phantom and adding the water structure and external ROI, which remained consistent for all plans, the dose grid was configured. A prescription of a median dose (D50%) of 2 Gy to the selected ROI was chosen. The beam was defined by selecting the isocenter at the center of the desired ROI, and the machine and phantom angles were set to 90° and 270°, respectively, to achieve a frontal irradiation of the ROI.

The plan optimization was performed using the Pencil Beam Scanning technique, which delivered a set of beams with varying energies and weighting factors to cover the entire volume. To select the appropriate energy for the monoenergetic beam, a test was conducted. All spots except one were deleted, and the final dose was calculated using the RayStation Monte Carlo algorithm for the following energies: 62.4 MeV, 72.4 MeV, 81.3 MeV, and 97.4 MeV. This was done using the MA/Adult Head calibration curve for

the Muscle ROI. The plans were then exported and imported into FLUKA as described in previous sections. The energy E = 62.4 MeV was chosen for planning and simulations since the low energy allowed most of the interaction to take place inside the phantom rather than in the water structure, as would be the case at higher energies. A number of particles equal to 1000×10^6 was used, corresponding to a maximum dose of 2 Gy in the volume and 0.45 Gy to 50% of the volume. It should be noted that this does not correspond to the prescribed dose, which was 2 Gy to 50% of the volume, as the additional energy layers provided by the optimization process have been removed in order to achieve a monoenergetic beam. The Dose-Volume-Histogram (DVH) for the described plan is shown in Figure 5.8. For each calibration curve, the muscle plan was configured and optimized as previously described. Subsequently, the following plans were created by shifting the isocenter to the corresponding ROI and selecting the dose grid, with the optimization process not being repeated. Instead, only the final dose calculations were performed, maintaining the same energy and number of particles. It is worth noting that although the phantom has two inserts of each tissue-equivalent material, due to time constraints, only one plan, and thus only one set of simulations, was performed for each tissue-equivalent material.

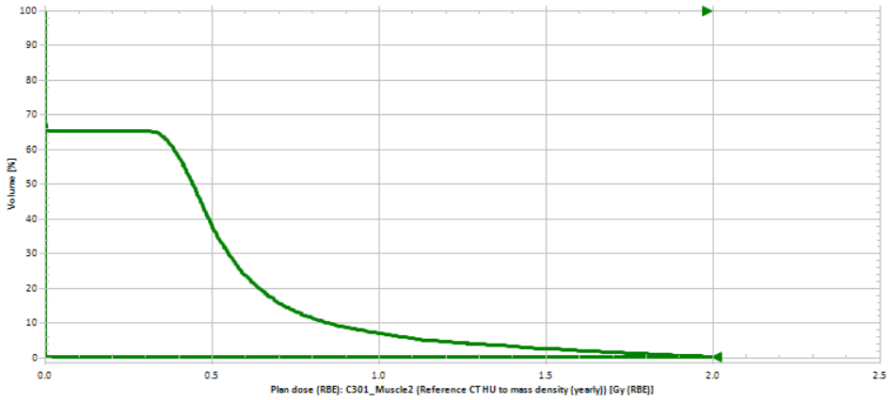

Figure 5.8.: Dose-Volume-Histogram of the muscle ROI for a 62.4 MeV proton beam with a number of particles equal to 1000×10^6. The line above the x-axis border represents the External ROI.

Each plan was exported from TPS and imported into FLUKA following the procedure described in section 5.2.3. Prior to the conversion of the CT images into the FLUKA combinatorial geometry, the first slice was removed to compensate for the delineation of the external ROI within the image stack that was performed in the TPS. The nominal energy was corrected to account for the missing beam model and nozzle by setting it to 58.98 MeV (see Table 5.3). Simulations were performed with 100,000 primaries over 5 cycles and scored in 506mm × 506mm × 158mm volume. The dose was integrated from the whole scored field in x-y plane and plotted with resolution of 1 mm along the z-axis and normalized by multiplying the dose by the number of particles. Since the physical dose and not the biological dose was exported from TPS, it was not necessary

to multiply the dose by the Relative Biological Effectiveness factor $RBE = 1.1$. Finally, the normalized dose was divided by the maximum dose to display the relative dose. The plotted distributions were then compared to the dose distributions exported from the TPS. The results can be found in Chapter 6.2.

5.4. Beam Model Influence

A beam model file prepared by the project coordinator was used to assign the effect of the beam model implementation on the range and overall shape of the Bragg curve. The beam model file includes details such as nominal beam energy, angular dispersion on the horizontal and vertical planes, and spatial beam spread as the Full Width at Half Maximum (FWHM). In addition to the beam model file, the adaptation of the nozzle to the FLUKA combinatorial geometry was necessary to obtain the expected results. The beam model verification process was performed as described above.

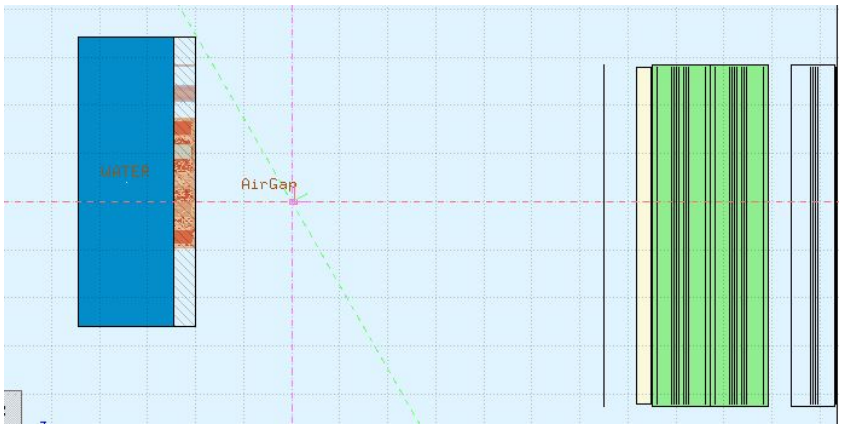

Figure 5.9.: FLUKA combinatorial geometry of the phantom, including the water structure and the nozzle.

The plan used as a basis was the muscle plan of the MA/Pediatric Head, which was already used for validation of the calibration curve of the MA/Pediatric Head. The configuration of the FLUKA input file was carried out as described in the other sections, with the exception that the beam model was added to the simulation in the RTPLAN panel of the Particle Therapy Tool. To include the nozzle geometry, the input file prepared by the project coordinator was merged into the muscle plan input file. This input file contained the geometry cards that defined the structures that compose the nozzle. Figure 5.9 illustrates the phantom including the nozzle. Since the simulation included the nozzle and beam model, it was not necessary to manually override the beam energy as in previous simulations. The run consisted of 100,000 primaries over 5 cycles. The results were plotted, normalized, and compared to the depth dose distributions from the TPS as well as to the one obtained by manually adjusting the energy. The results can be found in Section 6.3. In addition, the input file used for this simulation can be found in Appendix A.4.

6. Results

6.1. Calibration Curve Adaptation

For the interpolation of the MA/Adult Head calibration curve, the materials were divided into several ranges as suggested by Schneider [91], as shown in Fig 6.1.

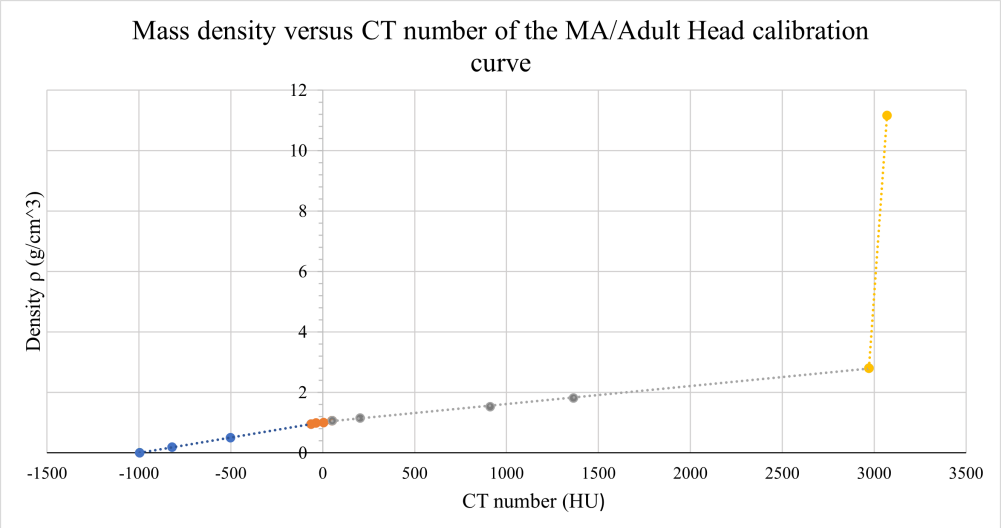

Figure 6.1.: Mass density versus CT number for the MA/Adult Head Calibration Curve. The plot shows the data separated into different regions. The blue markers correspond to lung tissue, the orange markers correspond to soft tissue, the gray markers correspond to skeletal tissue, and the yellow markers correspond to the CT maximum. In addition, the linear interpolation functions are displayed.

The interpolation functions used to fit the soft tissues are obtained by taking the data from adipose, breast, water, liver, and muscle equivalent tissues with HU in the range of -63.52 HU to 51.31 HU, and obtaining the linear regression equation given in 6.1.

$$\rho_{\text{Soft tissue}} = 0.0009 \times \text{HU} + 1.0163 \tag{6.1}$$

The data points from Bone200, Bone800 and Bone1250 with CT numbers ranging from 204.3 HU to 1364.4 HU are used to calculate the linear regression equation, which is given by (6.2)

$$\rho_{\text{Skeletal tissue}} = 0.0006 \times \text{HU} + 1.0133 \tag{6.2}$$

For the lung and the CT maximum ranges, only two points were available for use. In the case of the lung tissue, the data points corresponding to LungEx and LungIn with Hounsfield units of -820.69 HU and -502.75 HU give the following linear regression:

$$\rho_{\text{Lung}} = 0.001 \times \text{HU} + 1.0081 \tag{6.3}$$

The data points of the aluminum and CT maximum were taken to define the upper limit, resulting equation (6.4).

$$\rho_{\text{Max}} = 0.0853 \times \text{HU} - 250.82 \tag{6.4}$$

The lower limit, corresponding to air, was set as a constant at $\rho = 0.001214\,\text{g/cm}^3$. The density was calculated using the respective linear regression equations. is compared to the actual density of the materials in Table 6.1. The absolute and relative deviation between the physical and calculated values are also included in the table.

Material	**Density (g/cm^3)**	**Calculated Density (g/cm^3)**	**Deviation (g/cm^3)**	**Deviation (%)**
Air	1.21×10^{-3}	1.21×10^{-3}	0.00	0.00
LungIn	0.195	0.187	7.59×10^{-3}	3.89
LungEx	0.510	0.505	4.64×10^{-3}	0.91
Adipose	0.960	0.959	8.65×10^{-4}	0.090
Breast	0.991	0.983	8.23×10^{-3}	0.83
Water	1.00	1.02	-2.03×10^{-2}	2.03
Liver	1.07	1.06	1.19×10^{-2}	1.11
Muscle	1.0620	1.0625	-4.78×10^{-4}	0.04
Bone200	1.16	1.14	2.51×10^{-2}	2.16
Bone800	1.53	1.56	-2.97×10^{-2}	1.94
Bone1250	1.82	1.83	-1.19×10^{-2}	0.65
Al	2.80	2.79	3.50×10^{-3}	0.12
CT MAX	11.163	11.051	0.112	1.00

Table 6.1.: MA/Adult Head calibration curve materials and their physical densities compared to the densities calculated for the same materials using the respective linear regression equations.

The linear regression equations for the ranges of lung, soft tissue, skeletal, and CT maximum were used to calculate the density of the maximum and minimum CT numbers for each HU material determined in FLUKA. By employing these values, correction factors between the two curves were determined according to the process outlined in Section 5.2.1 using Equation 5.7. The resulting correction factors were organized in the appropriate material file format, located in Appendix A.2, and incorporated into FLUKA as detailed in Chapter 5.2.2 to simulate the Bragg curve of a 97.4 MeV proton beam in the materials of the phantom of known densities depicted in Figure 5.2. Additionally, for comparison purposes, a material file provided by the FLUKA developers and based on

the work of Schneider, referred to as the Schneider calibration curve in this study, was also utilized for the simulations in each material. The Bragg curve of the proton beam in acrylic was directly exported from TPS and compared to the FLUKA simulations using the MA/Adult Head calibration curve and the Schneider calibration curve, as shown in Figure 6.2.

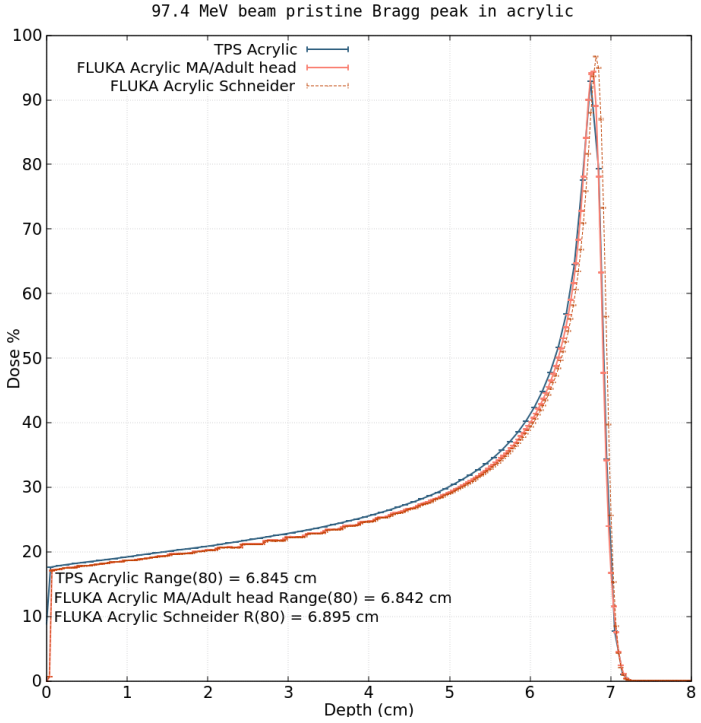

Figure 6.2.: Bragg curve of a 97.4 MeV proton beam in acrylic, indicating its range at 80% of the maximum dose. The blue curve represents the dose distribution calculated in the TPS and contained in the RTDOSE module of the DICOM file. Additionally, the solid and scattered orange lines depict the depth dose distribution of the beam in acrylic using the MA/Adult Head and the Schneider calibration curve as a basis for the voxel geometry.

Material	**Curve**	**Range (cm)**
Acrylic	TPS Adult Head	6.85 ± 0.05
	FLUKA MA/Adult Head	6.84 ± 0.05
	Schneider	6.90 ± 0.05
Difference TPS/MA		0.01 ± 0.07
Difference TPS/Schneider		0.05 ± 0.07

Table 6.2.: Ranges and range differences for acrylic from the TPS and FLUKA curves.

The error in the ranges is derived from the resolution of the dose grid, while the error in the difference is calculated using error propagation. Additionally, the difference between the two curves is always given as an absolute value. Table 6.2 lists the ranges at 80% of the maximum dose for each of the three curves, as well as the difference in range between the range of the TPS curve and the range of the two curves simulated with FLUKA. Figure 6.3 shows the Bragg curves for the 97.4 MeV proton beam in nylon for the TPS, MA/Adult Head and Schneider calibration curves, while Table 6.3 lists the ranges of these curves.

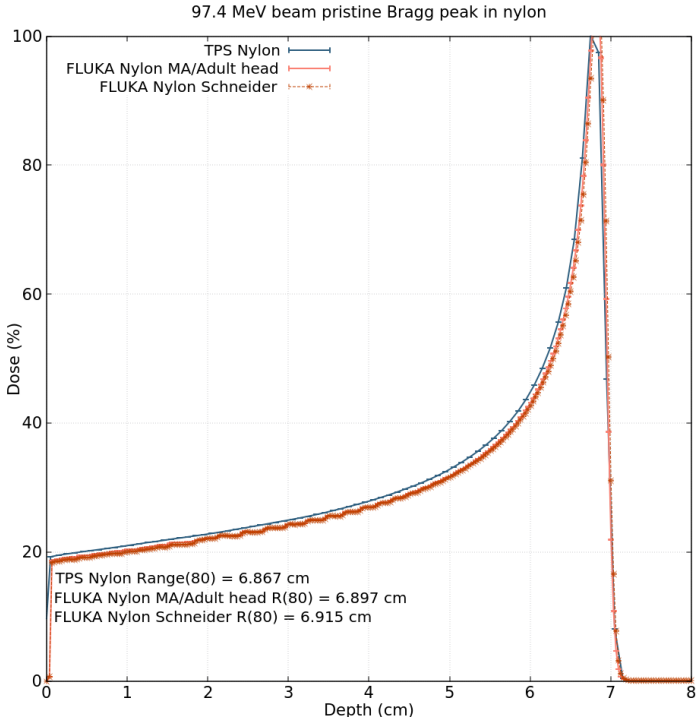

Figure 6.3.: Bragg curve of a 97.4 MeV proton beam in nylon, showing its 80% range of the maximum dose. The blue curve represents the TPS dose distribution. In addition, the solid and scattered orange lines show the MA/Adult Head and the Schneider depth dose distribution of the beam, respectively.

Material	**Curve**	**Range (cm)**
Nylon	TPS Adult Head	6.87 ± 0.05
	FLUKA MA/Adult Head	6.90 ± 0.05
	Schneider	6.92 ± 0.05
Difference TPS/MA		0.03 ± 0.07
Difference TPS/Schneider		0.05 ± 0.07

Table 6.3.: Ranges and range differences for nylon from the TPS and FLUKA curves.

The Bragg curves for the 97.4 MeV proton beam in Lexan are depicted in Figure 6.4. Table 6.4 summarizes the 80% range values for the Lexan material for the TPS Adult Head, FLUKA MA/Adult Head, and FLUKA Schneider calibration curves.

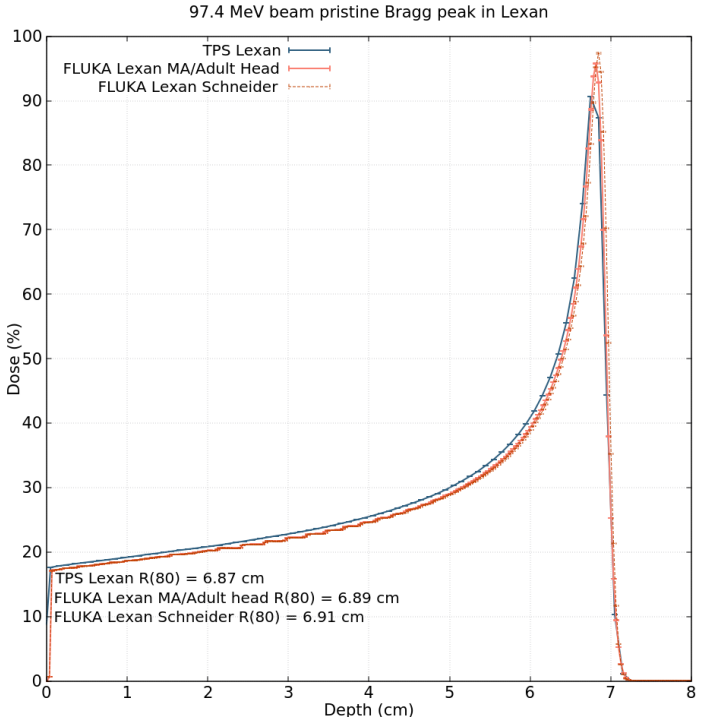

Figure 6.4.: Bragg curve of a 97.4 MeV proton beam in Lexan, displaying its range at 80% of the maximum dose. The blue curve represents the dose distribution calculated in the TPS, while the solid and scattered orange lines show the depth dose distribution using the MA/Adult Head and the Schneider calibration curve.

Material	**Curve**	**Range (cm)**
Lexan	TPS Adult Head	6.87 ± 0.05
	FLUKA MA/Adult Head	6.89 ± 0.05
	Schneider	6.91 ± 0.05
Difference TPS/MA		0.02 ± 0.07
Difference TPS/Schneider		0.04 ± 0.07

Table 6.4.: Ranges and range differences for Lexan from the TPS and FLUKA curves.

The range of the Bragg peak in Teflon for the TPS, MA/Adult Head and Schneider calibration curves as well as their differences are given in Table 6.5. Graph 6.5 displays two distinct peaks. The smaller peak can be attributed to the fact that the beam was

not centered on the target material when the plan was edited, as detailed in Section 5.2.2. This resulted in a portion of the beam being deposited on the surrounding water-equivalent material, as depicted in Figure 6.6. The left image shows the dose distribution, with contour lines representing different dose levels, while the right image highlights the location of the maximum dose within the target area, displaying the misalignment of the beam.

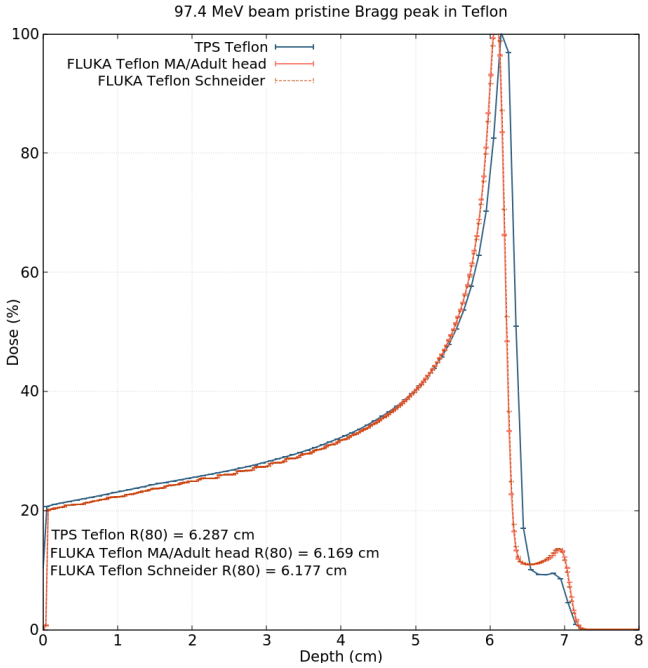

Figure 6.5.: Bragg curve in Teflon with the TPS curve in blue and the FLUKA MA/Adult Head and the Schneider calibration curves in orange.

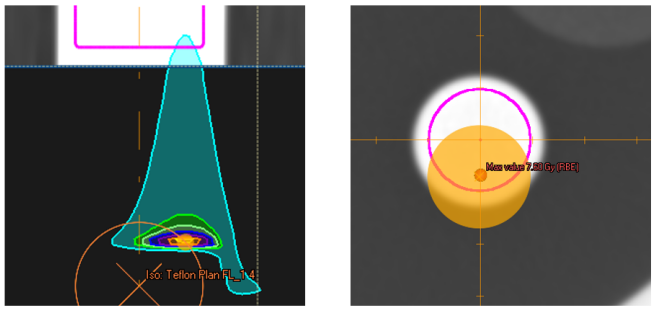

Figure 6.6.: Dose distribution (left) and single spot (right) of the 97.4 MeV monoenergetic proton beam for the Teflon plan.

Material	Curve	Range (cm)
Teflon	TPS Adult Head	6.29 ± 0.05
	FLUKA MA/Adult Head	6.17 ± 0.05
	FLUKA Schneider	6.18 ± 0.05
Difference TPS/MA		0.12 ± 0.07
Difference TPS/Schneider		0.11 ± 0.07

Table 6.5.: Ranges and range differences for Teflon from the TPS and FLUKA curves.

Finally, the Bragg curves for the 97.4 MeV proton beam in polyethylene for the TPS, MA/Adult Head and Schneider calibration curves are depicted in Figure 6.7. Table 6.6 summarizes the ranges.

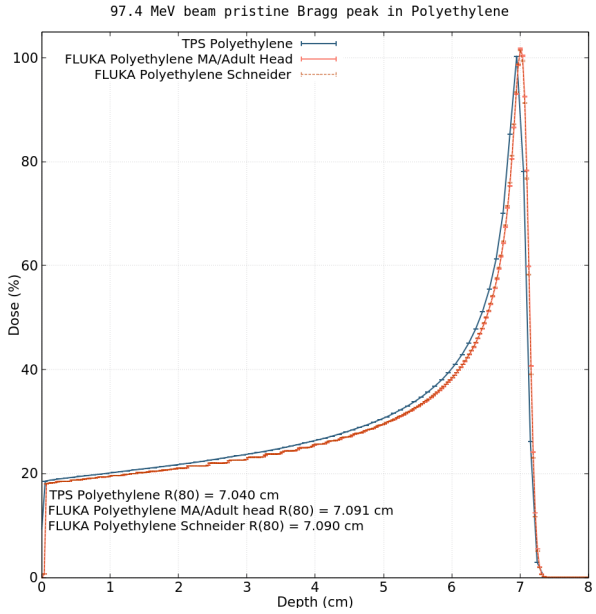

Figure 6.7.: Bragg curve of proton beam in polyethylene. The TPS curve is given in blue, while the solid and scattered orange correspond to the MA/Adult Head and Schneider curves.

Material	Curve	Range (cm)
Polyethylene	TPS Adult Head	7.04 ± 0.05
	FLUKA MA/Adult Head	7.09 ± 0.05
	FLUKA Schneider	7.09 ± 0.05
Difference TPS/MA		0.05 ± 0.07
Difference TPS/Schneider		0.05 ± 0.07

Table 6.6.: Ranges and range differences for polyethylene from the TPS and FLUKA curves.

6.2. Calibration Curve Comparison

6.2.1. Adult Head

The Bragg peaks for the materials in the tissue-equivalent phantom were calculated with TPS and simulated in FLUKA using the material file previously prepared and implemented for the range calculations of the phantom with material inputs of known density. A comparison between the range from FLUKA and TPS is shown in the following plots, where the TPS curve is displayed in purple and the FLUKA MA/Adult Head curve is displayed in green.

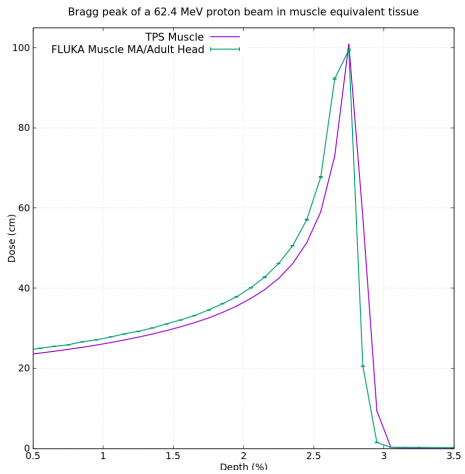

Figure 6.8.: Bragg curve of 62.4 MeV proton beam in muscle equivalent material obtained for the calibration curve MA/Adult Head.

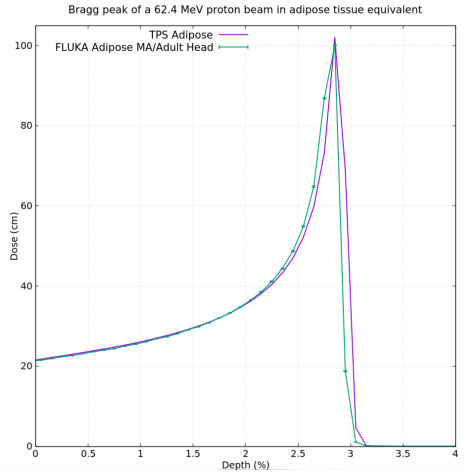

Figure 6.9.: Bragg curve of 62.4 MeV proton beam in adipose tissue-equivalent for the calibration curve MA/Adult Head.

The Bragg peaks for the muscle and adipose tissue equivalent materials shown in Figures 6.8 and 6.9. The ranges at 80% of the maximum dose for these materials are given in Table 6.7.

Material	Curve	Range (cm)
Muscle	TPS Adult Head	2.79 ± 0.05
	FLUKA Adult Head	2.77 ± 0.05
	Difference	0.02 ± 0.07
Adipose	TPS Adult Head	2.92 ± 0.05
	FLUKA Adult Head	2.87 ± 0.05
	Difference	0.05 ± 0.07

Table 6.7.: Ranges and range differences for the muscle and adipose equivalent materials from the TPS and MA/Adult Head calibration curves.

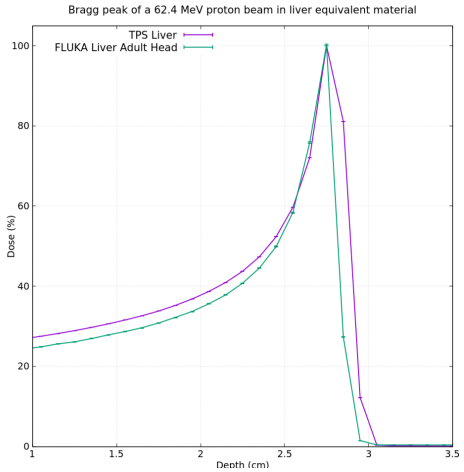

Figure 6.10.: Bragg curve of 62.4 MeV proton beam in liver equivalent material for the calibration curve MA/Adult Head.

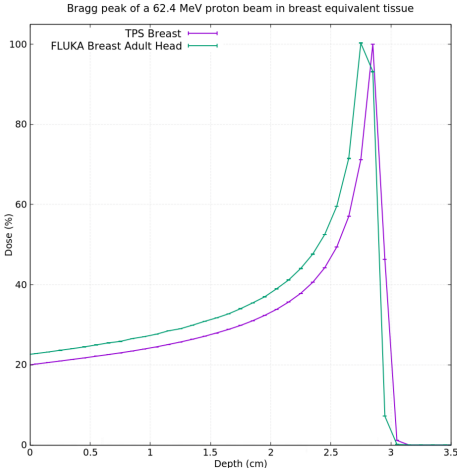

Figure 6.11.: Bragg curve of 62.4 MeV proton beam in breast equivalent material for the calibration curve MA/Adult Head.

The ranges at 80% of the maximum dose for the liver and breast equivalent materials (Figures 6.10 and 6.11) are given in Table 6.8, Furthermore, the ranges for the LungIn and LungEx materials (Figures 6.12 and 6.13) are given in Table 6.9.

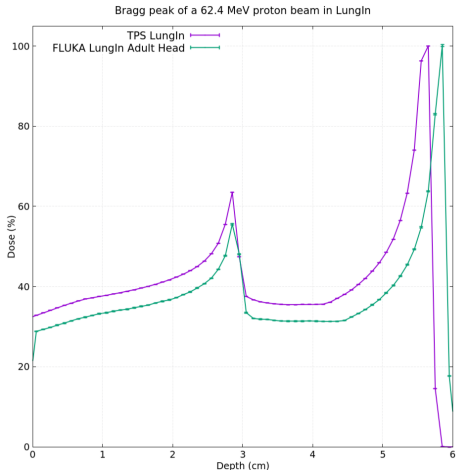

Figure 6.12.: Bragg curve of 62.4 MeV proton beam in inhaling lung equivalent material (LungIn) for the calibration curve MA/Adult Head.

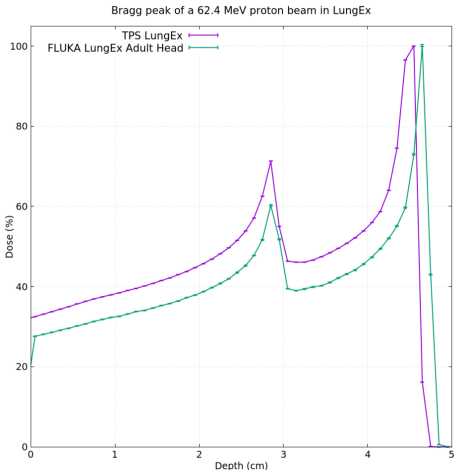

Figure 6.13.: Bragg curve of 62.4 MeV proton beam in exhaling lung equivalent material (LungEx) for the calibration curve MA/Adult Head.

Material	Curve	Range (cm)
Liver	TPS Adult Head	2.85 ± 0.05
	FLUKA Adult Head	2.87 ± 0.05
	Difference	0.02 ± 0.07
Breast	TPS Adult Head	2.88 ± 0.05
	FLUKA Adult Head	2.96 ± 0.05
	Difference	0.08 ± 0.07

Table 6.8.: Ranges and range differences for the liver and breast equivalent materials from the TPS and MA/Adult Head calibration curves.

Material	Curve	Range (cm)
LungEx	TPS Adult Head	4.57 ± 0.05
	MA/Adult Head	4.68 ± 0.05
	Difference	0.11 ± 0.07
LungIn	TPS Adult Head	5.67 ± 0.05
	MA/Adult Head	5.87 ± 0.05
	Difference	0.2 ± 0.07

Table 6.9.: Ranges and range differences for the LungEx and LungIn equivalent materials from the TPS and MA/Adult Head calibration curves.

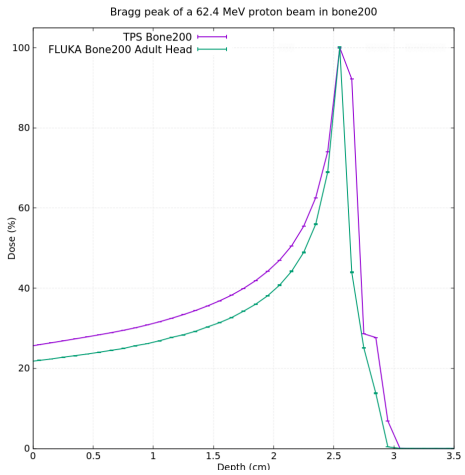

Figure 6.14.: Bragg curve of 62.4 MeV proton beam in Bone200 obtained for the calibration curve MA/Adult Head.

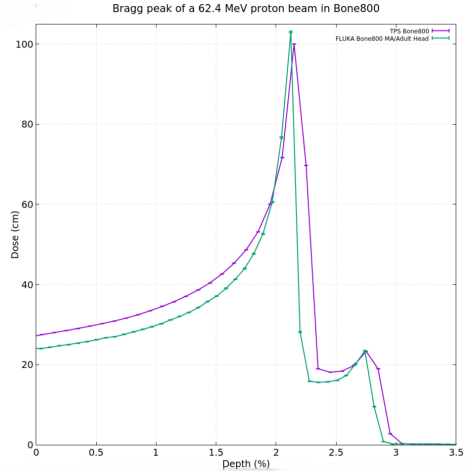

Figure 6.15.: Bragg curve of 62.4 MeV proton beam in Bone800 obtained for the calibration curve MA/Adult Head.

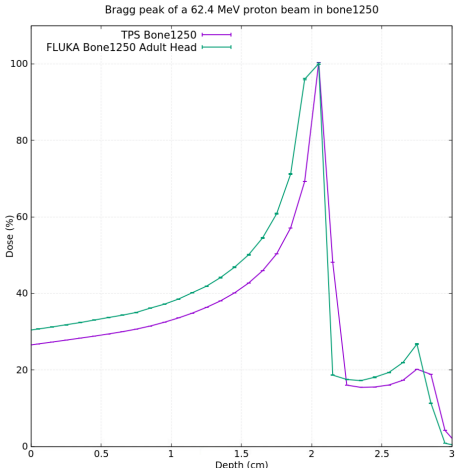

Figure 6.16.: Bragg curve for a 62.4 MeV proton beam in Bone1250 material, obtained for the calibration curve MA/Adult Head.

Finally, the ranges for the Bone200, Bone800 and Bone1250 materials (Figures 6.14 and 6.15 and 6.16) are given in Table 6.10.

Material	**Curve**	**Range (cm)**
Bone200	TPS Adult Head	2.67 ± 0.05
	FLUKA Adult Head	2.58 ± 0.05
	Difference	0.09 ± 0.07
Bone800	TPS Adult Head	2.21 ± 0.05
	MA/Adult Head	2.15 ± 0.05
	Difference	0.06 ± 0.07
Bone1250	TPS Adult Head	2.07 ± 0.05
	FLUKA Adult Head	2.08 ± 0.05
	Difference	0.01 ± 0.07

Table 6.10.: Ranges and range differences for the Bone200, Bone800, and Bone1250 materials from the TPS and MA/Adult Head curves.

In this and the following sections, the error in the ranges is also derived from the resolution of the dose grid, while the error in the difference is calculated using error propagation. In addition, the difference between the two sets of curves is given as an absolute value.

6.2.2. Pediatric Head

The adaptation of the MA/Pediatric Head calibration curve was performed following the same procedure as described above in Section 6.1. The linear regression equation for the lung tissue is:

$$\rho_{\text{Lung}} = 0.001 \times \text{HU} + 1.0217 \tag{6.5}$$

For the soft tissue, the linear regression equation of the MA/Pediatric Head calibration curve is given by:

$$\rho_{\text{Soft tissue}} = 0.0009 \times \text{HU} + 1.0159 \tag{6.6}$$

The linear regression equation for skeletal tissue is given by:

$$\rho_{\text{Skeletal tissue}} = 0.0006 \times \text{HU} + 1.0131 \tag{6.7}$$

Finally, for the CT maximum of the MA/Pediatric Head calibration curve, which has a density $\rho = 7.6519\,\text{g/cm}^3$, the linear regression equation given by:

$$\rho_{\text{Max}} = 0.0495 \times \text{HU} - 144.34 \tag{6.8}$$

The material densities calculated using these equations are compared to the densities measured for the tissue-equivalent materials in Table 6.11.

Material	**Density (g/cm^3)**	**Calculated Density (g/cm^3)**	**Deviation (g/cm^3)**	**Deviation (%)**
Air	1.21×10^{-3}	1.21×10^{-3}	0	0
LungIn	0.195	0.201	-5.53×10^{-3}	2.83
LungEx	0.510	0.519	-8.66×10^{-3}	1.69
Adipose	0.960	0.959	5.42×10^{-4}	0.06
Breast	0.991	0.983	8.11×10^{-3}	0.82
Water	1.000	1.020	-1.95×10^{-2}	1.95
Liver	1.072	1.061	1.12×10^{-2}	1.04
Muscle	1.062	1.062	-5.76×10^{-5}	0.05
Bone200	1.161	1.136	2.52×10^{-2}	2.17
Bone800	1.530	1.560	-2.97×10^{-2}	1.94
Bone1250	1.820	1.832	-1.24×10^{-2}	0.68
Al	2.800	2.796	3.70×10^{-3}	0.13
CT MAX	7.652	7.625	2.69×10^{-2}	0.35

Table 6.11.: MA/Pediatric Head calibration curve materials and their physical densities compared to the densities calculated for the same materials using the respective linear regression equations.

Based on these results, the material file for the MA/Pediatric Head was created as described above. The Bragg peaks for the materials in the tissue-equivalent phantom were calculated using TPS and simulated in FLUKA. The comparison between the FLUKA

and TPS depth dose distributions for each material is shown in the following plots, where the TPS curve is in purple and the FLUKA MA/Pediatric Head curve is in green.

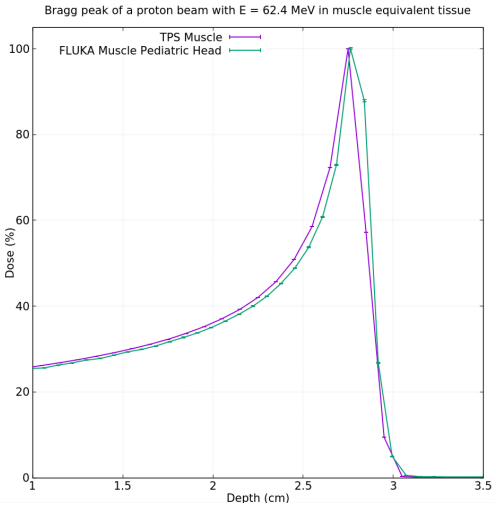

Figure 6.17.: Bragg curve of 62.4 MeV proton beam in muscle equivalent material obtained for the calibration curve MA/Pediatric Head.

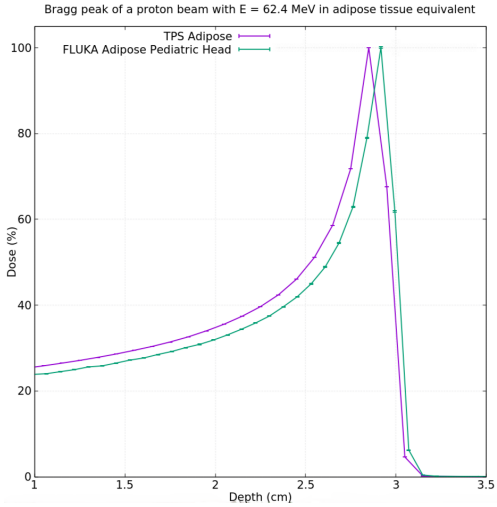

Figure 6.18.: Bragg curve of 62.4 MeV proton beam in adipose tissue material obtained for the calibration curve MA/Pediatric Head.

The ranges and range differences for the materials in the soft tissue category (muscle 6.17, adipose tissue 6.18, liver 6.19 and breast 6.20) are given in Table 6.12.

Material	**Curve**	**Range (cm)**
Muscle	TPS Pediatric Head	2.79 ± 0.05
	MA/Pediatric Head	2.84 ± 0.05
	Difference	0.05 ± 0.07
Adipose	TPS Pediatric Head	2.91 ± 0.05
	MA/Pediatric Head	2.95 ± 0.05
	Difference	0.04 ± 0.07
Liver	TPS Pediatric Head	2.84 ± 0.05
	MA/Pediatric Head	2.86 ± 0.05
	Difference	0.02 ± 0.07
Breast	TPS Pediatric Head	2.88 ± 0.05
	MA/Pediatric Head	2.94 ± 0.05
	Difference	0.06 ± 0.07

Table 6.12.: Ranges and range differences for soft tissue category materials from the TPS and MA/Pediatric Head curves.

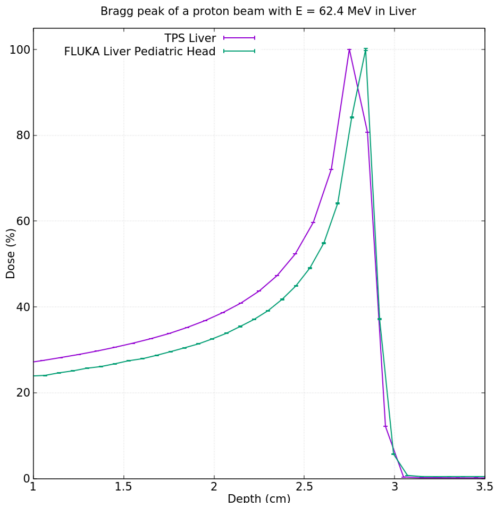

Figure 6.19.: Bragg curve of 62.4 MeV proton beam in liver equivalent material obtained for the calibration curve MA/Pediatric Head.

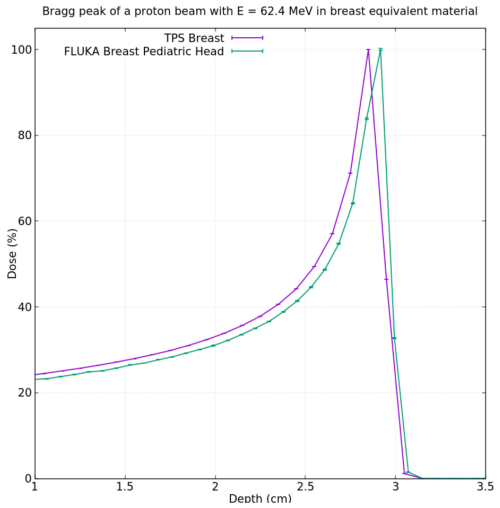

Figure 6.20.: Bragg curve of 62.4 MeV proton beam in breast equivalent material obtained for the calibration curve MA/Pediatric Head.

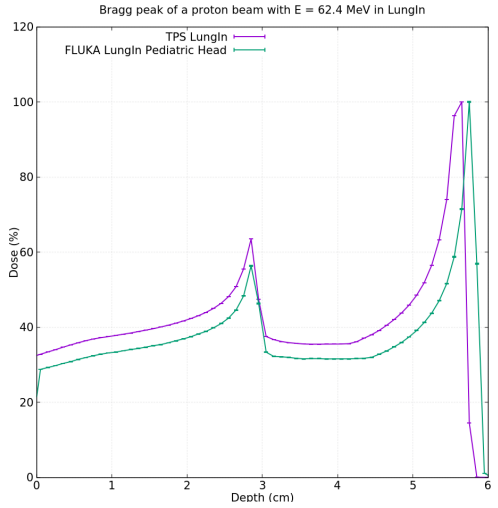

Figure 6.21.: Bragg curve of 62.4 MeV proton beam in inhaling lung equivalent material (LungIn) obtained for the calibration curve MA/Pediatric Head.

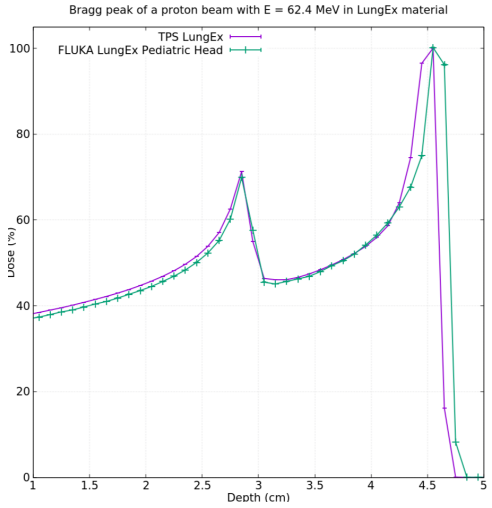

Figure 6.22.: Bragg curve of 62.4 MeV proton beam in exhaling lung equivalent material (LungEx) obtained for the calibration curve MA/Pediatric Head.

For the LungEx and LungIn materials, displayed in Figures 6.22 and 6.21, the ranges

at 80% of the maximum dose are given in Table 6.13.

Material	Curve	Range (cm)
LungEx	TPS Pediatric Head	4.56 ± 0.05
	MA/Pediatric Head	4.66 ± 0.05
	Difference	0.10 ± 0.07
LungIn	TPS Pediatric Head	5.66 ± 0.05
	MA/Pediatric Head	5.80 ± 0.05
	Difference	0.14 ± 0.07

Table 6.13.: Ranges and range differences for the LungEx and LungIn materials from the TPS and MA/Pediatric Head curves.

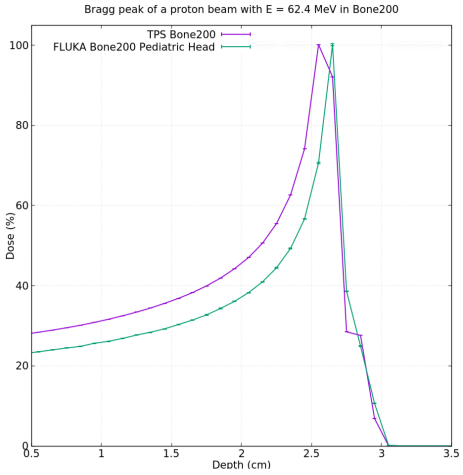

Figure 6.23.: Bragg curve of 62.4 MeV proton beam in Bone200, obtained for the calibration curve MA/Pediatric Head.

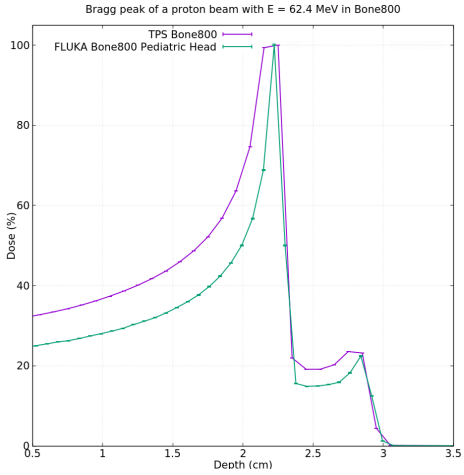

Figure 6.24.: Bragg curve of 62.4 MeV proton beam in Bone800, obtained for the calibration curve MA/Pediatric Head.

Material	Curve	Range (cm)
Bone200	TPS Pediatric Head	2.66 ± 0.05
	MA/Pediatric Head	2.58 ± 0.05
	Difference	0.08 ± 0.07
Bone800	TPS Pd Head	2.27 ± 0.05
	MA/Pd Head	2.25 ± 0.05
	Difference	0.02 ± 0.07

Table 6.14.: Ranges and range differences for the Bone200 and Bone800 materials from the TPS and MA/Pediatric Head curves.

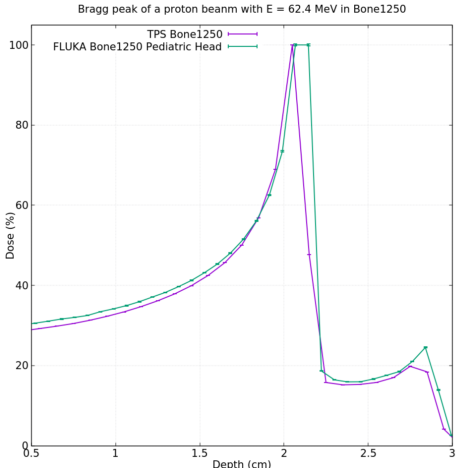

Figure 6.25.: Bragg curve for a 62.4 MeV proton beam in Bone1250 material, obtained for the calibration curve MA/Pediatric Head.

The ranges and range differences for the Bone200 and Bone800 materials, shown in Figures 6.23 and 6.24 are listed in Table 6.14, while for Bone1250, shown in Figure 6.25, are in Table 6.15.

Material	**Curve**	**Range (cm)**
Bone1250	TPS Pediatric Head	2.08 ± 0.05
	MA/Pediatric Head	2.16 ± 0.05
	Difference	0.08 ± 0.07

Table 6.15.: Ranges and range differences for Bone1250 from the TPS and MA/Pediatric Head curves.

6.2.3. Pediatric Abdomen

Finally, the adaptation of the last evaluated calibration curve, the MA/Pediatric Abdomen calibration curve, was also completed following the procedure described in Section 6.1. For the soft tissues, the linear regression was obtained by taking the data points corresponding to adipose, breast, liver, and muscle equivalent materials with CT numbers ranging from -65.24 HU to 41.79 HU, with water having a CT number equal to -4.64 HU. The resulting linear regression equation is:

$$\rho_{\text{ Soft tissue}} = 0.001 \times \text{HU} + 1.0233 \tag{6.9}$$

For the case of the lung equivalent tissue, the linear regression equation is:

$$\rho_{\text{ Lung}} = 0.001 \times \text{HU} + 1.0264 \tag{6.10}$$

In the case of the skeletal tissue, the CT numbers for the MA/Pediatric Abdomen calibration curve range from 220.17 HU up to 1286.55 HU, resulting in the following equation:

$$\rho_{\text{ Skeletal tissue}} = 0.0006 \times \text{HU} + 1.0288 \tag{6.11}$$

Finally, for the CT maximum of the MA/Pediatric Abdomen calibration curve is the same as the CT maximum of the MA/Pediatric Head presented in Equation 6.8, since both have a maximum with a density $\rho = 7.6519\,\text{g/cm}^3$,

$$\rho_{\text{ Max}} = 0.0495 \times \text{HU} - 144.34 \tag{6.12}$$

Table 6.16 lists the physical densities together with the resulting densities calculated using the respective equations and shows their absolute and relative deviation.

Material	**Density (g/cm^3)**	**Calculated Density (g/cm^3)**	**Deviation (g/cm^3)**	**Deviation (%)**
Air	1.21×10^{-3}	1.21×10^{-3}	0	0
LungIn	0.195	0.211	-1.60×10^{-2}	8.20
LungEx	0.510	0.520	-9.90×10^{-3}	1.94
Adipose	0.960	0.958	1.94×10^{-3}	0.20
Breast	0.991	0.981	9.87×10^{-3}	1.00
Water	1.000	1.019	-1.87×10^{-2}	1.87
Liver	1.072	1.062	1.05×10^{-2}	0.98
Muscle	1.062	1.065	-3.10×10^{-3}	0.29
Bone200	1.161	1.161	9.65×10^{-5}	0.05
Bone800	1.530	1.551	-2.12×10^{-2}	1.38
Bone1250	1.820	1.801	1.93×10^{-2}	1.06
Al	2.800	2.812	-1.20×10^{-2}	0.43
CT MAX	7.652	7.625	2.69×10^{-2}	0.35

Table 6.16.: MA/Pediatric Abdomen calibration curve materials and their calculated and physical densities.

The comparison of depth dose distributions between the TPS and FLUKA calculations using the MA/Pediatric Abdomen calibration curve and its recalculation for each tissue-equivalent material are shown below. The TPS curve is presented in purple, while the FLUKA MA/Pediatric Abdomen curve is presented in green.

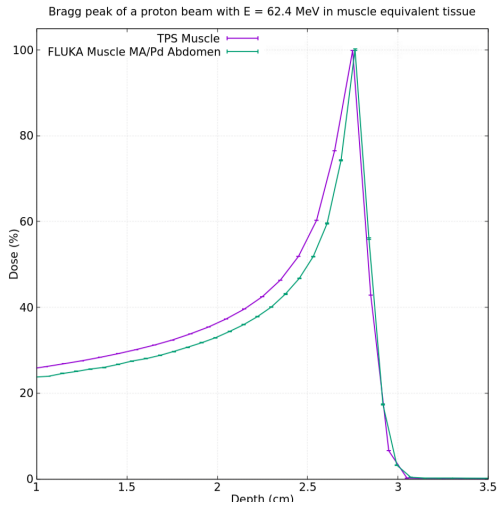

Figure 6.26.: Bragg curve for a 62.4 MeV proton beam in muscle equivalent material for MA/Pediatric Abdomen.

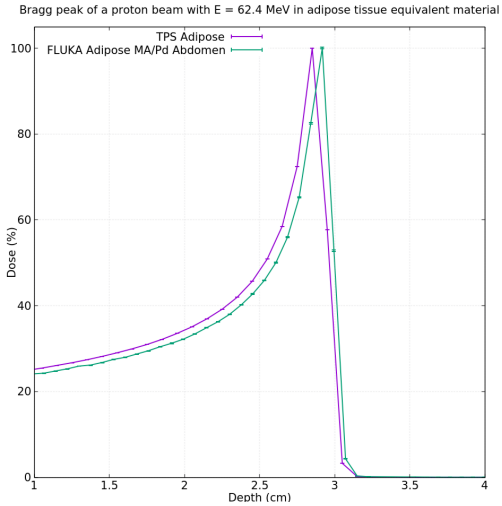

Figure 6.27.: Bragg curve for a 62.4 MeV proton beam in adipose tissue material for MA/Pediatric Abdomen.

The ranges and range differences for the materials in the soft tissue category (muscle 6.26, adipose tissue 6.27, liver 6.28 and breast 6.29) are given in Table 6.17.

Material	**Curve**	**Range (cm)**
Muscle	TPS Pediatric Abdomen	2.78 ± 0.05
	MA/Pediatric Abdomen	2.80 ± 0.05
	Difference	0.02 ± 0.07
Adipose	TPS Pediatric Abdomen	2.89 ± 0.05
	MA/Pediatric Abdomen	2.94 ± 0.05
	Difference	0.05 ± 0.07
Liver	TPS Pediatric Abdomen	2.80 ± 0.05
	MA/Pediatric Abdomen	2.84 ± 0.05
	Difference	0.04 ± 0.07
Breast	TPS Pediatric Abdomen	2.88 ± 0.05
	MA/Pediatric Abdomen	2.93 ± 0.05
	Difference	0.05 ± 0.07

Table 6.17.: Ranges and range differences for soft tissue category materials from the TPS and MA/Pediatric Abdomen curves.

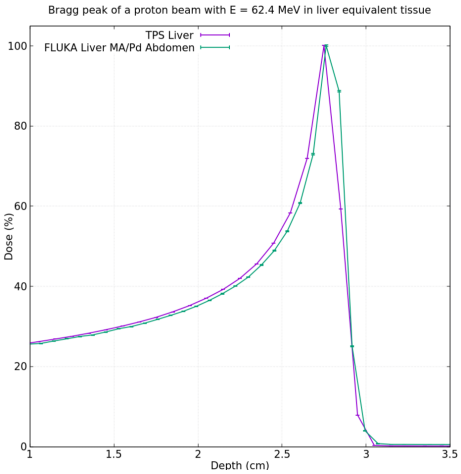

Figure 6.28.: Bragg curve for a 62.4 MeV proton beam in liver equivalent material for MA/Pediatric Abdomen.

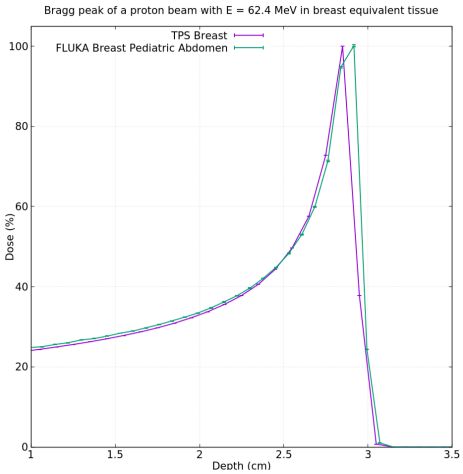

Figure 6.29.: Bragg curve for a 62.4 MeV proton beam in breast equivalent material for MA/Pediatric Abdomen.

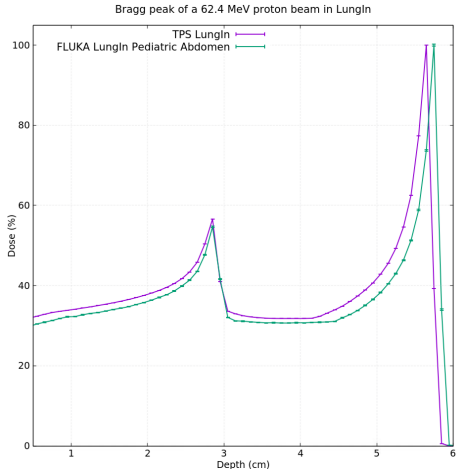

Figure 6.30.: Bragg curve of 62.4 MeV proton beam in LungIn for MA/Pediatric Abdomen.

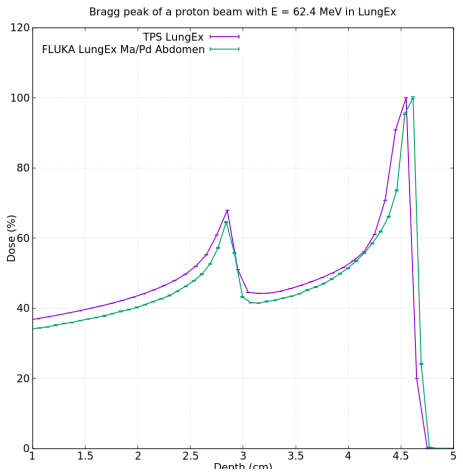

Figure 6.31.: Bragg curve of 62.4 MeV proton beam in LungEx for MA/Pediatric Abdomen.

For the LungEx and LungIn materials, displayed in Figures 6.31 and 6.30, the ranges at 80% of the maximum dose are given in Table 6.18

Material	Curve	Range (cm)
LungEx	TPS Pediatric Abdomen	4.56 ± 0.05
	MA/Pediatric Abdomen	4.63 ± 0.05
	Difference	0.07 ± 0.07
LungIn	TPS Pediatric Abdomen	5.68 ± 0.05
	MA/Pediatric Abdomen	5.78 ± 0.05
	Difference	0.10 ± 0.07

Table 6.18.: Ranges and range differences for LungEx and LungIn materials from the TPS and MA/Pediatric Abdomen curves.

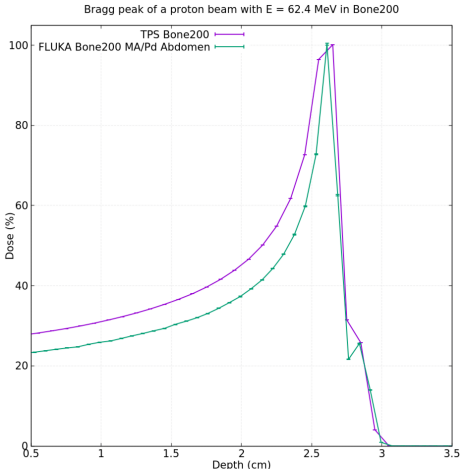

Figure 6.32.: Bragg curve for a 62.4 MeV proton beam in Bone200 material for MA/Pediatric Abdomen.

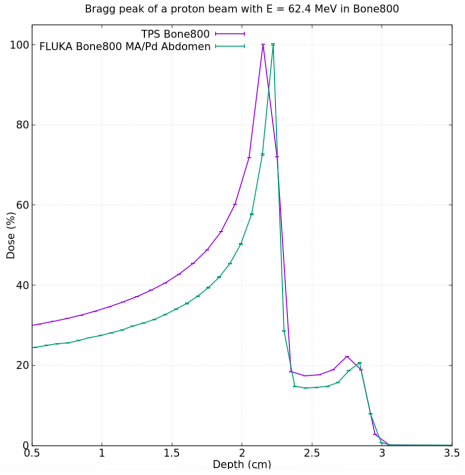

Figure 6.33.: Bragg curve for a 62.4 MeV proton beam in Bone800 material for MA/Pediatric Abdomen.

Material	Curve	Range (cm)
Bone200	TPS Pediatric Abdomen	2.68 ± 0.05
	MA/Pediatric Abdomen	2.64 ± 0.05
	Difference	0.04 ± 0.07
Bone800	TPS Pd Abdomen	2.22 ± 0.05
	MA/Pd Abdomen	2.24 ± 0.05
	Difference	0.02 ± 0.07

Table 6.19.: Ranges and range differences for the Bone200 and Bone800 materials from the TPS and MA/Pediatric Abdomen curves.

For the Bone200 and Bone800 materials, shown in Figures 6.32 and 6.33, the ranges are listed in Table 6.19, while for Bone1250 (Figure 6.34) are given in Table 6.20.

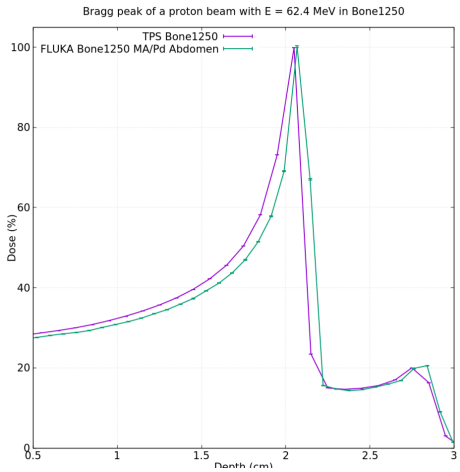

Figure 6.34.: Bragg curve for a 62.4 MeV proton beam in Bone1250 material for MA/Pediatric Abdomen.

Material	**Curve**	**Range (cm)**
Bone1250	TPS Pediatric Abdomen	2.07 ± 0.05
	MA/Pediatric Abdomen	2.12 ± 0.05
	Difference	0.05 ± 0.07

Table 6.20.: Ranges and range differences for the Bone1250 materials from the TPS and MA/Pediatric Abdomen curves.

6.2.4. Range Comparison

To facilitate visualization and comparison of the results from all three calibration curves, the ranges at 80% of the maximum dose were divided into the previously defined categories: lung, soft tissue, and skeletal tissue. These data were then plotted as a histogram with the x-axis representing the curve and the y-axis representing the range of that curve. The range of all curves for the LungEx material are displayed in 6.35 and for the LungIn material in 6.36.

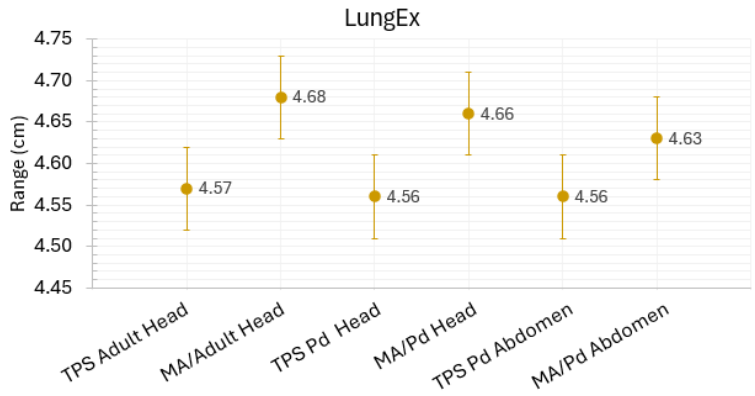

Figure 6.35.: Comparison of the ranges at 80% of the maximum dose for the LungEx material in the TPS calculation with the three calibration curves and their respective FLUKA simulations from the Bragg curves plotted above.

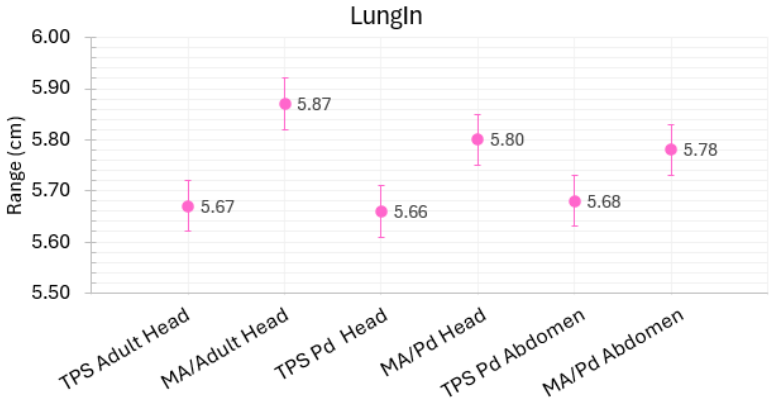

Figure 6.36.: Comparison of the ranges at 80% of the maximum dose for the LungIn material in the TPS calculation with the three calibration curves and their respective FLUKA simulations from the Bragg curves plotted above.

The ranges for the skeletal tissue are displayed in Figures 6.37, 6.38 and 6.39.

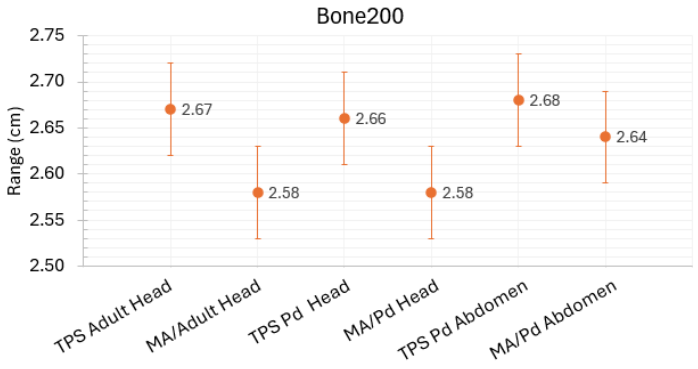

Figure 6.37.: Comparison of the ranges at 80% of the maximum dose for the Bone200 from TPS and FLUKA for the three calibration curves.

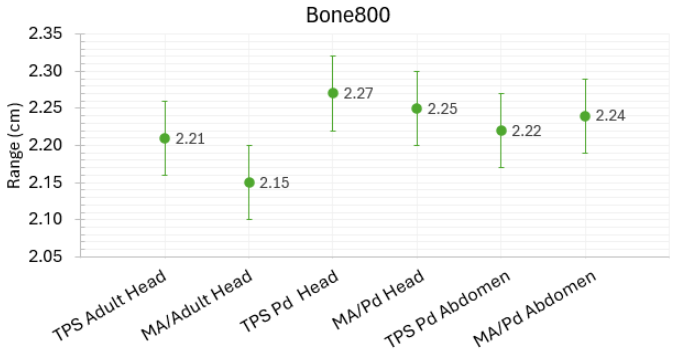

Figure 6.38.: Comparison of the ranges at 80% of the maximum dose for the Bone800 from TPS and FLUKA for the three calibration curves.

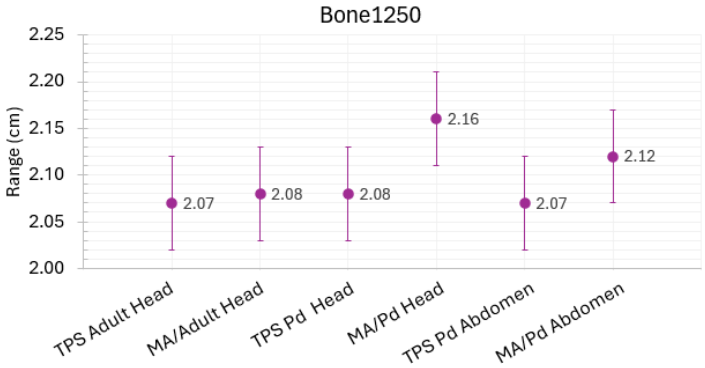

Figure 6.39.: Comparison of the ranges at 80% of the maximum dose for the Bone1250 from TPS and FLUKA for the three calibration curves.

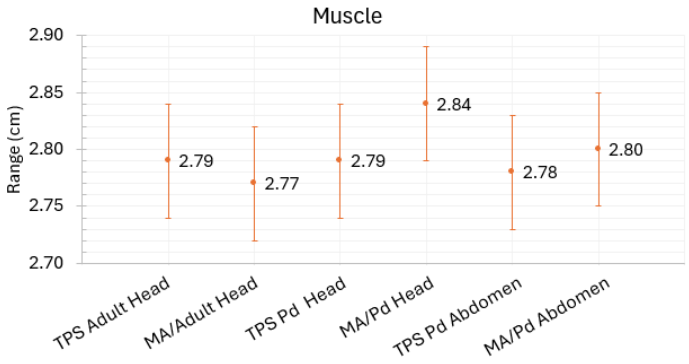

Figure 6.40.: Comparison of the ranges at 80% of the maximum dose for muscle from TPS and FLUKA for the three calibration curves.

Finally, Figures 6.40, 6.41, 6.42 and 6.43 display the ranges for the muscle, adipose tissue, liver and breast equivalent materials.

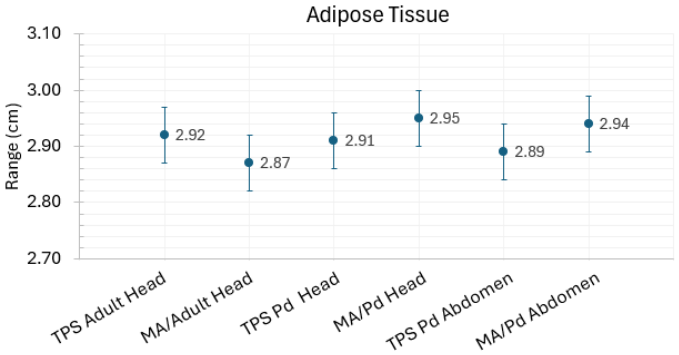

Figure 6.41.: Comparison of the ranges at 80% of the maximum dose for adipose tissue from TPS and FLUKA for the three calibration curves.

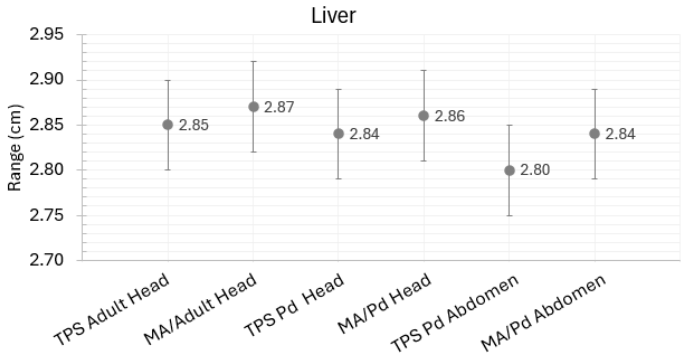

Figure 6.42.: Comparison of the ranges at 80% of the maximum dose for liver from TPS and FLUKA for the three calibration curves.

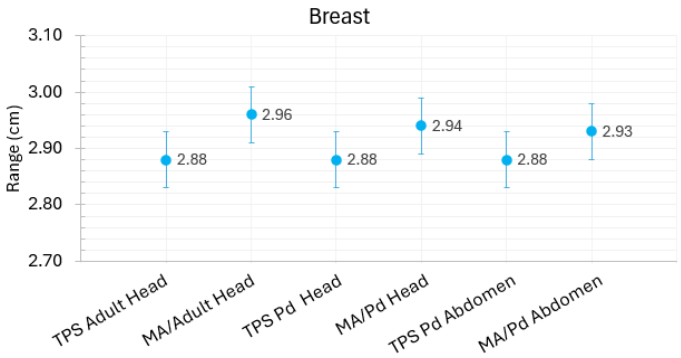

Figure 6.43.: Comparison of the ranges at 80% of the maximum dose for breast from TPS and FLUKA for the three calibration curves.

6.3. Influence of the Beam Model

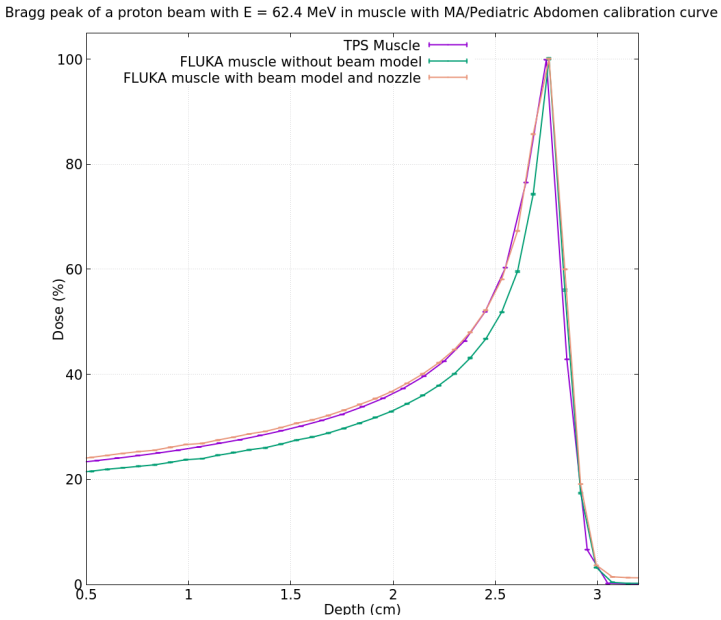

Figure 6.44.: Bragg curve for a 62.4 MeV proton beam in muscle material for MA/Pediatric Abdomen including the calibration curve.

The final simulations conducted aimed to examine the impact of the beam model on FLUKA Monte Carlo simulations. The muscle and Bone200 plans for the MA/Pediatric Abdomen calibration curve were used for the input. The nozzle geometry and the beam model were included in the input for the simulation. The results for the muscle plan are shown in Figure 6.44, and for the Bone200 plan in Figure 6.45 compared to 6.32. The ranges are listed in Table 6.21.

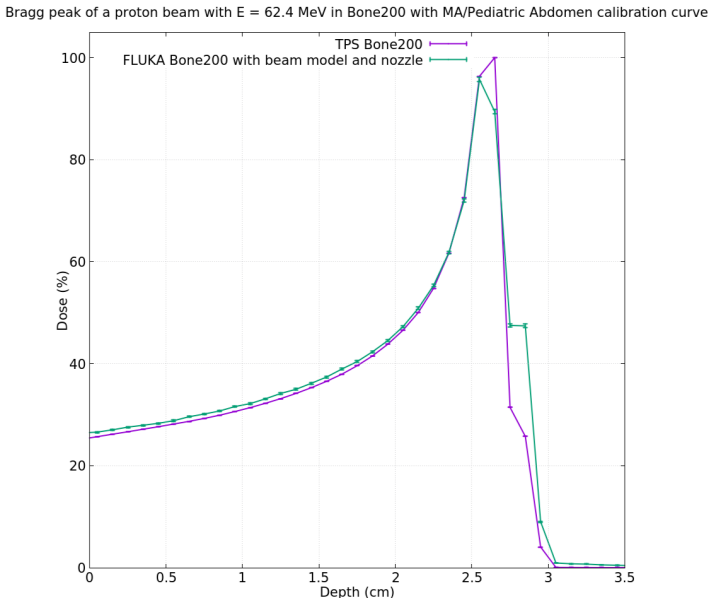

Figure 6.45.: Bragg curve for a 62.4 MeV proton beam in the Bone200 material for MA/Pediatric Abdomen including the calibration curve.

Material	**Curve**	**Range (cm)**
Muscle	TPS Pediatric Abdomen	2.78 ± 0.05
	MA/Pediatric Abdomen without Beam Model	2.80 ± 0.05
	MA/Pediatric Abdomen including Beam Model	2.80 ± 0.05
Bone200	TPS Pediatric Abdomen	2.68 ± 0.05
	MA/Pediatric Abdomen without Beam Model	2.64 ± 0.05
	MA/Pediatric Abdomen including Beam Model	2.67 ± 0.05

Table 6.21.: Ranges at 80% of the maximum dose of the muscle and Bone200 equivalent tissue for the MA/Pediatric Abdomen calibration curve from TPS, and FLUKA with and without the beam model.

7. Discussion

The overall capabilities of the FLUKA Particle Therapy Tool for dose recalculation of treatment plans have been evaluated in this thesis. The influence of several input parameters on the resulting Bragg curves was examined by computing the depth dose distribution of proton beams with two different nominal energies $E = 97.4$ MeV and $E = 62.4$ MeV for two different phantoms.

The differences in the range of the Bragg peaks calculated in TPS and in FLUKA with the use of the MA/Adult Head curve were small for the acrylic (6.2), nylon (6.3), and Lexan (6.4) materials, where the range differences were 0.1 mm for acrylic, 0.3 mm for nylon, and 0.2 mm for Lexan. However, for polyethylene (6.7), the difference was slightly higher at 0.5 mm. In the case of the Teflon material (6.5), a secondary peak is present both in the TPS plan and in the results of the FLUKA simulations, which as already mentioned and shown in Figure 6.6, is caused by a misalignment of the beam at the moment of editing the plan, which causes the beam to also interact with the surrounding material. The higher range difference of 1.2 mm could be caused by several factors, such as the different methods used by each program to account for heterogeneities, resulting in different scattering; the averaging of densities during voxalization, or the lack of implementation of the beam model in this simulation, which affects the size and divergence of the beam, resulting in a difference of the dose distribution, especially at the interface of two materials. The effect of the beam model can also be observed in the tissue equivalent phantom results discussed below. The repetition of this plan would be of interest, but due to time constraints was beyond the scope of this work. For the Schneider curve, the difference in the range of the Bragg peaks was slightly higher than for the MA/Adult Head curve for the acrylic and nylon samples, where the range difference was 0.5 mm. This was also the range difference for the polyethylene material in both cases. For Lexan, the range difference was equal to 0.4 mm and for Teflon, also a higher range difference of 1.1 mm was measured.

For the tissue equivalent phantom, the difference between the TPS and FLUKA ranges of the soft tissue is the smallest on average for all three calibration curves, while the range difference is the highest for the lung tissue. These differences can arise from the fact that more samples and therefore more points were available for the linear regression of the soft tissue, while only two points (LungIn and LungEx) were available for the linear regression of the lung tissue. The range difference in the muscle plan goes from 0.2 mm for the Adult Head curve to 0.5 mm for the Pediatric Head curve. For the adipose tissue, the difference in the range goes from 0.4 mm for the Pediatric Head curve to 0.5 mm for the Pediatric Abdomen curve. The differences in the liver equivalent material are the smallest in the soft tissue category, being between 0.2 mm and 0.4 mm, and the highest for the breast equivalent material between 0.5 mm for the Pediatric Abdomen curve and 0.8 mm for the

Adult Head curve. For the LungEx plans, the range difference between the two softwares is 1.1 mm for the MA/Adult Head curve, 1.0 mm for the MA/Pediatric Head curve, and 0.7 mm for the MA/Pediatric Abdomen curve, while for the LungIn plans, it goes from 1.0 mm for the MA/Pediatric Abdomen curve and 2.0 mm for the MA/Adult Head curve. Several factors can contribute to the observed differences for lung tissue including mentioned already limitation in number of points for the interpolation of CT calibration curve in this region. The lower density of these materials results in a longer range for the beam compared to the range of the beam in the other materials analyzed, with a difference of several centimeters. As a result, the beam is more capable of scattering over the longer path, leading to a notable alteration in the range of the Bragg peaks. This could contribute to the range difference, especially when the beam size and divergence differ. The skeletal tissue plans present a secondary peak, which is caused by the beam being of a larger diameter than the material sample of the phantom, thus allowing for interaction with the surrounding material. The range differences for the Bone200 material are the highest in this category, with 0.9 mm for the MA/Adult Head curve, 0.8 mm for the MA/Pediatric Head curve and 0.4 mm for the MA/Pediatric Abdomen curve, and the lowest for the Bone800 material with 0.2 mm for the MA/Pediatric Head curve, 0.2 mm for the MA/Pediatric Abdomen curve and a significantly higher difference of 0.6 mm for the Adult Head curve. The range differences for the Bone1250 material are found between 0.1 mm and 0.8 mm. The skeletal tissue typically presents greater deviations in the calibration curves, due to the presence of inhomogeneities and the stronger influence of CT parameters. This is apparent when comparing the calibration curves presented in Table 5.1.

The accuracy of the x-axis dose calculation in TPS is limited by the resolution of the dose grid, which is 1 mm. This resolution was also employed for the scoring of the dose in FLUKA. Despite the differences in range, all the curves of the phantom with materials of known densities, with the exception of the Teflon curve, as well as the ranges of the samples in the soft tissue and skeletal tissue categories, are within this resolution limit. For the error in the y-axis, TPS is set to 0.5%, while in FLUKA it is a statistical error depending on the number of primaries, as described in 5.1, which is represented by the error bars in the plots. A constant deviation among all dose distributions is the lower dose deposition in the plateau area. This deviation is attributed to the difference in beam size and shape resulting from the missing beam model file and nozzle geometry, which as already mentioned, influence the divergence and scattering of the beam. The beam model file specifies the momentum, angular, and position spread of the beam [6]. Section 5.4 shows the Bragg curve of the muscle and Bone200 plans for the MA/Pediatric Abdomen calibration curve, including the beam model file and nozzle geometry in the input, and compares this to the previously discussed plans for the Pediatric Abdomen calibration curve from Figure 6.26 and 6.32.

In the case of the muscle plan, it is clear that even if the ranges for the curves with and without a beam model are the same, the overall shape of the curve differs, especially in the plateau area. In the case of Bone200, in addition to the plateau area being influenced by the beam model, the difference in range between the Bragg peaks obtained with TPS and

with FLUKA decreases from 0.4 mm to 0.1 mm. Further simulations for the remaining samples implementing the beam model are needed to evaluate its effects. The treatment plans analyzed in this thesis were simplified as described in Chapter 5 to evaluate the effect of input parameters such as the calibration curves. Typical treatment plans employ multiple spots with varying energies to cover the target volume, and the commissioned energies in TPS are not discrete but a spectrum. This fact has been accounted for in the ray model simulations.

Sources of error arise from the limited number of available points compared to the defined HU materials used for the FLUKA material files, especially outside the soft tissue area, coupled with the processing of the calibration curve in both softwares, since in FLUKA each Hounsfield unit range is related to a material with specific elemental composition and properties, while in TPS the mass density calculated for corresponding HU is connected to material properties interpolated from the list of core 10 materials. The primary source of error is the missing beam model file, which, as discussed earlier, defines the shape and size of the beam. This leads to inaccuracies in the beam dispersion and scattering, causing a variation in the dose distribution, which alters the range and overall shape of the Bragg curve. The physical models and approximations utilized in both programs, including those for electronic stopping power and multiple Coulomb scattering, also influence the results. Furthermore, the number of primaries utilized for the Monte Carlo simulations can be increased to achieve higher accuracy, although this results in a longer simulation time.

8. Conclusion and Outlook

In this thesis, necessary input parameters were adjusted and implemented with the objective of recalculating MedAustron treatment plans using the FLUKA Monte Carlo code. The recalculated dose distributions presented in this thesis indicate that FLUKA can be used as a research tool in the clinical setting at the MedAustron particle therapy center, when all required input parameters are configured. In addition, the capability of generating plans with reasonable results with a minimal configuration, as suggested by Kozlowska et at. [6] was verified, while highlighting the advantages of adapting the initial parameters as closely as possible to the parameters used in the treatment planning system, to improve the accuracy of the results.

This work served as a proof of concept for dose recalculation at MedAustron using the FLUKA Particle Therapy Tool. Nevertheless, further work is required before a comparison of dose distributions for clinical patient plans can be performed. The beam model and nozzle geometry were not available until a late stage of the project and are therefore not included in most of the simulations. However, these factors have a significant impact on the results for the ranges and dose distributions. Additional simulations are necessary for the remaining samples to evaluate its effects. The next steps in the development of this project would involve the full commissioning of the beam model for the proton beam for different nozzles used in MedAustron, as well as the creation and commissioning of a beam model for carbon. Furthermore, in order to be able to calculate the RBE dose for carbon beams and directly compare it with the dose from the TPS, the radiobiological models for carbon ions should be implemented.

Bibliography

[1] R A Hälg et al. 'Measurements of the neutron dose equivalent for various radiation qualities, treatment machines and delivery techniques in radiation therapy'. In: *Physics in Medicine and Biology* 59.10 (Apr. 2014), pp. 2457–2468. ISSN: 1361-6560. DOI: 10.1088/0031-9155/59/10/2457.

[2] H Paganetti. 'Monte Carlo simulations will change the way we treat patients with proton beams today'. In: *The British Journal of Radiology* 87.1040 (Aug. 2014), p. 20140293. ISSN: 1748-880X. DOI: 10.1259/bjr.20140293.

[3] Wioletta Kozłowska. 'Bridging the gaps in Particle Therapy using Monte Carlo Codes'. PhD thesis. Medical University of Vienna, 2022.

[4] Giuseppe Battistoni et al. 'The FLUKA code: An accurate simulation tool for particle therapy'. In: *Frontiers in Oncology* 6 (May 2016). DOI: 10.3389/fonc.2016.00116.

[5] Lamberto Widesott et al. 'Improvements in pencil beam scanning proton therapy dose calculation accuracy in brain tumor cases with a commercial Monte Carlo algorithm'. In: *Physics in Medicine and Biology* 63.14 (July 2018), p. 145016. ISSN: 1361-6560. DOI: 10.1088/1361-6560/aac279.

[6] Wioletta Kozlowska et al. 'FLUKA particle therapy tool for Monte Carlo independent calculation of scanned proton and carbon ion beam therapy'. In: *Physics in Medicine and Biology* 64 (Mar. 2019). DOI: 10.1088/1361-6560/ab02cb.

[7] M Benedikt et al. 'Overview of the MedAustron design and technology choices'. In: (2010). URL: https://cds.cern.ch/record/1272158.

[8] E. Griesmayer, T. Schreiner and Márius Pavlovič. 'The MedAustron project'. In: *Nuclear Instruments and Methods in Physics Research Section B: Beam Interactions with Materials and Atoms* 258 (May 2007), pp. 134–138. DOI: 10.1016/j.nimb.2006.12.082.

[9] L Badano et al. *Proton-Ion Medical Machine Study (PIMMS), 1*. 2000. URL: https://cds.cern.ch/record/385378.

[10] MedAustron. *MedAustron - Center for Ion Therapy and Research*. 2024. URL: https://www.medaustron.at/ (visited on 25/08/2024).

[11] J. Lettry et al. 'Ion sources for MedAustron'. In: *Review of Scientific Instruments* 81.2 (Feb. 2010). ISSN: 1089-7623. DOI: 10.1063/1.3277196.

[12] M. Benedikt and A. Wrulich. 'MedAustron—Project overview and status'. In: *The European Physical Journal Plus* 126.7 (July 2011). ISSN: 2190-5444. DOI: 10.1140/epjp/i2011-11069-9.

[13] Liviu Penescu et al. 'Commissioning and Operation of the MedAustron Injector: Results and Future Outlook'. In: June 2014.

[14] Cai Grau et al. 'Particle therapy in Europe'. In: *Molecular Oncology* 14.7 (Apr. 2020), pp. 1492–1499. ISSN: 1878-0261. DOI: 10.1002/1878-0261.12677.

[15] Timothy Malouff et al. 'Carbon Ion Therapy: A Modern Review of an Emerging Technology'. In: *Frontiers in Oncology* 10 (Feb. 2020), p. 82. DOI: 10.3389/fonc.2020.00082.

[16] Wayne Newhauser and Rui Zhang. 'The physics of proton therapy'. In: *Physics in medicine and biology* 60 (Mar. 2015), R155–R209. DOI: 10.1088/0031-9155/60/8/R155.

[17] *Diagnostic Radiology Physics*. Non-serial Publications. Vienna: INTERNATIONAL ATOMIC ENERGY AGENCY, 2014. ISBN: 978-92-0-131010-1. URL: https://www.iaea.org/publications/8841/diagnostic-radiology-physics.

[18] Anton Lechner. 'Particle interactions with matter'. en. In: *CERN Yellow Reports: School Proceedings* Vol 5 (2018 2018), Extraction and Transfer. DOI: 10.23730/CYRSP-2018-005.47.

[19] J H Hubbell. 'Review of photon interaction cross section data in the medical and biological context.' In: *Physics in medicine and biology* 44 1 (1999), R1–22. URL: https://api.semanticscholar.org/CorpusID:4658362.

[20] C. W. Fabjan and D. Fournier. 'Calorimetry'. In: *Particle Physics Reference Library: Volume 2: Detectors for Particles and Radiation*. Ed. by Christian W. Fabjan and Herwig Schopper. Cham: Springer International Publishing, 2020, pp. 201–280. ISBN: 978-3-030-35318-6. DOI: 10.1007/978-3-030-35318-6_6. URL: https://doi.org/10.1007/978-3-030-35318-6_6.

[21] Edward L. Alpen. 'Radiation Biophysics (Second Edition)'. In: *Radiation Biophysics*. Ed. by Edward L. Alpen. Second Edition. San Diego: Academic Press, 1998, pp. 365–392. ISBN: 978-0-12-053085-4. DOI: https://doi.org/10.1016/B978-012053085-4/50016-8. URL: https://www.sciencedirect.com/science/article/pii/B9780120530854500168.

[22] Michael F. L'Annunziata. 'Neutron Radiation'. In: *Radioactivity*. Elsevier, 2007, pp. 253–288. ISBN: 9780444527158. DOI: 10.1016/b978-044452715-8.50007-4.

[23] E.B. Podgorsak. *Radiation Physics for Medical Physicists*. Graduate Texts in Physics. Springer International Publishing, 2016. ISBN: 9783319253824. URL: https://books.google.at/books?id=lwpwDQAAQBAJ.

[24] Phillip M. Rinard. 'Neutron Interactions with Matter'. In: 1997. URL: https://api.semanticscholar.org/CorpusID:44224507.

[25] H. Bethe. 'Zur Theorie des Durchgangs schneller Korpuskularstrahlen durch Materie'. In: *Annalen der Physik* 397.3 (Jan. 1930), pp. 325–400. ISSN: 1521-3889. DOI: 10.1002/andp.19303970303.

[26] Linda Hong et al. 'A pencil beam algorithm for proton dose calculations'. In: *Physics in Medicine and Biology* 41.8 (Aug. 1996), pp. 1305–1330. ISSN: 1361-6560. DOI: 10.1088/0031-9155/41/8/005.

[27] E Pedroni et al. 'Experimental characterization and physical modelling of the dose distribution of scanned proton pencil beams'. In: *Physics in Medicine and Biology* 50.3 (Jan. 2005), pp. 541–561. ISSN: 1361-6560. DOI: 10.1088/0031-9155/50/3/011.

[28] Nicholas C Koch and Wayne D Newhauser. 'Development and verification of an analytical algorithm to predict absorbed dose distributions in ocular proton therapy using Monte Carlo simulations'. In: *Physics in Medicine and Biology* 55.3 (Jan. 2010), pp. 833–853. ISSN: 1361-6560. DOI: 10.1088/0031-9155/55/3/019.

[29] Gert Moliere. 'Theorie der Streuung schneller geladener Teilchen I. Einzelstreuung am abgeschirmten Coulomb-Feld'. In: *Zeitschrift für Naturforschung A* 2.3 (Mar. 1947), pp. 133–145. ISSN: 0932-0784. DOI: 10.1515/zna-1947-0302.

[30] Bernard Gottschalk. 'Radiotherapy Proton Interactions in Matter'. In: (2018). DOI: 10.48550/ARXIV.1804.00022.

[31] Virgil L. Highland. 'Some practical remarks on multiple scattering'. In: *Nuclear Instruments and Methods* 129.2 (Nov. 1975), pp. 497–499. ISSN: 0029-554X. DOI: 10.1016/0029-554x(75)90743-0.

[32] Dieter Schardt, Thilo Elsässer and Daniela Schulz-Ertner. 'Heavy-ion tumor therapy: Physical and radiobiological benefits'. In: *Reviews of Modern Physics* 82.1 (Feb. 2010), pp. 383–425. ISSN: 1539-0756. DOI: 10.1103/revmodphys.82.383.

[33] H Paganetti. 'Nuclear interactions in proton therapy: dose and relative biological effect distributions originating from primary and secondary particles'. In: *Physics in Medicine and Biology* 47.5 (Feb. 2002), pp. 747–764. ISSN: 1361-6560. DOI: 10.1088/0031-9155/47/5/305.

[34] International Atomic Energy Agency (IAEA). *Relative biological effectiveness in Ion Beam Therapy*. Technical reports series 461. Vienna: International Atomic Energy Agency, 2008. 153 pp. ISBN: 9789201078070.

[35] Uwe Schneider and Roger Haelg. 'The Impact of Neutrons in Clinical Proton Therapy'. In: *Frontiers in Oncology* 5 (Oct. 2015). ISSN: 2234-943X. DOI: 10.3389/fonc.2015.00235.

[36] Harald Paganetti. 'Range uncertainties in proton therapy and the role of Monte Carlo simulations'. In: *Physics in Medicine and Biology* 57.11 (May 2012), R99–R117. ISSN: 1361-6560. DOI: 10.1088/0031-9155/57/11/r99.

[37] Youngmo Ku, Jaerin Jung and Chan Hyeong Kim. 'New algorithm to estimate proton beam range for multi-slit prompt-gamma camera'. In: *Nuclear Engineering and Technology* 54.9 (2022), pp. 3422–3428. ISSN: 1738-5733. DOI: https://doi.org/10.1016/j.net.2022.04.019. URL: https://www.sciencedirect.com/science/article/pii/S1738573322002406.

[38] Hui Liu and Joe Y. Chang. 'Proton therapy in clinical practice'. In: *Chinese Journal of Cancer* 30.5 (May 2011), pp. 315–326. ISSN: 1944-446X. DOI: 10.5732/cjc.010.10529.

[39] Sh Keshazare, S F Masoudi and F S Rasouli. 'Effects of Defining Realistic Compositions of the Ocular Melanoma on Proton Therapy'. In: *Journal of Biomedical Physics and Engineering* 4.4 (2014). ISSN: 2251-7200. eprint: https://jbpe.sums.ac.ir/article_43176_3eb5b87641e2bcdffd81c1804a3c5a38.pdf. URL: https://jbpe.sums.ac.ir/article_43176.html.

[40] Tomas Kron, Joerg Lehmann and Peter B Greer. 'Dosimetry of ionising radiation in modern radiation oncology'. In: *Physics in Medicine and Biology* 61.14 (June 2016), R167–R205. ISSN: 1361-6560. DOI: 10.1088/0031-9155/61/14/r167.

[41] International Atomic Energy Agency (IAEA). *Dosimetry in diagnostic radiology. An international code of practice*. Ed. by International Atomic Energy Agency. Technical reports series 457. Vienna: International Atomic Energy Agency, 2007. 359 pp. ISBN: 9789201154064.

[42] Sven Ove Hansson. 'ALARA: What is Reasonably Achievable?' In: *Social and Ethical Aspects of Radiation Risk Management*. Elsevier, 2013, pp. 143–155. DOI: 10.1016/b978-0-08-045015-5.00009-5.

[43] ICRP. 'ICRP Publication 26'. In: *Recommendations of the ICRP* (1977).

[44] International Commission on Radiation Units and Measurements (ICRU). *Prescribing, recording, and reporting photon beam therapy*. ICRU report 78. Oxford: Oxford Univ. Press, 2007. 210 pp. ISBN: 9780199543489.

[45] Ervin B. Podgorsak, ed. *Radiation oncology physics. A handbook for teachers and students*. STI/PUB 1196. Vienna: International Atomic Energy Agency, 2005. 657 pp. ISBN: 9201073046.

[46] J. Valentin, ed. *The 2007 recommendations of the International Commission on Radiological Protection*. Annals of the ICRP 37.2007,2/4. Literaturverz. S. 321 - 332. Oxford [u.a.]: Elsevier, 2007. 332 pp. ISBN: 9780702030482.

[47] Harald Paganetti. 'Dose to water versus dose to medium in proton beam therapy'. In: *Physics in Medicine and Biology* 54.14 (June 2009), pp. 4399–4421. ISSN: 1361-6560. DOI: 10.1088/0031-9155/54/14/004.

[48] Lars Fredrik Fjæra. 'Development of a Monte Carlo Based Treatment Planning Verification Tool for Particle Therapy'. MA thesis. The University of Bergen, 2016.

[49] Eidi Helland. 'Monte Carlo simulations of neutron based in-vivo range verification in proton therapy – characterstics of proton-induced secondary particles'. MA thesis. The University of Bergen, 2019.

[50] J Bauer et al. 'Integration and evaluation of automated Monte Carlo simulations in the clinical practice of scanned proton and carbon ion beam therapy'. In: *Physics in Medicine and Biology* 59.16 (July 2014), pp. 4635–4659. ISSN: 1361-6560. DOI: 10.1088/0031-9155/59/16/4635.

[51] *Absorbed Dose Determination in External Beam Radiotherapy*. Technical Reports Series 398. Vienna: INTERNATIONAL ATOMIC ENERGY AGENCY, 2001. ISBN: 92-0-102200-X. URL: https://www.iaea.org/publications/5954/absorbed-dose-determination-in-external-beam-radiotherapy.

[52] Rui Zhang and Wayne Newhauser. 'Calculation of water equivalent thickness of materials of arbitrary density, elemental composition and thickness in proton beam irradiation'. In: *Physics in medicine and biology* 54.6 (Mar. 2009), pp. 1383–95. ISSN: 1361-6560. DOI: 10.1088/0031-9155/54/6/001.

[53] Eric J. Hall and Amato J. Giaccia. *Radiobiology for the radiologist*. 7th ed. Includes bibliographical references and index. Philadelphia, Pa.: Wolters Kluwer Lippincott Williams, Wilkins, 2012. 546 pp. ISBN: 9781608311934.

[54] Eleanor A. Blakely et al. 'Heavy-Ion Radiobiology: Cellular Studies'. In: *Advances in Radiation Biology*. Elsevier, 1984, pp. 295–389. DOI: 10.1016/b978-0-12-035411-5.50013-7.

[55] Christopher B. Sylvester et al. 'Radiation-Induced Cardiovascular Disease: Mechanisms and Importance of Linear Energy Transfer'. In: *Frontiers in Cardiovascular Medicine* 5 (Jan. 2018). ISSN: 2297-055X. DOI: 10.3389/fcvm.2018.00005.

[56] Jinhyun Choi and Jin Oh Kang. 'Basics of particle therapy II: relative biological effectiveness'. In: *Radiation Oncology Journal* 30.1 (2012), p. 1. ISSN: 2234-3156. DOI: 10.3857/roj.2012.30.1.1.

[57] Nadine Barrie Smith. *Introduction to medical imaging. Physics, engineering and clinical applications*. Ed. by Andrew G. Webb. Repr. Cambridge texts in biomedical engineering. Formerly CIP Uk. Cambridge: Cambridge University Press, 2012. 286 pp. ISBN: 9780521190657.

[58] Lois E. Romans. *Computed tomography for technologists. a comprehensive text*. Wolters Kluwer Health/Lippincott Williams, Wilkins, 2011, p. 379. ISBN: 9780781777513.

[59] Mario Mustra, Kresimir Delac and M. Grgic. 'Overview of the DICOM standard'. In: vol. 1. Oct. 2008, pp. 39–44.

[60] Medical Imaging Technology Association (MITA). *Digital Imaging and Communications in Medicine (DICOM) Standard*. (available free at http://medical.nema.org/). NEMA PS3 / ISO 12052. URL: https://www.dicomstandard.org/.

[61] Michele Larobina. 'Thirty Years of the DICOM Standard'. In: *Tomography* 9.5 (2023), pp. 1829–1838. ISSN: 2379-139X. DOI: 10.3390/tomography9050145. URL: https://www.mdpi.com/2379-139X/9/5/145.

[62] Kevin L. Moore. 'Automated Radiotherapy Treatment Planning'. In: *Seminars in Radiation Oncology* 29.3 (July 2019), pp. 209–218. ISSN: 1053-4296. DOI: 10.1016/j.semradonc.2019.02.003.

[63] David Craft et al. 'Shared data for intensity modulated radiation therapy (IMRT) optimization research: the CORT dataset'. In: *GigaScience* 3.1 (Dec. 2014). ISSN: 2047-217X. DOI: 10.1186/2047-217x-3-37.

[64] Martin Janson et al. 'Treatment planning of scanned proton beams in RayStation'. In: *Medical Dosimetry* 49.1 (2023), pp. 2–12. ISSN: 0958-3947. DOI: https://doi.org/10.1016/j.meddos.2023.10.009. URL: https://www.sciencedirect.com/science/article/pii/S095839472300105X.

[65] Ahmed Eldib et al. 'Dosimetric evaluation of the capabilities of two clinical treatment planning systems for prostate cancer'. In: *Radiation Physics and Chemistry* 188 (Nov. 2021), p. 109642. ISSN: 0969-806X. DOI: 10.1016/j.radphyschem.2021.109642.

[66] Martin Janson et al. 'Treatment planning of scanned proton beams in RayStation'. In: *Medical Dosimetry* (2023). ISSN: 0958-3947. DOI: https://doi.org/10.1016/j.meddos.2023.10.009. URL: https://www.sciencedirect.com/science/article/pii/S095839472300105X.

[67] IndraJ Das et al. 'Computed tomography imaging parameters for inhomogeneity correction in radiation treatment planning'. In: *Journal of Medical Physics* 41.1 (2016), p. 3. ISSN: 0971-6203. DOI: 10.4103/0971-6203.177277.

[68] R. Cropp et al. 'Scanner and kVp dependence of measured CT numbers in the ACR CT phantom'. In: *Journal of Applied Clinical Medical Physics* 14 (2013), pp. 338–349. URL: https://api.semanticscholar.org/CorpusID:4560343.

[69] Esther Bär et al. 'Assessment of the impact of CT calibration procedures for proton therapy planning on pediatric treatments'. In: *Medical Physics* 48.9 (July 2021), pp. 5202–5218. ISSN: 2473-4209. DOI: 10.1002/mp.15062.

[70] T. Landberg et al. '2. Definitions of Terms and Concepts'. In: *Reports of the International Commission on Radiation Units and Measurements* os-26.1 (1993), pp. 3–26. DOI: 10.1093/jicru_os26.1.3. eprint: https://doi.org/10.1093/jicru_os26.1.3. URL: https://doi.org/10.1093/jicru_os26.1.3.

[71] T. Landberg et al. '2. Volumes'. In: *Reports of the International Commission on Radiation Units and Measurements* os-32.1 (1999), pp. 3–20. DOI: 10.1093/jicru_os32.1.3. eprint: https://doi.org/10.1093/jicru_os32.1.3. URL: https://doi.org/10.1093/jicru_os32.1.3.

[72] Stewart Mein et al. 'Spot-Scanning Hadron Arc (SHArc) Therapy: A Study With Light and Heavy Ions'. In: *Advances in Radiation Oncology* 6.3 (May 2021), p. 100661. ISSN: 2452-1094. DOI: 10.1016/j.adro.2021.100661.

[73] A.M. Johansen. 'Monte Carlo Methods'. In: *International Encyclopedia of Education (Third Edition)*. Ed. by Penelope Peterson, Eva Baker and Barry McGaw. Third Edition. Oxford: Elsevier, 2010, pp. 296–303. ISBN: 978-0-08-044894-7. DOI: https://doi.org/10.1016/B978-0-08-044894-7.01543-8. URL: https://www.sciencedirect.com/science/article/pii/B9780080448947015438.

[74] Jacob Bernoulli. *Ars conjectandi: opus posthumum. Accedit Tractatus de seriebus infinitis, et epistola Gallicè scripta de ludo pilae reticularis. Basileae, Impensis Thurnisiorum, 1713*. Culture et civilisation, 1713.

[75] Oleg N. Vassiliev. *Monte Carlo Methods for Radiation Transport. Fundamentals and Advanced Topics*. SpringerLink. [Cham]: Springer, 2017. 2813832 pp. ISBN: 9783319441412.

[76] Alfredo Ferrari et al. 'FLUKA: a multi-particle transport code'. In: *CERN Yellow report* 2005-10 (Jan. 2005). DOI: 10.2172/877507.

[77] Alfredo Ferrari et al. 'FLUKA: a multi-particle transport code'. In: *CERN Yellow report* 2005-10 (Jan. 2005). DOI: 10.2172/877507.

[78] ICRU. 'Stopping Powers and Ranges for Protons and Alpha Par-ticles, International Commission on Radiation Units and Measurements'. In: *ICRU Report* 49 (1993).

[79] J. F. Ziegler. *The Stopping and Ranges of Ions in Matter. Handbook of Stopping Cross-Sections for Energetic Ions in All Elements*. Description based upon print version of record. Burlington: Elsevier Science, 2013. 437 pp. ISBN: 9780080216072.

[80] R.M. Sternheimer, M.J. Berger and S.M. Seltzer. 'Density effect for the ionization loss of charged particles in various substances'. In: *Atomic Data and Nuclear Data Tables* 30.2 (Mar. 1984), pp. 261–271. ISSN: 0092-640X. DOI: 10.1016/0092-640x(84)90002-0.

[81] Walter H. Barkas, John N. Dyer and Harry H. Heckman. 'Resolution of the sigma - Mass Anomaly'. In: *Physical Review Letters* 11.3 (Aug. 1963), pp. 138–138. ISSN: 0031-9007. DOI: 10.1103/physrevlett.11.138.

[82] F. Bloch. 'Zur Bremsung rasch bewegter Teilchen beim Durchgang durch Materie'. In: *Annalen der Physik* 408.3 (Jan. 1933), pp. 285–320. ISSN: 1521-3889. DOI: 10.1002/andp.19334080303.

[83] Alberto Fasso et al. 'New developments in FLUKA modelling of hadronic and EM interactions'. In: vol. 97. Jan. 1997.

[84] A. Ferrari et al. 'An improved multiple scattering model for charged particle transport'. In: *Nuclear Instruments and Methods in Physics Research Section B: Beam Interactions with Materials and Atoms* 71.4 (1992), pp. 412–426. ISSN: 0168-583X. DOI: https://doi.org/10.1016/0168-583X(92)95359-Y. URL: https://www.sciencedirect.com/science/article/pii/0168583X9295359Y.

[85] A. Fassò et al. 'FLUKA: Status and Prospects for Hadronic Applications'. In: *Advanced Monte Carlo for Radiation Physics, Particle Transport Simulation and Applications*. Springer Berlin Heidelberg, 2001, pp. 955–960. ISBN: 9783642182112. DOI: 10.1007/978-3-642-18211-2_153.

[86] Vasilis Vlachoudis. 'FLAIR: A POWERFUL BUT USER FRIENDLY GRAPHICAL INTERFACE FOR FLUKA'. In: Apr. 2009.

[87] T.T. Böhlen et al. 'The FLUKA Code: Developments and Challenges for High Energy and Medical Applications'. In: *Nuclear Data Sheets* 120 (2014), pp. 211–214. ISSN: 0090-3752. DOI: https://doi.org/10.1016/j.nds.2014.07.049. URL: https://www.sciencedirect.com/science/article/pii/S0090375214005018.

[88] RaySearch Laboratories AB. *RAYSTATION 11B SPC3, Instructions for Use*. RaySearch Laboratories AB. Oct. 2022.

[89] Yoichi Watanabe. 'Derivation of linear attenuation coefficients from CT numbers for low-energy photons'. In: *Physics in Medicine and Biology* 44.9 (Sept. 1999), p. 2201. DOI: 10.1088/0031-9155/44/9/308. URL: https://dx.doi.org/10.1088/0031-9155/44/9/308.

[90] Katia Parodi et al. 'Clinical CT-based calculations of dose and positron emitter distributions in proton therapy using the FLUKA Monte Carlo code'. In: *Physics in Medicine and Biology* 52 (2007), pp. 3369–3387. URL: https://api.semanticscholar.org/CorpusID:39836804.

[91] Wilfried Schneider, Thomas Bortfeld and Wolfgang Schlegel. 'Correlation between CT numbers and tissue parameters needed for Monte Carlo simulations of clinical dose distributions'. In: *Physics in medicine and biology* 45.2 (Mar. 2000), pp. 459–78. ISSN: 1361-6560. DOI: 10.1088/0031-9155/45/2/314.

[92] F. Ballarini et al. 'The physics of the FLUKA code: Recent developments'. In: *Advances in Space Research* 40.9 (Jan. 2007), pp. 1339–1349. ISSN: 0273-1177. DOI: 10.1016/j.asr.2007.05.031.

Acronyms

ALARA As Low As Reasonably Achievable. 17

CSDA Continuous Slowing Down Approximation. 13, 20

CT Computer tomography. xi, xiii, xiv, 23–27, 31, 34, 36–39, 41, 42, 46

CTV Clinical Target Volume. 27, 28

DICOM Digital Imaging and Communications in Medicine. 1, 25, 31, 34, 35, 40–42

DNA Deoxyribonucleic Acid. 21, 22

DVH Dose-Volume-Histogram. 34, 46

FOI Field Of View. 26

FOV Field Of View. 36

FWHM Full Width at Half Maximum. 47

GTV Gross Tumor Volume. 27, 28

GUI Graphical User Interface. 34

HU Hounsfield Unit. xi, xiii, 24, 26, 27, 36–38, 77

IAEA International Atomic Energy Agency. 20

ICRP International Commission on Radiological Protection. xi, 17, 18, 34

ICRU International Commission on Radiation Units and Measurements. xiii, 21, 27, 33, 34

LEBT Low Energy Beam Transfer. 2

LET Linear Energy Transfer. 17, 19, 21, 22

LINAC Linear Accelerator. 2

MA MedAustron. xi, xii, xiv–xvi, 36, 37, 39, 41, 43, 45, 47, 49–69, 73–76

MC Monte Carlo. 31, 32

MCS Multiple Coloumb Scattering. 11

MEBT Medium-Energy Beam Transfer. 3

MRI Magnetic Resonance Imaging. 23

OAR Organs At Risk. 26–28

PBS Pencil Beam Scanner. 35

PET Positron Emission Tomography. 23

PIMMS Proton-Ion Medical Machine Study. 2

PTV Planning Target Volume. 27, 28

QA Quality Assurance. 44

RBE Relative Biological Effectiveness. 17, 22, 79

ROI Region Of Interest. xiii, xiv, 25, 28, 34, 39, 40, 44–46

RTDOSE Radiation Therapy Dose Module. 34, 42

RTPLAN Radiation Therapy Plan Module. 34, 35, 42, 47

RTSTRUCT Radiation Therapy Structure Module. 34

RV Target Volume. 26

SOBP Spread Out Bragg Peak. 15

SS Single Scattering. 35

TPS Treatment Planning System. xiv–xvi, 1, 29, 34, 35, 39–43, 46, 47, 51, 52, 54–56, 60, 61, 66, 70–73, 75–77, 79

WET Water Equivalent Thickness. xiii, 20, 21

A. Appendix

A.1. CT Scanning Parameters

This section presents the parameters used to prepare the CT protocols to generate the calibration curves.

CT protocol name	**MA/Adult Head**	**MA/Pediatric Head**	**MA/Pediatric Abdomen**
FOV (mm)	350	350	400
kVp	120	120	120
mAs	300	150	200
Collimation (mm)	16x0.75	16x0.75	16x1.5
Pitch	0.563	0.563	0.813
Slice thickness (mm)	2	2	3
Increment (mm)	2	2	3
Rotation time (s)	0.75	0.75	0.76
Filter	UB	UB	B
Enhancement	0	0	0
Dose right	No	No	No
Angular Modulation	No	No	No
Resolution	Standard	Standard	Standard
SP Filter (CB)	On	On	On
Adaptive filter (streak)	Off	Off	Yes
Center (mm)	0x0	0x0	0x0
Matrix	512	512	512

Table A.1.: Parameters used to generate the calibration curve by scanning the tissue equivalent phantom with a Phillips CT machine.

A.2. Calibration Curve

This section presents the material file prepared and used for the MA/Adult Head calibration curve.

$\mathbf{HU_{Max}}$	Material name	$C\rho_{\mathbf{Min}}$	$C\rho_{\mathbf{Max}}$	$\mathbf{dE/dx_{Min}}$	$\mathbf{dE/dx_{Max}}$
-950	AIR	1	1	1	1
-925	HU<-925	0.89472853891055	1.16517545243515	1	1
-900	HU<-900	0.928082496221887	1.14143479420393	1	1
-830	HU<-830	0.808042962407894	1.23891594854502	1	1
-700	HU<-700	0.765598003455558	1.2608946054905	1	1
-500	HU<-500	0.773312048079632	1.24049206498263	1	1
-120	HU<-120	0.738508753574667	1.2672107135384	1	1
-83	HU<-83	0.98208616094377	1.0209635546033	1	1
-53	HU<-53	0.990832320041451	1.02445967316816	1	1
-23	HU<-23	0.988242706311543	1.02385604113111	1	1
7	HU<7	0.985794274182379	1.02328148519819	1	1
18	HU<18	0.992009487518469	1.00548750612445	1	1
80	HU<80	0.969587672668561	1.04985879832506	1	1
120	HU<120	0.964396266841627	1.02891834275651	1	1
200	HU<200	0.999794803118993	1.05689080925376	1	1
300	HU<300	0.979639439096949	1.05207328833173	1	1
400	HU<400	0.981278317892658	1.04947114183393	1	1
500	HU<500	0.982765932236157	1.04711668120885	1	1
600	HU<600	0.984122300314156	1.04497614901189	1	1
700	HU<700	0.98536405729913	1.0430216556819	1	1
800	HU<800	0.986505141029082	1.04122995765947	1	1
900	HU<900	0.987557317413438	1.03958152861998	1	1
1000	HU<1000	0.988530587633202	1.03805984494137	1	1
1100	HU<1100	0.989433507040259	1.03665082988832	1	1
1200	HU<1200	0.990273437315874	1.03534241685012	1	1
1300	HU<1300	0.991056747634946	1.03412420290688	1	1
1400	HU<1400	0.991788976475098	1.03298717165547	1	1
1500	HU<1500	0.992474962769521	1.03192346966196	1	1
1600	HU<1600	0.993118952972273	1.03092622481387	1	1
2000	HU<2000	0.952167694580254	1.12086636037764	1	1
3070	HU<3070	0.968258120776106	1.28855766199847	1	1

Table A.2.: Table of correction factors and parameters for the MA/Adult Head calibration curve.

A.3. FLUKA Input File

In this section an example of the FLUKA input file is presented, in particular the input file for the MA/Adult Head muscle plan.

```
    !@dicom=rtplan
#define rtplan_beam1
!@dicom=rtplan
#if rtplan_beam1
!@dicom=rtplan
```

```
#define rtplan_spots1 2
!@dicom=rtplan
#define rtplan_weight1 1000000000
!@what.1=rtplan_weight1/Gy
!@dicom=rtplan
#define rtplan_norm1 160.217646
!@dicom=rtplan
#endif
!@what.1=int(rtplan_spots1)
!@dicom=rtplan
#define rtplan_spots 2
TITLE

GLOBAL         5000.
*Set the defaults for precision simulations
DEFAULTS                                                              HADROTHE
*Define the beam characteristics
BEAM        -0.05898
*Define the beam position
BEAMPOS
*Card to initialize special beam - SPOTBEAM
!@what.1=rtplan_spots
!@dicom=rtplan
SPECSOUR           2                                                  BEAMSPOT
*Defines beam source file for beam1
!@dicom=rtplan
#if rtplan_beam1
!@dicom=rtplan
#include RTPlan_RP1.2.752.243.1.1.20240426144642010.2600.10844_beam1.inp
!@dicom=rtplan
#endif
!@what.5=rtplan_spots
!@dicom=rtplan
SPOTTRAN      RTPLAN    RTPLAN                    1         2           INVERSE
GEOBEGIN                                                              COMBNAME
!@pos=[-30.05859375, -25.85859375, -24.5]
!@iop=[1.0, 0.0, 0.0, 0.0, 1.0, 0.0]
VOXELS    -30.058594-25.858594     -24.5                              LungInA
    0    0
*Black body
SPH blkbody    0.0 0.0 0.0 100000.0
RPP water      -30.05859375 30 -25.85859375 34.14 -44.35 -24.5
*Void sphere
```

```
SPH void       0.0 0.0 0.0 10000.0
END
*Black hole
BLKBODY      5 +blkbody -void
*Void around
VOID         5 +void  -water -VOXEL
WATER        5 +water
END
GEOEND
MATERIAL          15               1.82                                PHOSPHO
MATERIAL          16               2.07                                SULFUR
MATERIAL          17           0.003214                                CHLORINE
*..+....1....+....2....+....3....+....4....+....5....+....6....+....7..
ASSIGNMA    BLCKHOLE   BLKBODY
ASSIGNMA      VACUUM      VOID
*Voxel cage
ASSIGNMA      VACUUM     VOXEL
*Voxel cage
ASSIGNMA       WATER     WATER
*Isocenter translation
!@dicom=rtplan
ROT-DEFI         100                     11.72682 -4.318414  22.55008RTPLAN
*HFS Voxel Rotation
!@dicom=rtplan
ROT-DEFI         100         0        90                                RTPLAN
!@dicom=RTDOSE-2
!@pos=[-25.25, -25.25, -34.85]
!@iop=[1.0, 0.0, 0.0, 0.0, 1.0, 0.0]
USRBIN          10.0  DOSE-H2O     -99.0     25.35     25.35    -19.052-DOSE-H2O
USRBIN        -25.25    -25.25    -34.85       506       506       158 &
!@dicom=RTDOSE-2
!@pos=[-25.25, -25.25, -34.85]
!@iop=[1.0, 0.0, 0.0, 0.0, 1.0, 0.0]
USRBIN          10.0      DOSE       -98     25.35     25.35    -19.052-SQBETA-D
USRBIN        -25.25    -25.25    -34.85       506       506       158 &
RAD-BIOL                                                              example
*Set the random number seed
RANDOMIZ         1.0
*Set the number of primary histories to be simulated in the run
START          100000
STOP
```

A.4. Beam Model Input File

This section presents the FLUKA input file which includes the nozzle geometry.

```
    !@dicom=rtplan
#define rtplan_beam1
!@dicom=rtplan
#if rtplan_beam1
!@dicom=rtplan
#define rtplan_spots1 2
!@dicom=rtplan
#define rtplan_weight1 1000000000
!@what.1=rtplan_weight1/Gy
!@dicom=rtplan
#define rtplan_norm1 160.217646
!@dicom=rtplan
#endif
!@what.1=int(rtplan_spots1)
!@dicom=rtplan
#define rtplan_spots 2
#define RaShi
TITLE

GLOBAL         5000.
*Set the defaults for precision simulations
DEFAULTS                                                              HADROTHE
PHYSICS            1                                                  COALESCE
PHYSICS            3                                                  EVAPORAT
PHYSICS            1     0.001     0.150         2         2         3IONSPLIT
PHYSICS       1000.0    1000.0    1000.0    1000.0    1000.0    1000.0PEATHRES
*IONTRANS          -2
*MULSOPT           1.                             1.        1.        1.GLOBHAD
*Define the beam characteristics
BEAM        -0.05898
*Define the beam position
BEAMPOS
*Card to initialize special beam - SPOTBEAM
!@what.1=rtplan_spots
!@dicom=rtplan
SPECSOUR           2                                                  BEAMSPOT
*Defines beam source file for beam1
!@dicom=rtplan
#if rtplan_beam1
!@dicom=rtplan
```

```
#include RTPlan_RP1.2.752.243.1.1.20240427105250638.3250.54178_beam1.inp
!@dicom=rtplan
#endif
!@what.5=rtplan_spots
!@dicom=rtplan
SPOTTRAN      RTPLAN    RTPLAN                    1         2          INVERSE
*Rotating and shifting full nozzle depending on couch angle: change azm=couch angle-90
*and deltax=deltaz and deltaz=deltax of isocenter translation (for -Azm deltax=-deltaz)
#if rtplan_beam1
ROT-DEFI         200       180       180  22.55103  7.162421 0.1005328Nozzle
#endif
GEOBEGIN                                                                COMBNAME
!@pos=[-30.05859375, -25.85859375, -24.5]
!@iop=[1.0, 0.0, 0.0, 0.0, 1.0, 0.0]
VOXELS    -30.058594-25.858594     -24.5                                s
    0    0
*Black body
SPH blkbody    0.0 0.0 0.0 100000.0
*Void sphere
SPH void       0.0 0.0 0.0 10000.0
RPP water      -30.05859375 30 -25.85859375 34.14 -44.35 -24.5
$start_transform Nozzle
RPP AirGap     -100 100 -100 100 -177.65 113.35
*Nozzle upstream (exit to entrance)
RPP KapFoil    -35.5 35.5 -35.5 35.5 64.80 64.82
XYP KapP       64.8025
RPP RaShi      -35 35 -35 35 71.62 74.62
*DDS1 implementation
RPP DDS1       -35.5 35.5 -35.5 35.5 74.9425 86.9425
RPP DDS1_1     -35 35 -35 35 75.92558 75.92813
XYP DDS1_P1    75.92563
RPP DDS3_1     -35 35 -35 35 78.92813 78.92936
XYP DDS1_P2    78.92816
RPP DDS5_1     -35 35 -35 35 79.42936 79.43436
XYP DDS1_P3    79.43186
RPP DDS7_1     -35 35 -35 35 79.93686 79.93941
XYP DDS1_P4    79.93691
RPP DDS9_1     -35 35 -35 35 80.43941 80.44441
XYP DDS1_P5    80.44191
RPP DDS11_1    -35 35 -35 35 81.44691 81.45191
XYP DDS1_P6    81.44941
RPP DDS13_1    -35 35 -35 35 81.95441 81.95564
XYP DDS1_P7    81.95561
```

```
RPP DDS15_1    -35 35 -35 35 82.45564 82.45687
XYP DDS1_P8    82.45684
RPP DDS17_1    -35 35 -35 35 85.95687 85.95942
XYP DDS1_P9    85.95937
*DDS2implementation
RPP DDS2       -35.5 35.5 -35.5 35.5 87.1425 99.1425
RPP DDS1_2     -35 35 -35 35 88.12558 88.12813
XYP DDS2_P1    88.12563
RPP DDS3_2     -35 35 -35 35 91.12813 91.12936
XYP DDS2_P2    91.12816
RPP DDS5_2     -35 35 -35 35 91.62936 91.63436
XYP DDS2_P3    91.63186
RPP DDS7_2     -35 35 -35 35 92.13686 92.13941
XYP DDS2_P4    92.13691
RPP DDS9_2     -35 35 -35 35 92.63941 92.64441
XYP DDS2_P5    92.64191
RPP DDS11_2    -35 35 -35 35 93.64691 93.65191
XYP DDS2_P6    93.64941
RPP DDS13_2    -35 35 -35 35 94.15441 94.15564
XYP DDS2_P7    94.15561
RPP DDS15_2    -35 35 -35 35 94.65564 94.65687
XYP DDS2_P8    94.65684
RPP DDS17_2    -35 35 -35 35 98.15687 98.15942
XYP DDS2_P9    98.15937
*ITS implementation
RPP ITS        -35.5 35.5 -35.5 35.5 103.94249 112.94251
RPP ITS1_3     -35 35 -35 35 103.9425 103.94505
XYP ITSP_1     103.94255
RPP ITS3_3     -35 35 -35 35 107.94505 107.94628
XYP ITSP_2     107.94508
RPP ITS5_3     -35 35 -35 35 108.42999 108.43499
XYP ITSP_3     108.43249
RPP ITS7_3     -35 35 -35 35 108.93749 108.93872
XYP ITSP_4     108.93752
RPP ITS9_3     -35 35 -35 35 109.43872 109.43995
XYP ITSP_5     109.43875
RPP ITS11_3    -35 35 -35 35 112.93995 112.9425
XYP ITSP_6     112.9400
RPP VacW1      -35 35 -35 35 113.22 113.259001
XYP VacWP1     113.220001
XYP VacWP2     113.258001
RPP VacW2      -35 35 -35 35 113.639501 113.659002
XYP VacWP3     113.639502
```

```
XYP VacWP4     113.658502
$end_transform
END
*Black hole
BLKBODY      5 +blkbody -void
*Void around
VOID         5 +void -VOXEL -water -AirGap
WATER        5 +water
AirGap       5 +AirGap  -VacW1 -VOXEL -RaShi
               -(KapFoil+KapP) -ITS -DDS1 -DDS2-water
KapFoil      5 +KapFoil  +KapP
RaShi        5 +RaShi
DDS1         5 +DDS1 -DDS11_1  -DDS13_1
               -DDS15_1 -DDS17_1 -DDS1_1
               -DDS3_1 -DDS5_1  -DDS7_1
               -DDS9_1
DDSAl1       4 +DDS1_1 -DDS1_P1
               | +DDS3_1 -DDS1_P2
               | +DDS5_1 -DDS1_P3
               | +DDS7_1 -DDS1_P4
               | +DDS9_1 +DDS1_P5
               | +DDS11_1 -DDS1_P6
               | +DDS13_1 +DDS1_P7
               | +DDS15_1 +DDS1_P8
               | +DDS17_1 +DDS1_P9
DDSMyl1      4 +DDS1_1 +DDS1_P1
               | +DDS3_1 +DDS1_P2
               | +DDS7_1 +DDS1_P4
               | +DDS13_1 -DDS1_P7
               | +DDS15_1 -DDS1_P8
               | +DDS17_1 -DDS1_P9
DDSKap1      4 +DDS5_1 +DDS1_P3
               | +DDS9_1 -DDS1_P5
               | +DDS11_1 +DDS1_P6
DDS2         5 +DDS2  -DDS11_2 -DDS13_2
               -DDS15_2 -DDS17_2 -DDS1_2
               -DDS3_2 -DDS5_2  -DDS7_2
               -DDS9_2
DDSAl2       4 +DDS1_2 -DDS2_P1
               | +DDS3_2 -DDS2_P2
               | +DDS5_2 -DDS2_P3
               | +DDS7_2 -DDS2_P4
               | +DDS9_2 +DDS2_P5
```

```
                | +DDS11_2 -DDS2_P6
                | +DDS13_2 +DDS2_P7
                | +DDS15_2 +DDS2_P8
                | +DDS17_2 +DDS2_P9
DDSMyl2       4 +DDS1_2 +DDS2_P1
                | +DDS3_2 +DDS2_P2
                | +DDS7_2 +DDS2_P4
                | +DDS13_2 -DDS2_P7
                | +DDS15_2 -DDS2_P8
                | +DDS17_2 -DDS2_P9
DDSKap2       4 +DDS5_2 +DDS2_P3
                | +DDS9_2 -DDS2_P5
                | +DDS11_2 +DDS2_P6
ITS           5 +ITS  -ITS1_3  -ITS3_3  -ITS5_3
                -ITS7_3  -ITS9_3  -ITS11_3
ITSAl         4 +ITS1_3 -ITSP_1
                | +ITS3_3 -ITSP_2
                | +ITS5_3 -ITSP_3
                | +ITS7_3 +ITSP_4
                | +ITS9_3 +ITSP_5
ITSAl1        4 +ITS11_3 +ITSP_6
ITSMyl        5 +ITS1_3 +ITSP_1
                | +ITS3_3 +ITSP_2
                | +ITS7_3 -ITSP_4
                | +ITS9_3 -ITSP_5
ITSMyl1       5 +ITS11_3 -ITSP_6
ITSKap        4 +ITS5_3 +ITSP_3
VacWTi1       5 +VacW1 +VacWP1
VacWMyl1      5 +VacW1 -VacWP1 +VacWP2
VacWAl1       5 +VacW1 -VacWP2
END
GEOEND
*..+....1....+....2....+....3....+....4....+....5....+....6....+....7..
ASSIGNMA    BLCKHOLE   BLKBODY
ASSIGNMA      VACUUM      VOID
*Voxel cage
ASSIGNMA      VACUUM     VOXEL
*Voxel cage
ASSIGNMA       WATER     WATER
COMPOUND   -0.026362  HYDROGEN -0.691133    CARBON  -0.07327  NITROGENKAPTON
COMPOUND   -0.209235    OXYGEN                                    KAPTON
*Mylar, Melinex
MATERIAL                             1.4                          Mylar
```

```
COMPOUND         8.0  HYDROGEN      10.0    CARBON       4.0    OXYGENMylar
*652 Titanium oxide
MATERIAL                              4.24                                TitanOx
COMPOUND         2.0    OXYGEN       1.0  TITANIUM                      TitanOx
MATERIAL           7                0.00129                             NitroGas
COMPOUND         2.0  NITROGEN                                          NitroGas
*104 Air dry (near sea level)
MATERIAL                              0.00129                             ICRU-104
COMPOUND  -0.0001248    CARBON -0.755267  NITROGEN -0.231781    OXYGENICRU-104
COMPOUND   -0.012827     ARGON                                          ICRU-104
*C  H  O
*  5  8  2
MATERIAL                              1.193                               PMMA
COMPOUND         8.0  HYDROGEN       5.0    CARBON       2.0    OXYGENPMMA
ASSIGNMA         AIR    AirGap
ASSIGNMA      KAPTON   KapFoil
ASSIGNMA         AIR     RaShi
#if RaShi
ASSIGNMA        PMMA     RaShi
#endif
ASSIGNMA       WATER     WATER
ASSIGNMA    ALUMINUM    DDSAl1
ASSIGNMA    NITROGEN      DDS1
ASSIGNMA       Mylar   DDSMyl1
ASSIGNMA      KAPTON   DDSKap1
ASSIGNMA    NITROGEN      DDS2
ASSIGNMA    ALUMINUM    DDSAl2
ASSIGNMA       Mylar   DDSMyl2
ASSIGNMA      KAPTON   DDSKap2
ASSIGNMA    ALUMINUM     ITSAl
ASSIGNMA    ALUMINUM    ITSAl1
ASSIGNMA       Mylar    ITSMyl
ASSIGNMA       Mylar   ITSMyl1
ASSIGNMA      KAPTON    ITSKap
ASSIGNMA         AIR       ITS
ASSIGNMA         AIR   VacWAl1
ASSIGNMA         AIR  VacWMyl1
ASSIGNMA         AIR   VacWTi1
RAD-BIOL                                                                 example
ROT-DEFI
*Isocenter translation
!@dicom=rtplan
ROT-DEFI         100                  11.72682 -4.318414  22.55008RTPLAN
```

```
*HFS Voxel Rotation
!@dicom=rtplan
ROT-DEFI         100         0        90                                RTPLAN
!@dicom=RTDOSE-1
!@pos=[-25.25, -25.25, -34.85]
!@iop=[1.0, 0.0, 0.0, 0.0, 1.0, 0.0]
USRBIN          10.0   ALPHA-D     -99.0     25.35     25.35    -19.051-ALPHA-D
USRBIN        -25.25    -25.25    -34.85       506       506       158 &
*Set the random number seed
RANDOMIZ         1.0
*Set the number of primary histories to be simulated in the run
START          100000
STOP
```